A Computational Fluid Dynamics Driven Machine-Learning Framework for Observation and Quantification of Extreme Ship Responses

by

Kevin M. Silva

A dissertation submitted in partial fulfillment
of the requirements for the degree of
Doctor of Philosophy
(Naval Architecture and Marine Engineering)
in The University of Michigan
2023

Doctoral Committee:

Associate Professor Kevin J. Maki, Chair
Associate Professor Matthew D. Collette
Professor Krzysztof J. Fidkowski
Assistant Professor Yulin Pan

Kevin M. Silva

kmsilva@umich.edu

ORCID iD: 0000-0002-8100-2475

Dedicated to my family.

ACKNOWLEDGEMENTS

This dissertation has been supported by the Department of Defense (DoD) Science, Mathematics, and Research for Transformation (SMART) Scholarship, and the Naval Surface Warfare Center Carderock Division (NSWCCD) Extended Term Training (ETT) and Naval Innovative Science and Engineering (NISE) program. Additionally, I would like to thank the Office of Naval Research (ONR) for their support under program manager Dr. Woei-Min Lin.

I would like to express my deep gratitude to my supervisors at NSWCCD throughout this Ph.D., Mr. Timothy Smith and Dr. Martin Donnelly. From the beginning, they were staunch advocates of me pursuing a Ph.D. I would not have been able to complete this dissertation or any of the research within it, without their support. The backing of Tim and Martin, and the resulting funding enabled me to focus on my research and provided me opportunities to explore my intellectual curiosity that I will appreciate forever.

I am also grateful for my colleagues at NSWCCD, who opened their doors for many beneficial discussions - Mr. Andrew Silver, Mr. Bradley Campbell, Dr. Sheguang Zhang, Mr. Kenneth Weems, and Dr. Vadim Belenky. Their knowledge and passion for ship hydrodynamics has been instrumental in my professional development. My pursuit of the topics in this dissertation are a direct consequence of our relationship.

I want to extend special thanks to my advisor, Professor Kevin Maki. As a Masters student in his Intro to Numerical Hydrodynamics class, I became infatuated with numerical hydrodynamics. Kevin's infectious energy and passion for ship hydrodynamics,

has always made it enjoyable to discuss research with him. His guidance, friendship, and patience throughout this dissertation will have a long-lasting impact on my career and life.

I am also appreciative of Professor Matthew Collette, Professor Yulin Pan, and Professor Krzysztof Fidkowski for sitting on my committee and offering constructive feedback that greatly increased the quality of this dissertation.

My academic journey began in Lowell and moved to Ann Arbor. I then started my professional career in D.C., but then found myself back in Ann Arbor before returning to D.C. I am incredibly thankful for all the great friends I have made throughout this experience. This includes my hometown friends in Lowell who will not understand a word of this dissertation, but were always avid supporters nonetheless; my friends in Ann Arbor, especially those in the Computational Ship Hydrodynamics Laboratory (CSHL), who I could speak for hours with about ship hydrodynamics; and finally, my friends in D.C., some of which have followed me from both Lowell and Ann Arbor, whose friendship has been invaluable throughout this Ph.D.

I am also incredibly thankful to my family, in particular my parents Luis and Maria, and my sister Stephanie. There is an alternate universe where I would not have even attended college after High School, let alone pursue a Ph.D. I owe my family a special thanks for always pushing me to reach my full potential.

Finally, to end my long list of acknowledgments. I am truly grateful to my fiancée Tori. Few people better understand the time and effort that went into this dissertation. Whenever there was a breakthrough in research, she was the first to hear and celebrate these triumphs. During difficult times of slow progress and obstacles, she was there to provide me with the encouragement and space I needed to dive deep and overcome challenges. Without her unconditional love, support, and dependable copy-editing, I would not have been able to push my research to the extent that I have and produce this dissertation.

TABLE OF CONTENTS

LIST OF FIGURES

Figure

LIST OF TABLES

Table

LIST OF ABBREVIATIONS

1-DoF	One Degree-of-Freedom
2-D	Two-Dimensional
2-DoF	Two Degrees-of-Freedom
3-D	Three-Dimensional
3-DoF	Three Degrees-of-Freedom
6-DoF	Six Degrees-of-Freedom
ALE	Arbitrary Lagrangian-Eulerian
BEM	Boundary Element Methods
CFD	Computational Fluid Dynamics
CPU	Central Processing Unit
CSHL	Computational Ship Hydrodynamics Laboratory
CWG	Critical Wave Groups
DLG	Design Loads Generator
DoF	Degrees-of-Freedom
DTMB	David Taylor Model Basin
EPOT	Envelope Peaks Over Threshold
EVD	Extreme Value Distribution
FFT	Fast Fourier Transform
FORM	First Order Reliability Method
GPR	Gaussian Process Regression
GRU	Gated Recurrent Units
HPC	High-Performance Computing
KDE	Kernel Density Estimation
LAMP	Large Amplitude Motion Program
LSTM	Long Short-Term Memory
ODE	Ordinary Differential Equation

ONRT Office of Naval Research Tumblehome

PDF Probability Density Function

PID Proportional–Integral–Derivative

POT Peaks Over Threshold

RAO Response Amplitude Operator

RMSE Root Mean Square Error

RNN Recursive Neural Networks

ROWG Reduced Order Wave Groups

SI System Identification

URANS Unsteady Reynolds-averaged Navier-Stokes

VOF Volume-of-Fluid

WF Whicker and Fehlner

ABSTRACT

The prediction of extreme ship responses remains an important and longstanding topic in ship hydrodynamics, with continued focus on developing probabilistic methods based on simplified descriptions of the hydrodynamics that mainly produce qualitative observations. While simpler hydrodynamic formulations provide insight into extreme events, their underlying assumptions can prevent accurate quantitative representations of the mechanisms ultimately responsible for the extreme responses. With this limitation in mind, research must strive to utilize increasingly more accurate hydrodynamic formulations to provide quantitative observations and statistical characterization of extreme ship response events. Additionally, previous work in the prediction and quantification of extreme events has involved simplifications such as only considering zero speed or constant speed and heading. Consequently, resulting calculations have largely neglected free-running vessels traveling with 6 degrees-of-freedom (6-DoF), where surge, sway, and yaw motions, in conjunction with propeller and rudder forces, contribute to extreme events and failures. The following research develops the CCS extreme event probabilistic framework capable of both observing and quantifying the probability of extreme events by integrating the critical wave groups (CWG) extreme event probabilistic method, fully nonlinear Computational Fluid Dynamics (CFD) to achieve a high-fidelity representation of the hydrodynamics, and long short-term memory (LSTM) neural networks to build surrogate models of the CFD predictions to improve the overall computational efficiency. This framework intentionally accommodates free-running vessels as well as various physical dynamical mechanisms that could lead to extreme events, without the need for intrusive dynamic constraints. As

a result, this approach provides an avenue forward for high-fidelity extreme event analysis at a practical computational cost.

This dissertation demonstrates the CCS framework on case studies utilizing a two-dimensional (2-D) midship section and a three-dimensional (3-D) representation of the Office of Naval Research Tumblehome (ONRT) hull form. The CCS framework is first demonstrated with a 2-D midship section of the ONRT in Sea State 7 beam seas that is only free to heave and roll. The case study implements the CCS framework with and without the LSTM neural networks to understand both the accuracy of the framework as well as the accuracy of the surrogate modeling technique for extremes. The CCS framework is able to produce responses and probability predictions that are representative of a purely CFD-driven CCS framework with 200 high-fidelity CFD training simulations, corresponding to seven orders of magnitude of computational cost savings when compared to a Monte Carlo approach. The other case study implements the CCS framework for a free-running 3-D ONRT, traveling in stern-quartering Sea State 7 seas and free to move in all 6-DoF. The case study tests the ability of the CCS framework to handle arbitrary frames of encounter when enforcing initial conditions as well as the ability of the LSTM neural networks to represent the extreme 6-DoF vessel response. Similarly to the 2-D case study, the probability of exceedance calculations from the surrogate models converge at around 200 training runs and produce LSTM predictions that are representative of the CFD validation simulations. The 3-D case study provides a total of three orders of magnitude in computational cost savings compared to Monte Carlo.

This dissertation develops the CCS framework and an LSTM neural network surrogate modeling methodology, as well as showcases significant advancement in the observation and probabilistic quantification of extreme ship response events with significant reductions in computational cost.

CHAPTER I

Introduction

Vessels experience a wide range of wave groups throughout their lifetime, some of which may lead to extreme events such as capsizing, broaching, large loads, etc., that can cause catastrophic failures and result in the casualty of vessels, equipment and personnel. Designers typically optimize performance for normal operating conditions, while at the same time ensuring survival in the most extreme conditions through either model testing or numerical hydrodynamic simulations to measure quantities such as the mean or standard deviation of a particular response. However, it is likely that assessments in random waves will lack the ability to capture the extremes for events like those in Figure 1.1, and will not deepen the understanding of the mechanisms and environmental characteristics that trigger extreme responses. Not only is it important to understand the dynamical behavior of ships due to a discrete wave environment that induces an extreme event, but it is also important to understand the probability of the event and others like it that also lead to extremes. Proper understanding and categorizing of the possible dynamical responses and the corresponding wave sequences during extreme events is crucial and constitutes one of the most difficult topics in ship hydrodynamics.

Figure 1.1: Depiction of significant extreme ship response events.

The observation and probabilistic quantification of extreme ship responses is challenging due to three main reasons:

1. Stochasticity of the ocean environment and rareness of extreme events
2. Complex nonlinear hydrodynamic behavior of a vessel in large amplitude waves
3. Evaluation costs associated with nonlinear hydrodynamic behavior

The stochastic nature of the ocean environment signifies that a large variety of wave sequences are possible and the time between extreme events is long. Monte Carlo-type direct assessments require many realizations of random wave fields to identify extreme events, and become impractical as the rarity of an event increases. The exposure time required to observe an extreme event increases exponentially with respect to the rarity of the response (*Ochi*, 1998). Figure 1.2 demonstrates a Probability Density Function (PDF) for a given response ϕ. The tail region of the PDF is highlighted in red and is the region of interest for extreme events that is computationally expensive to quantify through random observations. Probabilistic methods have been developed to help address this issue by directly targeting and resolving the tail region of the PDF and are summarized in Section 1.1 in relation to marine dynamics problems.

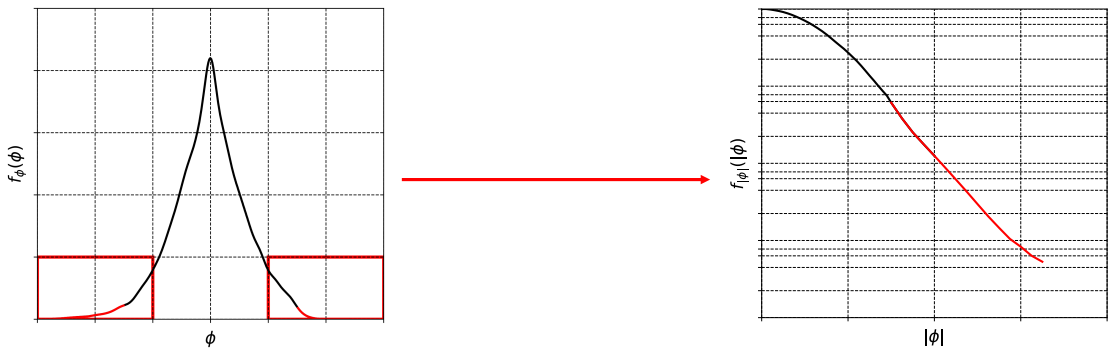

Figure 1.2: Tail region of the PDF.

Extreme event evaluations also require a characterization of the dynamical relationship between the environment and the resulting ship responses. The largest waves in the environment may not lead to the largest responses. Frequently, a series of successive waves may produce a more severe response than a single wave. Additionally, ship responses are highly nonlinear during extreme events for both the ship dynamics and hydrodynamics, and require advanced numerical hydrodynamic methods to resolve this phenomena which increases the computational cost of any extreme event evaluation. Different numerical hydrodynamic methods are reviewed in Section 1.2.

Due to the nonlinearity of extreme events, they are also influenced by initial conditions. Figure 1.3 shows an example case study from *Lee et al.* (2006), where the response of a floating box barge due to same wave excitation but different initial roll and roll velocity is investigated with both numerical simulations and experiments. Each marker in Figure 1.3 corresponds to whether a numerical simulation or experiment resulted in a capsize or not as a consequence of the initial condition. Figure 1.3 showcases not only that different initial conditions can lead to different responses, but it could also be the difference between safe operations or a failure event like a capsize. For extreme event evaluations, both the probabilistic and numerical hydrodynamic methods must be able to consider the influence of initial conditions. Figure 1.3 also shows results from experiments that denote capsize and no capsize for virtually the

same initial conditions, which demonstrates the high level of difficulty in precisely enforcing initial conditions of interest consistently and repeatedly in an experimental setting.

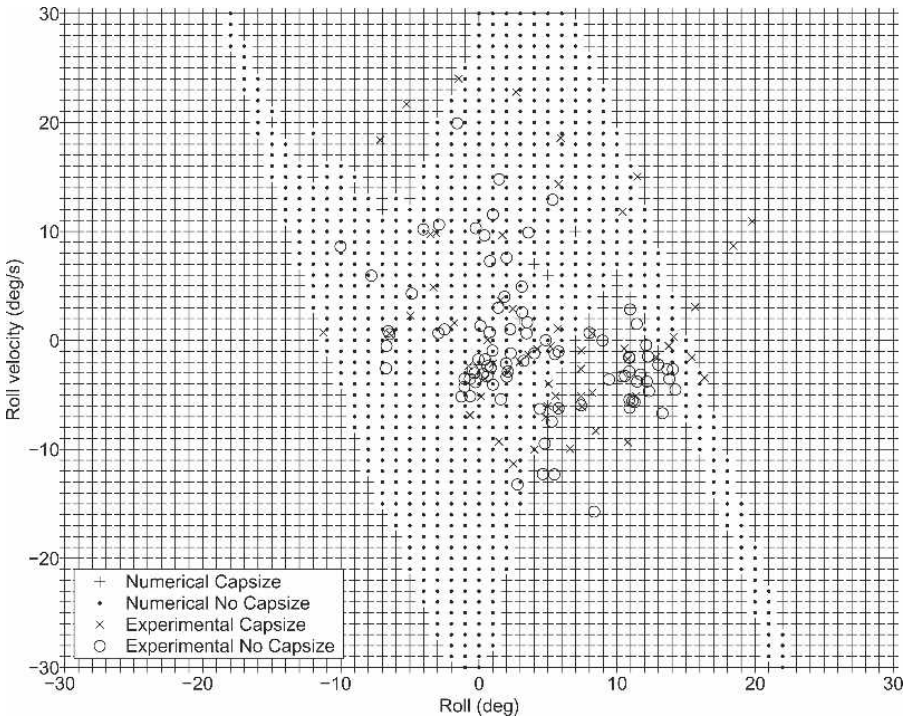

Figure 1.3: Comparison of capsize basin boundaries for same regular wave at different initial conditions from *Lee et al.* (2006).

Probabilistic methods aim to reduce the computational cost associated with the stochastic ocean environment, while numerical hydrodynamic methods provide observations of the ship response . However, many evaluations with a higher-fidelity numerical hydrodynamic method can be computationally expensive and render a complete characterization of extreme responses impractical. Surrogate modeling techniques can be leveraged to create representative models of the ship's response to reduce the overall computational cost. A review of surrogate modeling techniques for marine dynamics is summarized in Section 1.3.

The objective of this dissertation is to develop a framework capable of both observing realizations of extreme events and quantifying the probability of their

occurrence. The framework should consist of a probabilistic method to reduce the cost of evaluating the environment and quantify the probability of extremes, a numerical hydrodynamic method for producing observations of the extreme events to not only understand mechanisms that cause them, but that provides quantitative information of the extreme responses to the probabilistic calculation, and surrogate modeling techniques that reduces the computational cost of the entire framework. Additionally, the framework should be able to handle arbitrary ship responses, be applicable to free-running vessels, and quantitatively evaluate the extreme response.

1.1 Literature Review: Probabilistic Methods

Probabilistic methods are employed to address the computational cost of Monte Carlo-type assessments of extreme events. A large body of research has focused on the probabilistic description of extreme events as a consequence of the random nature of the ocean environment. Due to their rarity, a Monte Carlo-type direct assessment to identify extremes is impractical. The time between events is long, and a vast amount of data is needed to make meaningful assessments. Additionally, the largest waves do not necessarily equate to the largest responses, therefore, the selected probabilistic method must be flexible enough to incorporate this phenomena. There are several types of extreme event probabilistic methods, each with their own limitations. The objective of this dissertation is to develop a framework that can both observe realizations of extreme events and quantify the probability of their occurrence. Therefore, a probabilistic method chosen within this framework must allow for both. In the context of the framework developed in this dissertation, the invoked probabilistic method must also consider initial conditions, account for nonlinearity, allow for analysis of arbitrary responses of free-running vessels and not assume the response fits into any distribution. Together, these criteria ensure that extreme event evaluations are quantitative and completed comprehensively, without limiting assumptions. The following sections in

this chapter provide a brief overview of several popular methodologies and their ability to accomplish the overarching objectives of this dissertation.

1.1.1 Extrapolation Methods

Historically, the most common approaches for characterizing ship responses have been extrapolation-type methods, where limited observations of a dynamical response are extrapolated to regimes beyond the available dataset. An advantage of these methods is that they can leverage available datasets and are flexible enough to handle both simulation, experimental, and full-scale datasets (*Gaidai et al.*, 2016). Additionally, extrapolation methodologies can be applied to arbitrary responses, free-running vessels and initial conditions are inherently included if sufficiently long time windows are observed.

A popular concept in the probabilistic characterization of extreme ship response events is to employ the principle of separation (*Belenky et al.*, 2012). The principle of separation divides the ship response problem into two sub-problems, a rare and non-rare sub-problem. The *non-rare* sub-problem focuses on determining the probabilities of environmental conditions that precipitate extreme responses and the distribution of initial conditions. The *rare* sub-problem assesses whether an extreme response will occur, given the environmental and initial conditions, as well as the corresponding probability. The principle of separation is employed in the Peaks Over Threshold (POT) (*Campbell and Belenky*, 2010a), which identifies upcrossings of a moderate threshold for a given response to characterize the non-rare sub-problem and then extrapolates all the peaks above the prescribed threshold to solve the rare sub-problem. An alternative to the POT method is the Envelope Peaks Over Threshold (EPOT) method (*Campbell and Belenky*, 2010b; *Belenky and Campbell*, 2011), where the identification of upcrossings and the fitting of the peaks is performed on a characteristic envelope of the peaks, rather than the peaks themselves.

One of the largest disadvantages of extrapolation methods is that the they do not contain an explicit model of extreme nonlinear motions, thus analysis performed by these extrapolation methods is limited by the available data. Therefore, any nonlinear phenomena present outside of the available data is unknown and not incorporated into the extrapolation explicitly. Another disadvantage of extrapolation methods is that they are performed *a posteriori* and do not actually produce observations, but rather they conduct analysis with existing data. An additional limitation of extrapolation methods is that they require an assumption of the underlying distribution. Therefore, different vessels or responses may require different fitting techniques and may not provide generalized models.

1.1.2 Split-Time Method

The split-time method is a perturbation method first developed in *Belenky* (1993) that also employs the principle of separation and divides the extreme ship response problem into rare and non-rare sub-problems with a threshold. The non-rare sub-problem for the split-time method is reliant on identifying up-crossings of a moderate threshold for a response of interest. The rare sub-problem involves the determination of a perturbation that leads to a failure, thus calculating a *distance to danger*. Figure 1.4 shows an application of the split-time method for pure loss of stability from *Belenky et al.* (2012). In the case of pure loss of stability, the threshold for the non-rare problem is θ_m, the time-dependent instantaneous angle of the righting arm (GZ) maximum (*Belenky et al.*, 2010). Up-crossings of the time-dependent threshold θ_m are observed for roll θ, and the perturbation $\dot{\theta}_{cr}$, is the roll velocity $\dot{\theta}$ required to trigger a capsize.

The split-time method contains an explicit model of nonlinearity and can be generalized for both pure loss of stability (*Belenky et al.*, 2010, 2011), and capsizing caused by broaching-to (*Weems et al.*, 2020). Additionally, the split-time method is suitable for free-running vessels because the vessel location in space and time is known

at the moment a moderate upcrossing occurs, and perturbations can be performed at that exact location (*Weems et al.*, 2020). The split-time method could, in principle, be applied to arbitrary response quantities, but would require research into what the appropriate upcrossing and perturbation quantities are for each new problem. Additionally, initial conditions are included through the identification of upcrossings, and the split-time method does not assume the distribution of the responses.

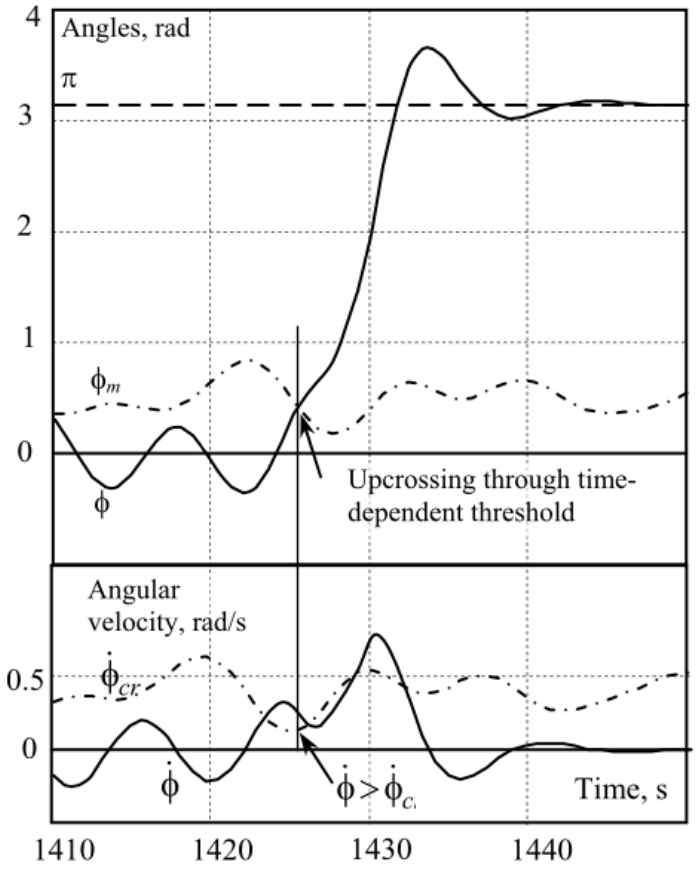

Figure 1.4: Split-Time method for pure loss of stability (*Belenky et al.*, 2012).

The split-time method provides observations of extreme events through the perturbations. However, for the case of pure-loss of stability, the threshold up-crossings are for roll and the perturbation is applied to the roll velocity. This intrusive perturbation requires an instantaneous acceleration of the Degrees-of-Freedom (DoF) of interest, and could lead to an unnatural event that would be challenging to validate

experimentally. In higher fidelity numerical hydrodynamic simulation tools, it would be difficult to differentiate whether the perturbation leading to an extreme event is physical, or purely a numerical instability.

1.1.3 First Order Reliability Method (FORM)

The First Order Reliability Method (FORM) is another probabilistic method that was popularized for extreme marine dynamics by *Jensen* (2007) and other subsequent research. The wave field is considered to be a Gaussian process and can be represented as:

$$\eta\left(x,t\right)\sum_{j}^{J}=a_j\sigma_j cos(\omega_j t-k_j x)+b_j\sigma_j sin(\omega_j t-k_j x) \tag{1.1}$$

where J is the number of components, a_j and b_j are uncorrelated standard normal random variables, ω_j is the wave frequency, k_j is the wave number, $\sigma_j=\sqrt{S(\omega_j)\Delta\omega_j}$, and $S(\omega)$ is the wave spectrum. For a given wave spectrum, the response ϕ of a dynamical system at time t excited by Equation 1.1, is dependent on the variables a_j and b_j. As illustrated in Figure 1.5, an limit state surface can be defined for a pre-determined extreme response ϕ_0 as:

$$G=\phi\left(t|a_1,b_1,a_2,b_2,\ldots,a_J,b_J\right)-\phi_0=0 \tag{1.2}$$

where the goal of FORM is to identify, through iteration, the most probable a^* and b^* that leads to the pre-determined extreme response at $G=0$, with the limit state surface linearized at the most probable point. The exceedance region, $G>0$, corresponds to observations that exceed the desired response, the non-exceedance region, $G<0$, denotes observations that are smaller than the desired response the the exceedance surface, $G=0$.

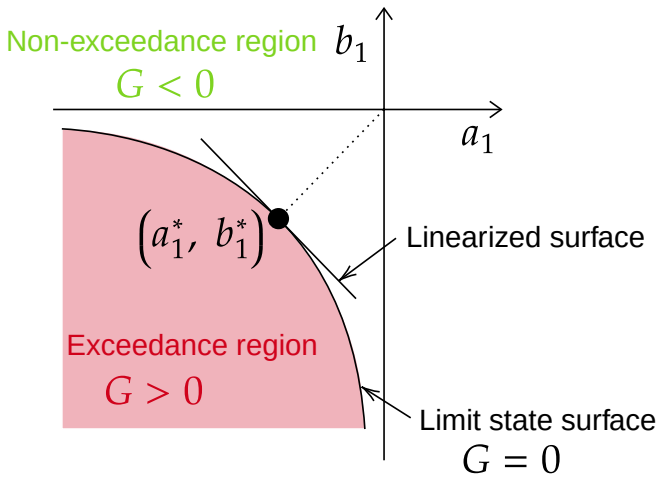

Figure 1.5: Illustration of FORM exceedance surface (*Xu*, 2020).

FORM allows for observation of extreme events through iterative search, where initial conditions are implicitly included in the random wave field description, and the response of the vessel is allowed to be nonlinear and is not required to fit any prescribed distribution. However, the objective of FORM is to identify the most probable wave sequence that will lead to a pre-determined response. Therefore, it does not attempt to understand the probabilistic space of all wave sequences that will lead to the pre-determined response, and is not a comprehensive probabilistic quantification of the extremes. An ensemble of observations is required to understand the mechanism behind the extremes.

Additionally, the iterative nature of FORM has the potential of being cost prohibitive. If many iterations are required, the cost would scale linearly. Additionally, the computational cost of a simulation is not only defined by the total Central Processing Unit (CPU) time, but also the the time-to-solution. For example, launching ten simulations in parallel simultaneously would provide a faster time-to-solution than launching one simulation sequentially for ten iterations. Therefore, a methodology that does not require iteration would be preferable.

1.1.4 Design Loads Generator (DLG)

The Design Loads Generator (DLG) developed in *Alford* (2008); *Alford et al.* (2011); *Kim* (2012) uses a calculated response spectrum to predict the Extreme Value Distribution (EVD), then generates random non-uniform phases that match the distribution, and finally maps the phases to a wavemaker that generates the waves that lead to the response. An advantage of this method is that an infinite number of events can be generated, which gives an opportunity to realize multiple extreme events for an arbitrary response. This capability allows engineers to generate short-time window events that can be realized with experiments or high-fidelity simulations to observe the physics and mechanisms at play during extreme events.

However, a disadvantage of DLG is that the EVD is built with a response spectrum based on a Response Amplitude Operator (RAO), which is inherently a linear prediction that differs from the nonlinear state involved during an extreme event. All of the observations in the DLG method are utilized with information from the RAO. Therefore, the new information from the generated events does not feed back into the EVD prediction, and all of the probabilistic calculations are completed *a priori*. Additionally, the overarching DLG method is based on linear methods, thus inheriting the Gaussian assumption of the ship's response.

The DLG is only focused on generating wave sequences that are derived from EVD and does not explicitly include initial conditions. During an observation, the initial conditions of the vessel state could be varied prior to encountering the wave sequences generated by the DLG. However, there is not a mechanism for relating the resulting observations to relevant statistics. Therefore, the observations do not provide any quantitative probabilistic information.

1.1.5 Reduced Order Wave Groups

A general category of probabilistic methods that allow both the observation and probabilistic quantification of extremes are Reduced Order Wave Groups (ROWG) methods. There are different ways to parameterize wave groups from existing observations, but some of the most popular are envelope type-approaches performed in *Cousins and Sapsis* (2016); *Gong et al.* (2020) and shown in Figure 1.6. The envelope $\rho(m)$ in Figure 1.6 is applied to the wave elevation and allows for a simple parameterization based on group amplitude A and the group length L.

The objective of any wave parameterization is to reduce the stochastic wave field down to an exhaustive collection of groups with a corresponding probabilistic map like that shown in Figure 1.7. Then, the wave groups can be discretized and observations of the ship response due to a given wave group can be made with experiments or simulations. The maximum response due to each of these wave groups can then be related to the probability of each group. With enough observations to cover the entire probability space, the probability of extremes can be determined.

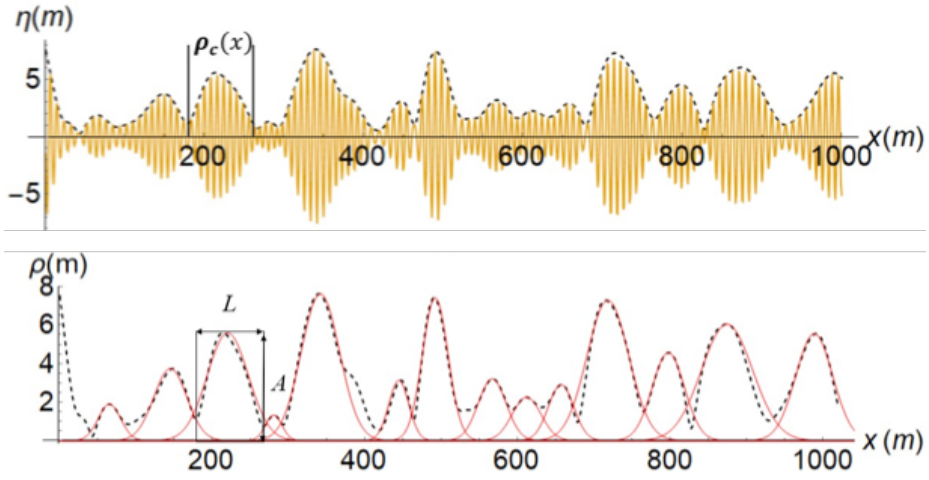

Figure 1.6: Envelope approach for identifying wave groups (*Gong et al.*, 2020).

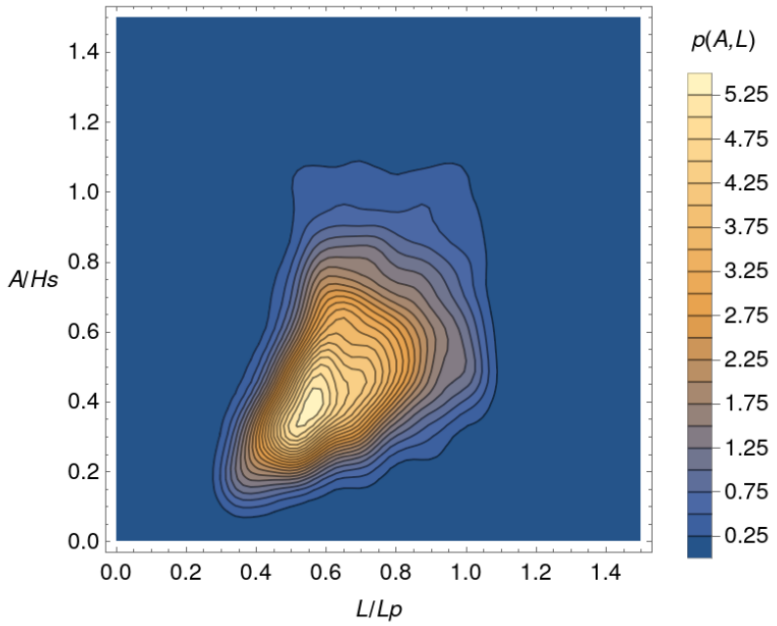

Figure 1.7: PDF for reduced order wave groups from (*Gong et al.*, 2020).

ROWG methods are similar to the DLG method in that they allow for the short time-window observations of extreme events that are suitable for either experiments or high-fidelity simulations. However, the ROWG methods do not make any assumption about the ship's response, and while it could handle arbitrary responses and nonlinearity, all of the assumptions and simplifications of this method are in the wave parameterization and its respective probabilities. Additionally, since the probabilities are calculated directly through observations, initial conditions can be included in the observations as well (*Gong and Pan*, 2022a,b). ROWG methods could also be applied to free-running vessels, but would require care to ensure the wave group is encountered correctly. The main issue with ROWG methods is that it is difficult to parameterize wave groups down to an exhaustive set without significant variability within each group description. The popular parameterization methods like envelope approaches tend to perform better for narrow-banded spectra (*Cousins and Sapsis*, 2016), where the group shape is more distinct but are difficult to implement in a generalized manner for arbitrary seaways.

1.1.6 Critical Wave Group (CWG) Method

The Critical Wave Groups (CWG) method was first developed in *Themelis and Spyrou* (2007) for regular waves and then further extended to irregular waves and explored in *Anastopoulos et al.* (2016); *Anastopoulos and Spyrou* (2016, 2017, 2019). The main idea of the CWG method is that the probability of a response exceeding a specified threshold is equal to all the wave groups and ship states at the moment of encountering the wave group that lead to an exceedance.

CWG also utilizes the principle of separation, where the non-rare sub-problem consists of the probability of the different ship states at the moment of encounter, and the rare sub-problem determines which wave group leads to the threshold exceedence. Separating the problem in this manner allows for the randomness and probabilities to be captured in the non-rare sub-problem, and the rare sub-problem is deterministic. The main advantage of the CWG method is that extreme events are observed as in the DLG method, but the results contribute to the formation of the extreme response distribution like a ROWG method. The CWG method is a type of ROWG method aside from the fact that the objective of the CWG is not to develop a mapping of all wave groups to a corresponding maximum response. Instead, the CWG method attempts to identify wave groups that lead to a near-exceedance of a specified threshold for specified ship states at the moment of encountering the group. These wave groups that lead to a near exceedance are referred to as a *critical* group and the CWG makes an assumption that any group of similar shape with larger wave heights should also lead to an exceedance. Therefore, for an exhaustive set of wave group shapes, only observations of the critical wave groups are needed and the probability of all wave groups larger than the critical group can be combined to calculate probability of exceedance at a particular threshold.

The CWG method does not make any assumption about ship response distribution, allows for nonlinearity in the ship response, and can be applied to arbitrary responses

as well as free-running vessels, although careful consideration of the different encounter frames must be taken. The method also includes initial conditions explicitly through the consideration of the ship state at the moment of encountering the wave group. Out of all the probabilistic methods reviewed, the CWG method has the greatest potential of accomplishing the overarching objectives of the desired framework from the probabilistic perspective. A complete description of the CWG method is described in detail in Chapter II.

The main drawback of the CWG method is that all of the previous research consists of case studies with One Degree-of-Freedom (1-DoF) Ordinary Differential Equation (ODE) models for roll. Only the response due to the wave group is simulated with the ODE and the ship state at the moment of encountering the wave group can be varied and prescribed as the initial condition for the ODE. However, impulsively starting a wave group from rest and prescribing a complete description of the body and fluid state at the moment of encounter is not physically possible. These issues must be addressed if the CWG method were to be implemented with higher-fidelity numerical hydrodynamic methods or experiments. Further discussion on proposed remedies for this limitation and information on physically realizable initial conditions can be found in Chapter IV.

1.2 Literature Review: Numerical Hydrodynamics

The hydrodynamics during extreme events are significantly nonlinear and complex, and require resolution of the different physical phenomena involved. Experiments provide an avenue to reproduce quantitative evaluations of the ship response. However, the cost of constructing a physical model and operating a facility to perform the testing can be prohibitive, especially if a large volume of observations or hull form geometry variants are desired. Therefore, within a framework for observing and quantifying the probability of extreme events, numerical hydrodynamic methods provide an avenue for

producing observations of a given ship's response during extremes virtually through simulation.

Numerical hydrodynamic methods have been developed with different levels of fidelity and computational cost. For inclusion within the framework desired in this dissertation, a numerical hydrodynamic method is required to resolve the the different phenomena in Figure 1.8 for a free-running vessel. The forces acting on the hull include the hydrodynamic radiation and diffraction, the hydrostatic restoring, the wave excitation, circulatory lift and cross-flow drag, the wind, and the contributions from the various appendages. To achieve quantitative evaluations of extreme events, the outlined forces illustrated in Figure 1.8 must be considered with as little empirical modeling as possible, but at a reasonable computational cost.

The following sections in this chapter provide a brief overview of several numerical hydrodynamic methodologies and their ability to accomplish the overarching objectives of this dissertation. These methods range from low-fidelity (computationally fast and less accurate) to high-fidelity (computationally slow, but more accurate), as well as medium-fidelity methods that provide a balance between computational cost and accuracy.

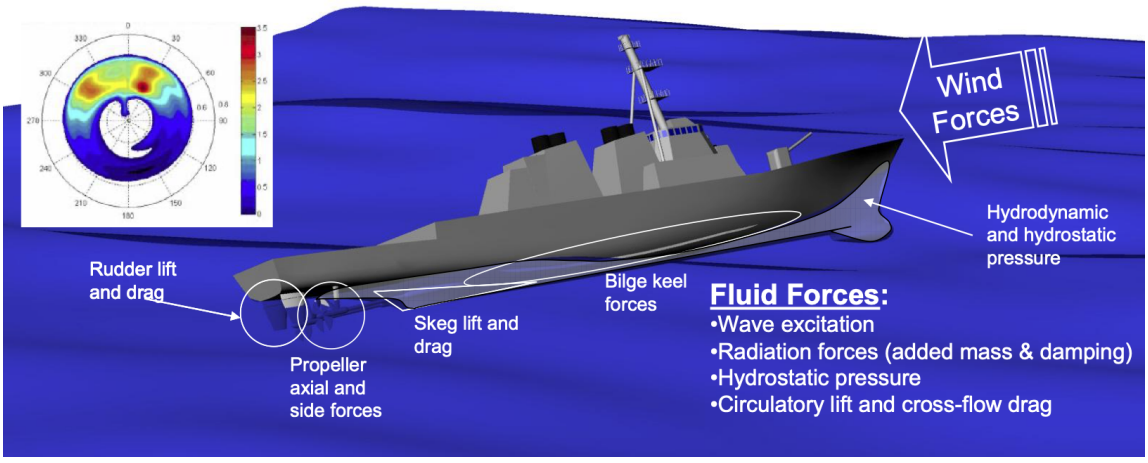

Figure 1.8: Illustration of the ship maneuvering in waves from *Belknap and Reed* (2019).

1.2.1 Low-Fidelity

Low-fidelity numerical hydrodynamic tools have the advantage of being computationally inexpensive, allowing for faster evaluations, which enables longer exposure observations of the dynamical response of a vessel. Historically, the probabilistic methods outlined in Section 1.1 are implemented with low-fidelity numerical hydrodynamic simulation tools due to their computational efficiency. Popular low-fidelity methods in the field of extreme ship response probabilistic methods are typically ODE type models. An example of a prototypical ODE model for roll from *Kogiso and Murotsu* (2018); *Paroka and Umeda* (2006) is:

$$(I_{xx} + A_{xx})\ddot{\theta} + D(\dot{\theta}) + \Delta GZ(\theta) = M_{\text{wind}}(t) + M_{\text{wave}}(t) \tag{1.3}$$

where $\theta(t)$ is the roll angle of the ship, I_{xx} is mass moment of inertia of the ship, A_{xx} is added mass, $D(\dot{\theta})$ is the roll damping moment, Δ is the displacement, $GZ(\dot{\theta})$ is the righting arm, $M_{\text{wind}}(t)$ is the wind-induced moment, and $M_{\text{wave}}(t)$ is the wave-induced moment. Equation 1.3 and others like it only consider roll and each of the individual terms require modeling. Nonlinearity and complicated relationships can be included in an ODE model like Equation 1.3. However, the resulting formulation will never be able to represent the complex phenomena of a ship traveling through large-amplitude waves and the forces illustrated in Figure 1.8 quantitatively and with high-accuracy.

Another popular low-fidelity numerical hydrodynamic method is the volume-based approach from *Weems and Wundrow* (2013) that developed the simulation tool called SimpleCode. The dominant forces present when a ship is traveling through large amplitude waves are the nonlinear hydrostatic restoring and Froude-Krylov (forcing due to the undisturbed wave impact) forces, which are typically solved through a pressure integration over the instantaneous wetted surface, and can be computationally intensive. The volume-based approach uses Gauss's theorem to relate the pressure

integration over the wetted surface to the instantaneously submerged volume. The volume and volume moments are interpolated from pre-computed Bonjean curves and corrected for roll and wave slope as demonstrated in Figure 1.9 from *Weems and Wundrow* (2013). The conversion to this volume-based methodology allows for a 2,000 to 5,000 times increase in speed, and is able to maintain an accurate representation of one of the dominant excitation forces for extremes. The main hurdle with the volume-based methodology is that the other forces in Figure 1.8 all still require empirical models, and more advanced empirical models may interfere with the computational efficiency that makes the method favorable. Volume-based approaches are an upgrade from traditional ODE models, but are still lack accuracy for quantitative observations of extreme events.

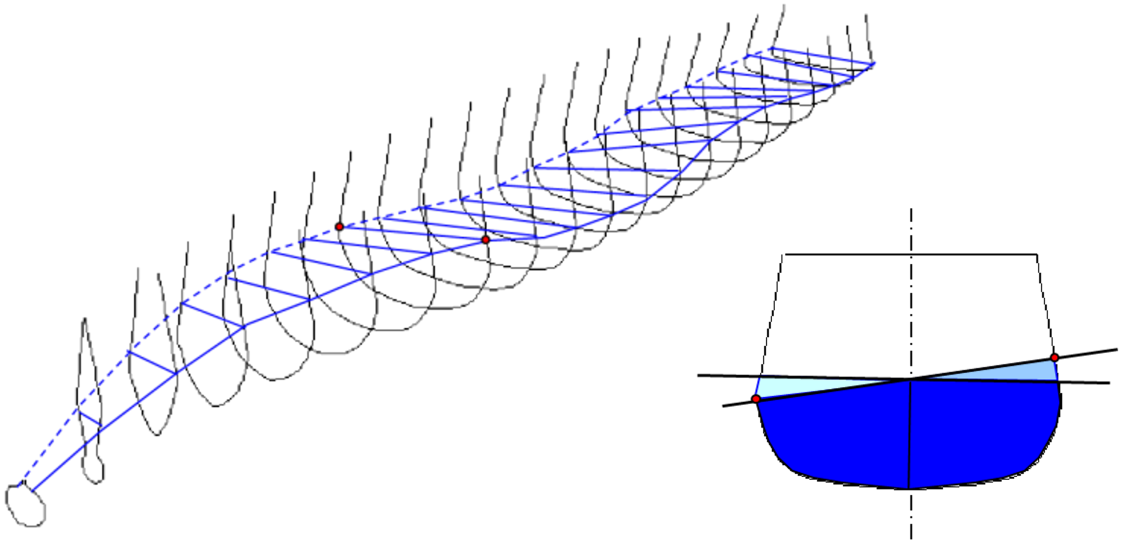

Figure 1.9: Station offsets and incident wave intersection points (*Weems and Wundrow*, 2013).

All of the low-fidelity methodologies provide a critical role in the development and testing of probabilistic methods. However, their formulation renders them qualitative and they are inadequate for developing realistic observations of extreme events or calculating the probability of their occurrence.

1.2.2 Medium-Fidelity

Medium-fidelity numerical hydrodynamic methods in this dissertation refer to potential flow methods that are typically the most popular approaches for general seakeeping evaluations. *Reed and Beck* (2016) provides a comprehensive overview of potential flow approaches, as well as previous and present developments. The approaches solve the wave-body interaction problem and are able to calculate the hydrodynamic perturbation, hydrostatic restoring and Froude-Krylov forces, either over the mean wetted surface (body-linear), or over the instantaneous wetted surface (body-nonlinear). Potential flow methods are inviscid and require empirical models to account for any viscosity-related forces. There are several approaches that fall within the category of potential flow methods for large amplitude ship motion. One such approach is the Three-Dimensional (3-D) Boundary Element Methods (BEM) (*Lin and Yue*, 1990, 1993; *Shin et al.*, 2003), where a 3-D perturbation velocity potential is computed by solving an initial boundary value problem with a potential flow BEM, and then Bernoulli's equation to compute the hull pressure distribution including the second-order terms. The Large Amplitude Motion Program (LAMP) (*Shin et al.*, 2003) is one example of a simulation tool that applies BEM on the mean wetted surface and hydrostatic restoring and Froude-Krylov forces on the instantaneous wetted surface to achieve a *blended* calculation. An alternative to the 3-D BEM is a body-exact strip-theory approach (*Bandyk*, 2009; *Belknap and Reed*, 2019), where impulsive and wave-memory problems are solved on individual Two-Dimensional (2-D) strips at every time step. Performing the evaluations at each 2-D strip allows for reduction in computational cost.

Medium-fidelity potential flow methods provide a more accurate alternative to the low-fidelity methods, but at an increased computational cost corresponding to real-time computations (*Belknap and Reed*, 2019). However, the medium-fidelity methods still require empirical models to solve the other forces outlined in Figure 1.8.

In particular, green water is not captured by the potential flow methods and requires supplemental modeling, but can play a large role in the overall response of the ship during extremes. Even with empirical modeling that accounts for water accumulating on the deck, cases with significant green water like those in Figure 1.1 will never be fully captured quantitatively when employing typical medium-fidelity potential flow methods that are considered in seakeeping evaluations. The phenomena experienced during various extreme events can be strongly nonlinear, complex, and violent, and the hydrodynamic tools may not provide quantitative representations of these physics during extremes, especially for a free-running vessel where the propeller and rudder forces must also be considered.

1.2.3 High-Fidelity

In the context of this dissertation, higher-fidelity numerical hydrodynamic methods correspond to Computational Fluid Dynamics (CFD) approaches such as Unsteady Reynolds-averaged Navier-Stokes (URANS). URANS can provide a more complete analysis than the low and medium-fidelity methods for extreme events and the various forces that dominate the response of the vessel. Unlike the medium-fidelity potential flow methods, URANS methods are not inviscid and provide an avenue forward for a full flow-field description of extreme events that allows for the characterization of all the necessary forces outlined in Figure 1.8. URANS has been increasingly applied to ship hydrodynamics problems in recent years, including simulations of extreme ship responses. The research of *Hosseini* (2009) and *Mousaviraad* (2010) demonstrated the ways in which CFD tools can be implemented to model extreme behaviors such as capsize and broaching of free-running vessels qualitatively. Other research has explored the use of CFD in probabilistic methods for extremes. *Filip et al.* (2020) and *Xu et al.* (2020) utilized CFD to simulate extreme events produced by the DLG for a fixed platform and an Office of Naval Research Tumblehome (ONRT)

hull traveling at constant speed in stern-quartering seas, while *Knight et al.* (2020) employed CFD with DLG to predict the extremes of a self-propelled ONRT hull in head seas. However, these methods only produced observations of the extremes and did not focus on quantifying them statistically due to the limitations of DLG. Of the reviewed numerical hydrodynamic methods, URANS provides the most potential of accomplishing the overarching objectives of the current research from the perspective of actually observing the extreme events with little empiricism. The main drawback of URANS is the computational cost of the methodology, which requires targeted short time-window realizations to be practical. For one hour of of full-scale simulated time, the estimated required computational cost in CPU hours is around one second for low-fidelity methods, one hour for medium-fidelity, and one million for high-fidelity (*Serani et al.*, 2021). Additionally, the computational cost of a URANS simulation is dependent on the High-Performance Computing (HPC) system, the specific software, and computational schemes, as well number of cells in the considered computational mesh which dictates the breadth of calculations required at each time-step. Therefore, simulation of extremes with URANS should only consider short time window events like the 45 deg roll event depicted in Figure 1.10, where each simulation directly impacts the probability calculation.

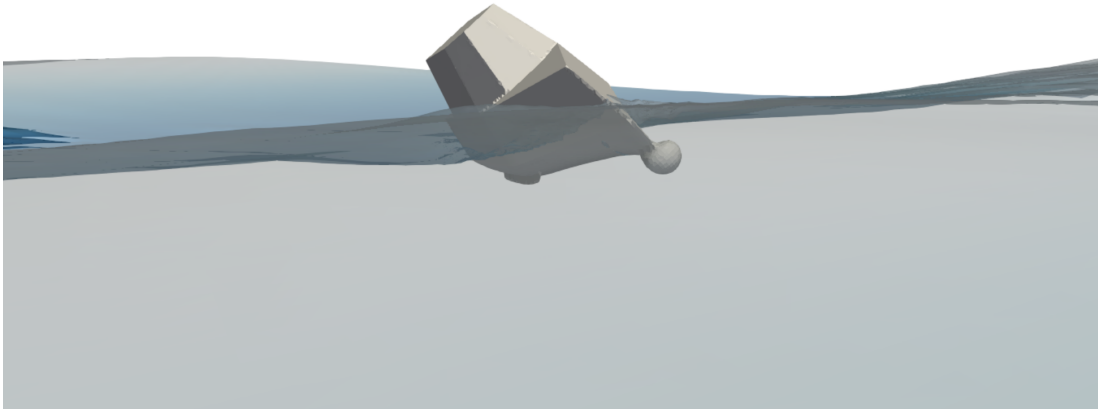

Figure 1.10: URANS observation of a 45 deg roll event.

1.3 Literature Review: Surrogate Modeling

As with many complex phenomena, accurate and quantitative predictions of ship responses in large waves are computationally expensive with advanced numerical hydrodynamic methods. Surrogate modeling techniques attempt to create models based off a limited set of data that can then be used to provide a wider range of predictions at a fraction of the computational cost of the numerical hydrodynamic tools. The need for surrogate models becomes especially important when predictions are being made with higher fidelity URANS methods discussed in Section 1.2.

The computational expense of evaluating extreme events can be broken into an observation cost and a quantification cost. The observation cost is that of a single observation and the quantification cost is the number of events required to calculate the relevant statistics. A quantification-cost driven framework requires a statistics-focused surrogate modeling technique, while an observation-focused cost-driven framework requires a prediction-focused methodology. The following sections in this chapter provide a brief overview of the various relevant surrogate modeling techniques for ship dynamics and their ability to meet the overarching objectives of this dissertation.

1.3.1 Statistics-Focused Surrogates

A statistics-focused surrogate methodology addresses the quantification cost by calculating the overall statistics of interest for a particular dynamical system. One example of a statistics-focused surrogate methodology is the research of *Schirmann et al.* (2020), where predictions of the heave, pitch, and roll standard deviation from a low-fidelity numerical hydrodynamic tool are corrected with full-scale data. A popular statistics-focused surrogate technique that has been implemented for extreme marine dynamics is the concept of sequential sampling with an ROWG method. A ROWG probabilistic method requires a map of the maximum response of a vessel with respect to a specific parameterized wave group. The evaluation of this mapping with sufficient

resolution can be computationally expensive, thus a sequential sampling methodology attempts to develop a surrogate model of this mapping, typically through Gaussian Process Regression (GPR) (*Gong et al.*, 2020; *Mohamad and Sapsis*, 2018; *Sapsis*, 2021).

Figure 1.11 from *Gong et al.* (2020) shows an example of sequential sampling in practice with an ROWG method. Figure 1.11a demonstrates a probability distribution with respect to the non-dimensional wave group amplitude A/H_s and the non-dimensional wave group length L/L_p, where the different sample points are shown throughout the space.

In *Gong et al.* (2020), six initial random sample points are selected, observations of the wave groups that correspond to those points are made, and a GPR model is constructed. GPR models naturally produce an estimate of the uncertainty. Therefore, the predictions and uncertainty in the model can be considered to select sample points for the next sequence in areas where the model has the largest uncertainty and an extreme event is likely. The objective function considered in *Gong et al.* (2020) is described by:

$$Q(\boldsymbol{\theta}^*) = \int_0^\infty \mid \hat{p}^+_{n+1}(r;\boldsymbol{\theta}^*) - \hat{p}^-_{n+1}(r;\boldsymbol{\theta}^*) \mid r^s dr \tag{1.4}$$

where r is the roll angle, $\boldsymbol{\theta}^*$, is the wave group parameter (A, L), s is a tunable parameter that targets different portions of the PDF tail, $\hat{p}^+_{n+1}(r;\boldsymbol{\theta}^*)$ and $\hat{p}^-_{n+1}(r;\boldsymbol{\theta}^*)$ are uncertainty bands (one standard deviation) on the probability distribution $\hat{p}_{n+1}(r;\boldsymbol{\theta}^*)$ that is calculated from the group-maximum to group property mapping developed from the GPR model. Optimizing Equation 1.4 provides an estimate of the next best sample to produce an observation and update the GPR model. This procedure of predicting the next best sample to produce an observation for and updating the GPR is completed sequentially until the probability distribution $\hat{p}_{n+1}(r)$ converges as shown in Figure 1.11b, where 18 sequential samples $p^{seq}_{18}(r)$ is compared to the actual

distribution $p^e(r)$ and 126 random samples p^{ran}_{126}.

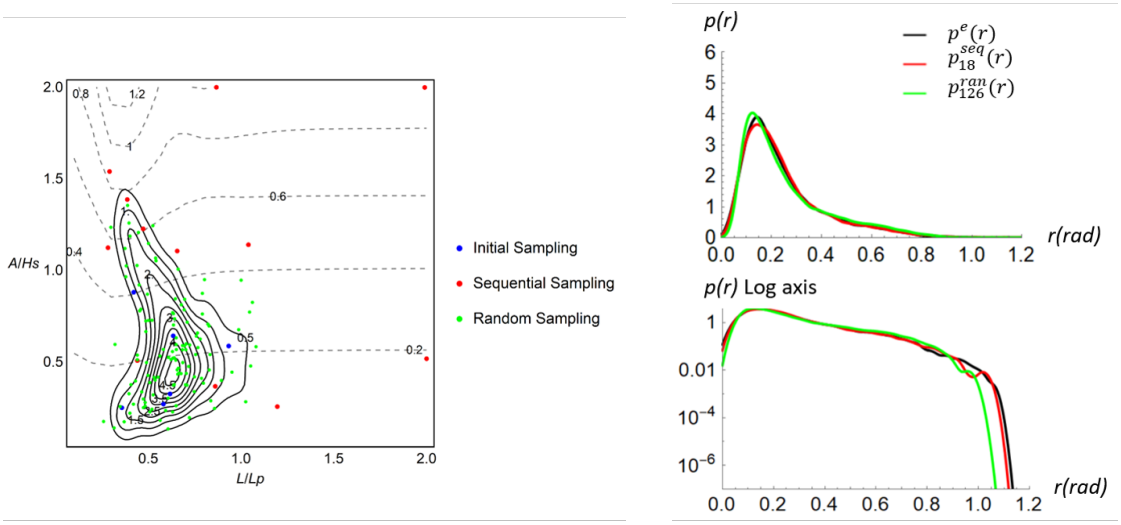

(a) Sampling (b) PDF

Figure 1.11: Construction of PDF through sequential and random sampling from *Gong et al.* (2020).

A methodology like sequential sampling is efficient and is capable of producing the underlying distribution of interest with few observations. The GPR and utilizing uncertainty-based sampling is a key aspect of the methodology and greatly accelerates the convergence of the surrogate model with limited computational cost. However, sequentially sampling has drawbacks that are similar to the probabilistic methodology FORM. Producing observations sequentially introduces an increase in your time-to-solution (*Filip et al.*, 2014) because all of the simulations must be performed serially, and they cannot be launched in parallel. Although the overall computational cost may be small, the time-to-solution for a sequential sampling with high-fidelity numerical hydrodynamic methods is large. Generally, although statistics-focused techniques have been shown to be useful and accurate, a major limitation in the context of this dissertation's objectives is that they do not retain the underlying temporal response and lose the ability to understand the mechanisms that trigger an extreme event. Therefore, they would only be able to satisfy the probabilistic quantification pursuit of the desired framework but not the observation aspects.

1.3.2 Prediction-Focused Surrogates

A prediction-focused methodology builds surrogate models that focus on reducing the computational cost per event by building a surrogate through System Identification (SI), as shown in Figure 1.12, to provide temporal predictions that are representative of the numerical hydrodynamic method. Unlike a statistics-focused methodology, a prediction-focused surrogate model retains the temporal response information required to understand how different DoFs interact and the mechanisms that trigger an extreme. In recent years, neural networks and Long Short-Term Memory (LSTM) neural networks in particular, have increased in popularity for system identification of ship responses as well as for marine dynamics in general. *Xu* (2020) produced several case studies with a methodology developed with LSTM neural networks for different marine dynamics problems such as a nonlinear wave propagation, nonlinear ship roll described by an ODE, a sloshing tank, and a simplified floating object in irregular waves with URANS. Additionally, *del Águila Ferrandis et al.* (2021) utilized standard Recursive Neural Networks (RNN), LSTM, and Gated Recurrent Units (GRU) architectures to represent the Three Degrees-of-Freedom (3-DoF) URANS predicted response of a vessel at constant speed and heading in random irregular waves.

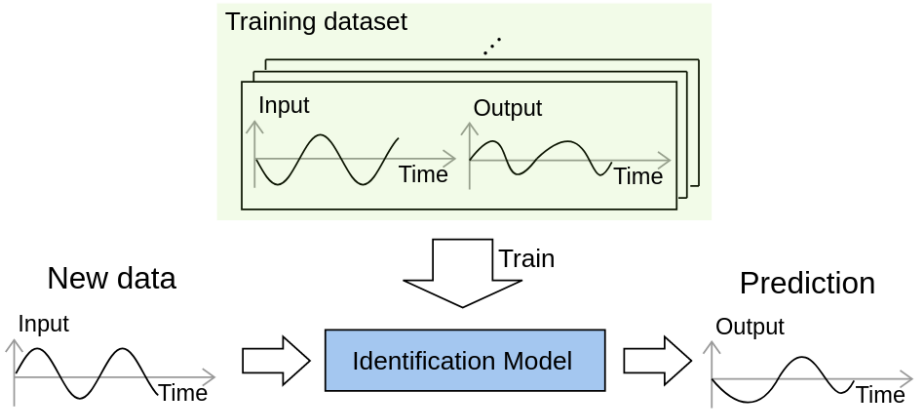

Figure 1.12: System identification flow chart from *Xu* (2020).

Xu (2020) and *del Águila Ferrandis et al.* (2021) both consider simplified cases of ship motion at either zero speed or constant speed and heading. Therefore, the exact path of the ship was known and the wave excitation along this path was utilized as an input into the surrogate model, while the output was the response of the vessel. *D'Agostino et al.* (2022) cast more emphasis on forecasting than solely system identification and utilized previous time steps of wave elevation and response quantities to forecast into the future for a free-running vessel in random irregular waves. The predictions seem to perform fairly well for the cases demonstrated in *D'Agostino et al.* (2022) but can only predict one or two waves into the future. A short-term forecast, as shown in Figure 1.13, in an extreme event framework would require multiple forecasts into the future, utilizing previous predictions as inputs, to produce a prediction with enough exposure time to realize a wave environment that leads to an extreme. With each sequential model prediction, the error from the previous prediction has the possibility of compounding and causing erroneous results.

Out of all the surrogate modeling methods reviewed, the LSTM neural network method has the most potential of accomplishing the overarching objectives of this dissertation when creating surrogate models for nonlinear ship dynamics. After training, LSTM neural networks allow for highly computationally efficient predictions of the temporal response that helps formulate the extreme statistics, while maintaining the ability to understand the mechanisms behind them. However, the previous research reflects few examples of application to free-running vessels and extreme events in general. Typical case studies have focused on simplified problems in random wave fields. If LSTM neural networks are to be incorporated into a framework with a probabilistic method and numerical hydrodynamic method, the resulting modeling methodology must be able to handle any extreme response for free-running vessels, as well as arbitrary operating and environmental conditions.

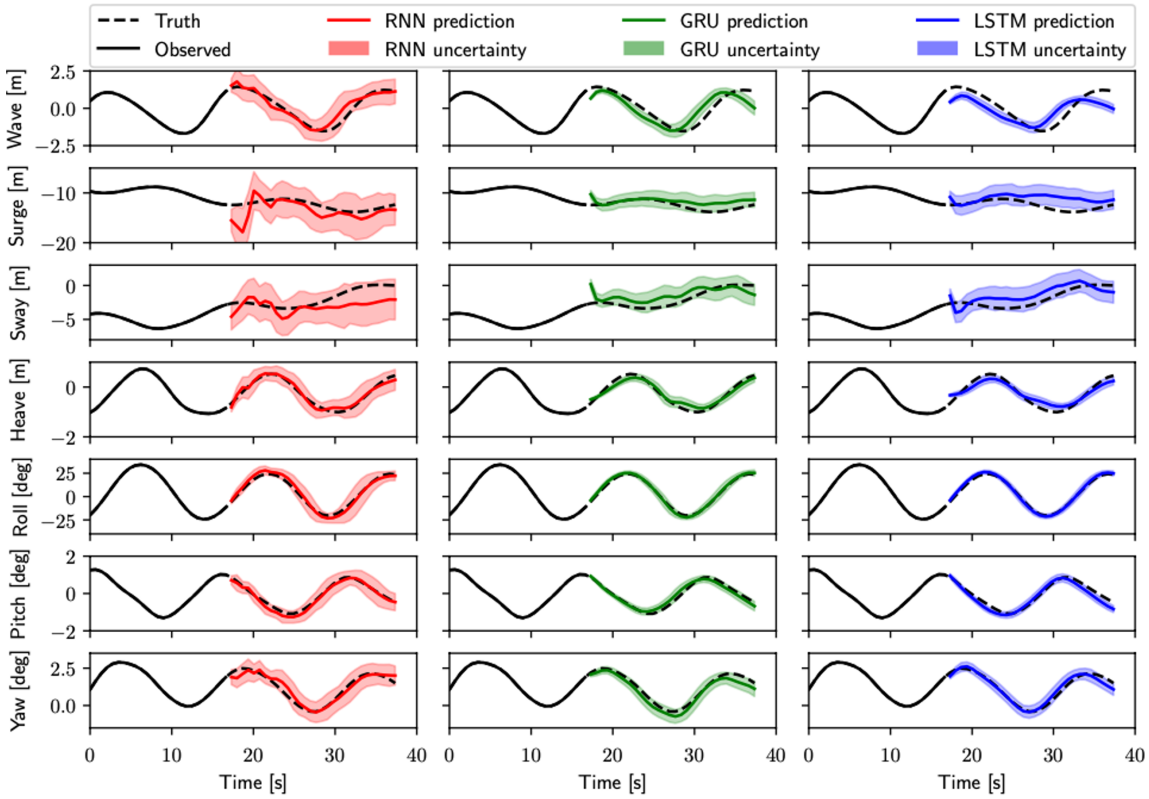

Figure 1.13: Examples of forecasts with different neural network architectures from *D'Agostino et al.* (2022).

1.4 Overview of Thesis

A large volume of critical research has been produced in the areas of extreme probabilistic methods, numerical hydrodynamic simulation approaches, and surrogate modeling techniques for ship responses in waves. Sections 1.1 through 1.3 review some of the most pertinent methods to the extreme ship response problem. Individually, none of the research areas alone can produce a quantitative analysis of extreme events with high fidelity. Although significant progress has been made in each area, they have historically been developed and researched independently of one another, with little interaction between the state-of-the-art methods in each area. Recent research has resulted in the incorporation of surrogate models in probabilistic methods and numerical hydrodynamic methods separately. However, simulations of ship responses

in waves with higher-fidelity numerical hydrodynamic methods have typically only considered simplified and canonical cases and have not been fully immersed into a probabilistic method for free-running vessels. This disconnect has created a gap in the literature of a framework capable of addressing all of the challenges of the extreme ship response problem, and allows for the efficient observation and probabilistic quantification of arbitrary extreme ship response events. Of the reviewed literature, the CWG probabilistic method, CFD (more specifically URANS) numerical hydrodynamic methods, and LSTM neural networks for surrogate modeling, provide the greatest potential to perform high fidelity observations of extreme events and quantify their probability.

This dissertation develops the *CCS* framework which utilizes the **C**WG probabilistic method for generating wave group descriptions and handling the probability calculations, **C**FD which produces observations of extreme events through simulation, and LSTM neural networks to develop a **S**urrogate model of the CFD predictions to reduce the overall computational cost of the framework. In their current state, none of the methodologies explored are capable of combining into a framework immediately and require modification and advancement prior to their integration. The CWG method has only been implemented with 1-DoF ODE models of the ship response, where the encounter condition can be prescribed as an initial condition and the wave groups are not physically realizable. CFD methods are computationally expensive and require simulations be short to reduce the cost but long enough to generate waves in both time and space to observe the generated extreme events. Additionally, there are not any instances of LSTM neural networks or other prediction-focused surrogate modeling techniques producing models that are accurate enough to predict extreme events for free-running vessels traveling in large-amplitude waves.

This dissertation expands upon the author's published research that shape the foundation of the developed methodologies (*Xu et al.*, 2021; *Silva and Maki*, 2021a,b,

2022b,a, 2023; *Silva et al.*, 2021, 2022; *Knight et al.*, 2022). Complete descriptions of each methodology, technique, and case study developed in the previous publications by the author are included and expounded upon in this dissertation for completeness.

Chapter I gives an overview of the extreme ship response problem and relative literature associated with it. The literature review is broken into the areas of probabilistic methods, numerical hydrodynamics, and surrogate modeling techniques. Chapter II provides a detailed description of the CWG method in the context of this dissertation. This chapter details how the probability of exceedance problem is formulated, the way in which wave groups are constructed, and how the methodology is practically implemented. Chapter III provides an overview of the CFD solver and methodology considered in this dissertation for the case studies. The chapter details the boundary conditions, the wave generation methodology, and the propeller and rudder models that are employed to produce free-running simulations.

Both Chapter IV and V describe critical components of the CCS framework. Chapter IV gives an overview of initial conditions and how to implement and enforce them practically within an extreme ship response framework, using either high-fidelity numerical hydrodynamic tools or experiments. The chapter introduces the idea of the *natural initial condition* which is fundamental in the implementation of the CWG method with CFD. Additionally, Chapter IV provides a case study demonstrating how uncertainty in the enforcement of initial conditions can be quantified within the CCS framework. Chapter V describes LSTM neural networks in more detail and gives an overview of an SI methodology developed in this dissertation to represent the Six Degrees-of-Freedom (6-DoF) response of a free-running vessel in large-amplitude waves. This chapter also provides several case studies demonstrating the ability of the methodology to represent the 6-DoF response in random irregular waves for course-keeping, turning circles, as well as multiple speeds, headings, and sea states.

Chapter VI describes the CCS framework developed in this dissertation. The

chapter details how the CWG method, CFD, and LSTM neural networks are combined and the ways in which they work together to produce observations of extreme events and quantify the probability of their occurrence.

Chapter VII implements CCS framework and details a case study for a 2-D midship section of the ONRT in Sea State 7 beam seas that is only free to heave and roll. The case study presents an implementation of the CCS framework with and without the LSTM neural networks to understand both the accuracy of the framework as well as the accuracy of the surrogate modeling technique for extremes. Example observation time-history predictions, the extreme statistics, and the computational cost of the framework are discussed for the case study.

Chapter VIII extends the case study in Chapter VII to a free-running a 3-D ONRT in Sea State 7, traveling in stern-quartering seas and free in all 6-DoF. The case study tests the ability of the CCS framework to handle arbitrary frames of encounter when enforcing initial conditions as well as the ability of the LSTM neural networks to represent the 6-DoF vessel response. Finally, Chapter IX concludes the dissertation, discusses its specific contributions, and provides suggestions for future opportunities of expansion.

Throughout the dissertation, the primary focus is aimed at producing a framework that can provide quantitative observations of the extremes and quantify the probability of their occurrence. An additional focus will be placed on reducing the overall computational cost of the framework. Striking this balance between accuracy and cost is a crucial consideration that is a major theme throughout the dissertation.

CHAPTER II

Critical Wave Group (CWG) Method

The CWG method is a probabilistic framework for observing and quantifying extreme ship response events that was first developed for regular waves in *Themelis and Spyrou* (2007) and later extended to irregular waves in *Anastopoulos et al.* (2016); *Anastopoulos and Spyrou* (2016, 2017, 2019). This dissertation relies heavily on the probabilistic description and wave group construction techniques presented in *Anastopoulos and Spyrou* (2019) and this chapter will describe the CWG method as it is implemented within the developed CCS framework.

2.1 Probability of Exceedance

The CWG method is concerned with the calculation of the probability that a given response ϕ exceeds a threshold ϕ_{crit}. Due to the randomness of the ocean and the larger number of waves a vessel will experience throughout its lifetime. The CWG method assumes that a given ship response ϕ is a function of the wave group that causes an external excitation on the ship, and the motion state of the vessel at the moment the wave group is encountered, referred herein as the *encounter condition*, but also sometimes referred to as the *initial condition*. For sample spaces of arbitrary parameterized wave groups, G, and encounter conditions, E, a probability

of exceedance can be generally defined as:

$$p\left[\phi > \phi_{\text{crit}}\right] \;=\; \int \mathbf{1}_{\Theta(g,e)>\phi_{\text{crit}}} f_{G,E}\left(g,e\right) dg\, de \tag{2.1}$$

where $f_{G,E}\left(g,e\right)$ is the joint PDF of wave groups and encounter conditions, Θ is a mapping describing the absolute maximum response for a given wave group and encounter condition ($\phi = \Theta\left(G,E\right)$), and $\mathbf{1}_{\Theta(g,e)>\phi_{\text{crit}}}$ is an indicator function that denotes a result of one when a particular wave group/encounter condition pair exceeds a given threshold, and an output of zero when it does not. To evaluate Equation 2.1, simulations or experiments of the ship response due to different wave groups and encounter conditions are needed to develop the mapping Θ. However, the stochastic nature of the ocean and the infinite possible combinations of wave groups and encounter conditions renders a full description of Θ to be expensive and akin to a Monte Carlo-type approach. Therefore, the CWG method focuses on defining the boundary created by the indicator function in Equation 2.1. The corresponding wave groups and encounter conditions along this indicator function boundary lead to responses that cause a near-exceedance of the specified response threshold. These wave groups are referred to as the *critical* wave groups.

Equation 2.1 is general and does not make any assumption about the shape of the wave groups or the nature of the encounter conditions. However, if the wave groups are parameterized in such a way that their shape is similar with time and only the height of the waves in the groups is varied, then an assumption can be made that any wave group of similar shape that is larger than the critical wave group for a particular encounter condition will also lead to an exceedance. Figure 2.1 shows an example of a normalized wave elevation time-history η/H_s and the corresponding response ϕ/ϕ_{crit} for wave groups with the same shape that starts at dimensionless time $t/T_p = 0$. H_s and T_p correspond to the significant wave height and peak modal period of the wave

field, respectively. By prescribing the same encounter condition and increasing the height of the waves in the wave groups, a critical wave group can be determined that leads to a near exceedance. Proper identification of the critical wave groups allows for Equation 2.1 to be evaluated without a complete description of Θ, thus reducing the computational cost of the probability calculations.

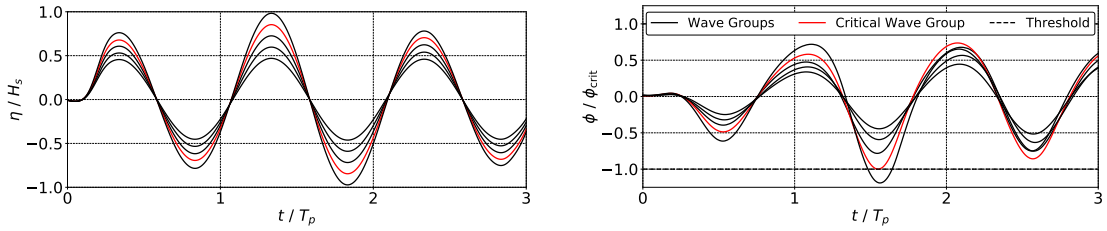

(a) Wave Groups

(b) Response

Figure 2.1: Identification of a critical wave group for a given set of wave groups with similar shapes.

In order to evaluate Equation (2.1) practically, the wave groups must be parameterized to take advantage of the concept of critical wave groups. If wave groups are parameterized by an arbitrary shaping parameter q and encounter conditions ec_k, Equation 2.1 can be rewritten as:

$$p\left[\phi > \phi_{\text{crit}}\right] = \sum_{k} p\left[\bigcup_{q} wg_{k,q}, ec_k\right] \tag{2.2}$$

where ec_k is the k^{th} encounter condition, and $wg_{k,q}$ are all the wave groups for the k^{th} encounter condition and q^{th} wave group shape that lead to the response exceeding a specified threshold. Each of the wave groups in $wg_{k,q}$ are either critical wave groups or larger than their respective critical groups. Since the wave group shaping q is arbitrary, there is a possibility of waves and groups that are not mutually exclusive, such as a single wave being a part of a two-wave group or a two-wave group being a part of a three-wave group. Therefore, the wave group probabilities in Equation 2.2 are combined with a union, with respect to q.

To properly evaluate the wave group and encounter condition probabilities separately, Equation 2.2 can be written as:

$$p\left[\phi > \phi_{\text{crit}}\right] = \sum_{k} p\left[\bigcup_{q} wg_{k,q} | ec_k\right] \times p\left[ec_k\right] \tag{2.3}$$

Equation 2.3 is an example of the principle of separation (*Belenky et al.*, 2012). $p\left[ec_k\right]$ is the probability of encounter conditions and corresponds to the non-rare portion of the problem, while $p\left[\bigcup_q wg_{k,q} | ec_k\right]$ is the rare portion of the problem and contains the probability of the threshold-exceeding wave groups. Since the wave groups $wg_{k,q}$ are defined as all the wave groups for the k^{th} encounter condition and q^{th} wave group shape that lead to the response exceeding a specified threshold, the conditional relation of ec_k in Equation 2.3 is not necessary and probability of exceedance can be further simplified to:

$$p\left[\phi > \phi_{\text{crit}}\right] = \sum_{k} p\left[\bigcup_{q} wg_{k,q}\right] \times p\left[ec_k\right] \tag{2.4}$$

An important consideration in a practical implementation of the CWG method is a proper parameterization of the wave groups and the shaping parameter q. *Anastopoulos and Spyrou* (2017, 2019) developed the methodology of constructing a set of mutually exclusive and collectively exhaustive wave groups by classifying wave groups in terms of their run length j and m wave period groupings, which translates Equation 2.4 to:

$$p\left[\phi > \phi_{\text{crit}}\right] = \sum_{k} \sum_{m} p\left[\bigcup_{j} wg_{m,j}^{(k)}\right] \times p\left[ec_k\right] \tag{2.5}$$

where $wg_{m,j}^{(k)}$ are all the wave groups leading to a threshold exceedance with j waves, wave periods in the m^{th} wave period range, and the k_{th} encounter condition. To avoid overlap in wave groups, the union with respect to j remains, but the probability summation is now with respect to k encounter conditions and m wave period ranges,

but do not intersect.

To enable the solution of Equation 2.5, *Anastopoulos and Spyrou* (2017, 2019) assumed that for sufficiently large response thresholds, the wave groups $wg_{m,j}^{(k)}$ were rare events and statistically independent of one another. With this assumption of independence, De Morgan's law can be applied to remove the union with respect to j and results in the following final parameterized probability of exceedance calculation:

$$p\left[\phi > \phi_{\text{crit}}\right] = \sum_{k} \sum_{m} \left(1 - \prod_{j} \left(1 - p\left[wg_{m,j}^{(k)}\right]\right)\right) \times p\left[ec_k\right] \tag{2.6}$$

where the probability of exceedance is broken into two main calculations: the probability of the k^{th} encounter condition $p\left[ec_k\right]$, and the probability of wave group exceedance $p\left[wg_{m,j}^{(k)}\right]$, for the m^{th} wave period range, j waves in the group, and the k^{th} encounter condition.

The probability of encounter conditions can be found through observations of the vessel response in random waves. In all the previous research with the CWG method, the response of interest was the roll angle, which was modeled with a 1-DoF second-order ODE. Therefore, the ship state at the moment of encountering the wave group was described by the roll and roll velocity. Figure 2.2 represents an example of several random wave observations of the roll and roll velocity and the associated joint PDF. Figure 2.2b must be discretized to provide a set of collectively exhaustive and mutually exclusive encounter conditions for consideration when identifying the critical wave groups. The probability of each encounter condition is found through the integration of the PDF for each discrete region corresponding to an evaluated encounter condition. More discussion on the selection and enforcement of encounter conditions can be found in Chapters IV and VI.

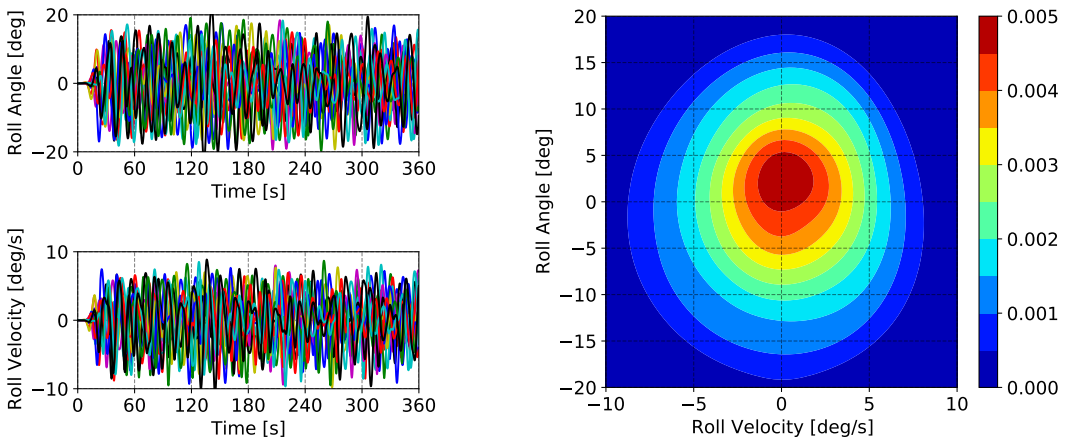

(a) Random Wave Observations

(b) Probability

Figure 2.2: Example of calculation of probability of encounter conditions.

The probability of wave group exceedance, $p\left[wg_{m,j}^{(k)}\right]$, is the probability of all the wave groups with a shape defined by the indices m and j that lead to a response threshold exceedance for the encounter condition k, and can be defined as:

$$p\left[wg_{m,j}^{(k)}\right] \;=\; p\left[\mathbf{H}_j > \mathbf{h}_{cr,j,m}^{(k)}, \mathbf{T}_j \in T_{cr,m}\right] \tag{2.7}$$

where the probability of wave group exceedance is equal to the probability that the heights of each individual wave in a given wave group, $\mathbf{H}_j$, are larger than those of the critical wave group $\mathbf{h}_{cr,j,m}^{(k)}$, and that the wave periods of the given wave group $\mathbf{T}_j$ are within the range $T_{cr,m}$ of the critical wave group.

2.2 Wave Group Construction

The concept of identifying critical wave groups provides a means for calculating the extreme probability of ship responses through the evaluation of Equation 2.7, in particular. However, the parameterization of wave groups by the number of waves in the group and the wave period range of waves in the group does not provide any insight into the height of the waves in the group. *Kimura* (1980) introduced the idea

that successive wave heights and periods can be modeled as Markov chains. Markov chains contain a memorylessness property where the future state only depends on the current state and not anything else that occurred prior to the current state. In the case of wave successions, it means the attributes of a wave only depend on the attributes of the waves that directly precede or follow it. The Markov chain wave group model developed in *Kimura* (1980) considered wave heights and periods separately and did not contain any cross-correlation that are present between successive wave heights and periods. *Anastopoulos et al.* (2016) improved the Markov chain wave group model developed in *Kimura* (1980) in order to create a systematic procedure of constructing irregular wave groups that match the parameterization needed for Equation 2.7.

Equations 2.8 and 2.9 demonstrate how the period of the *most expected* successive wave $\overline{t_n}$ can be calculated based off the current wave height h_{n-1} and period t_{n-1}, as well as the conditional PDF (or transition kernel) that represents the relationship between the succeeding wave period t_n, based on the current wave's height and period. The integration region $T_{cr,m}$ limits the prediction of wave period to fall within the wave period range of interest. The transition kernels and all of the marginal and joint PDFs required for the wave group portion of the CWG method can be developed through either observations of the wave field in a purely data-driven manner, or through spectral methods where parameters are tuned utilizing limited observations of the wave field and theoretical relationships between successive wave heights and periods through the use of copulas (*Anastopoulos et al.*, 2016). This dissertation develops all of the statistical relationships of successive waves through observations of the random wave field, which Chapter VI describes in further detail.

$$\overline{t_n} = \frac{1}{p_{T_n}} \int_{T_{cr,m}} t_n f_{T_n|H_{n-1},T_{n-1}}\left(t_n|h_{n-1},t_{n-1}\right) dt_n \tag{2.8}$$

$$p_{T_n} = \int_{T_{cr,m}} f_{T_n|H_{n-1},T_{n-1}}\left(t_n|h_{n-1},t_{n-1}\right) dt_n \tag{2.9}$$

Anastopoulos and Spyrou (2019) introduced the idea of also considering the Markov chain prediction of wave period in the prediction of the successive wave height in Equation 2.10. Therefore, the transition kernel now considers the relationship for the *most expected* successive wave height $\overline{h_n}$, based on the Markov chain predicted wave period $\overline{t_n}$ and the current wave height h_{n-1}, as well as period t_{n-1}.

$$\overline{h_n} = \int_0^\infty h_n f_{H_n|T_n,H_{n-1},T_{n-1}}\left(h_n|\overline{t_n},h_{n-1},t_{n-1}\right) dh_n \tag{2.10}$$

Due to the memorylessness property of Markov chains, each individual wave prediction only depends on the waves directly preceding or succeeding it. By selecting the height, H_c, and period, T_c, of the largest wave in a given wave group, the height, $\overline{h_n}$, and period, $\overline{t_n}$, of the most likely preceding and following wave can be determined from Equations (2.8) through (2.10). The Markov chain assumption dictates that any wave only depends on the wave that either precedes it or follows it; thus, once waves are predicted from the largest wave in the group, the next series of waves can be found from the previous predictions, and so on, to build a full wave group. Therefore, a wave group can be uniquely described by the H_c, T_c, and j.

The Markov chain procedure produces heights and periods of each wave in a particular group. However, to evaluate the corresponding ship response to a particular wave group, those heights and periods must be constructed into a continuous temporal representation. Figure 2.3 shows an example time-history of a wave group with the heights and periods predicted by the Markov chains. For each wave in the group, the crest and trough are assumed to each be half the wave height, and the time derivative of wave elevation is set to zero at the crest and trough to ensure they are peaks. Also, the crest and trough occur at the center of the time interval defined by the successive

zero-crossings, and the zero-crossings occur at instances of half of the current wave period. This dissertation assumes symmetry between the crest and troughs for each wave, but extension to nonlinear wave fields in future research should investigate how to allow for asymmetry between peaks and troughs. With these geometric constraints, trigonometric interpolation can be performed following the research of *Anastopoulos and Spyrou* (2019) and *Nathan* (1975) to build a continuous time representation of each wave group. Figure 2.4 provides an example of wave groups with the same T_c and j, but with a varying H_c, to illustrate how the Markov chain predictions predict the successive waves. σ in Figure 2.4 corresponds to the standard deviation of the wave height from random observations.

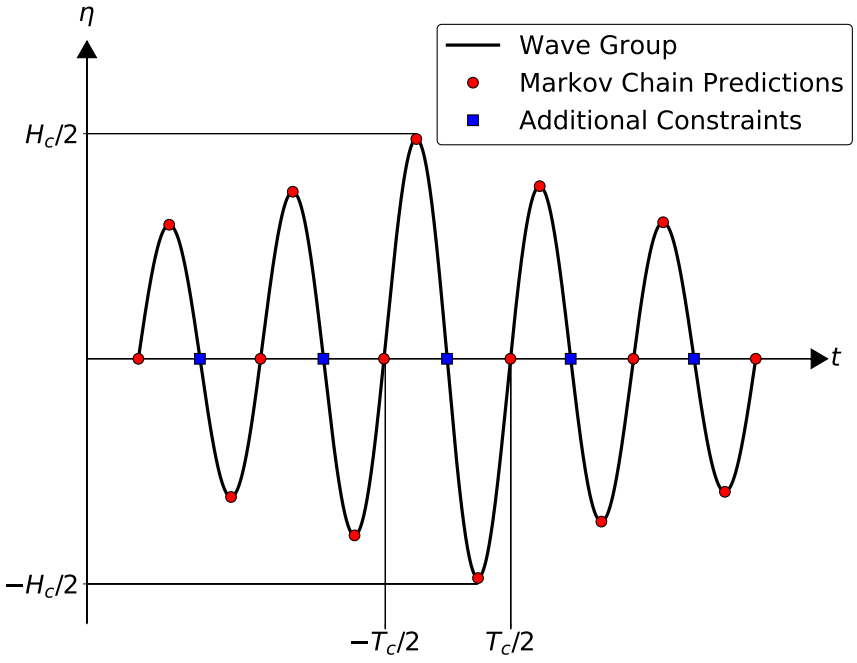

Figure 2.3: Markov chain construction of wave groups and additional geometric constraints (figure adapted from *Anastopoulos and Spyrou* (2016)).

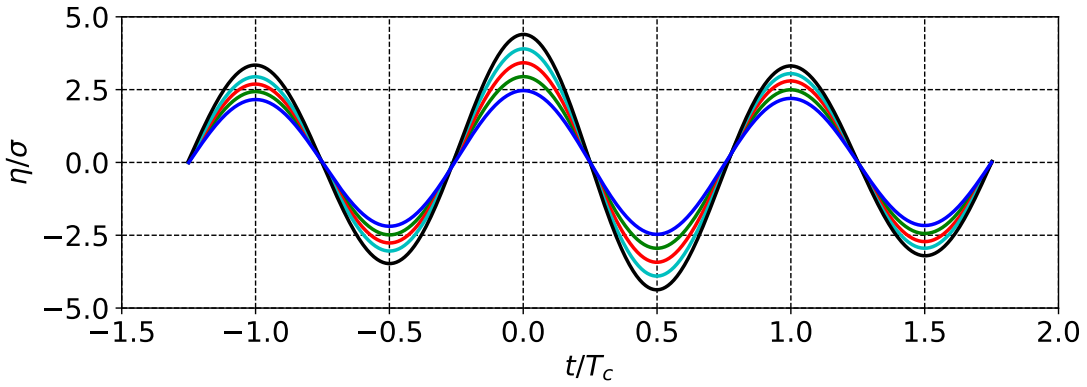

Figure 2.4: Ensemble of wave groups with the same T_c, j, and $H_c = 5\sigma$, 6σ, 7σ, 8σ, and 9σ.

2.3 Wave Group Probability

The Markov chain predictions provide a methodology for producing a wave group that can be utilized to predict the corresponding ship response and identify the critical wave groups. Markov chains can also be considered when evaluating the probability that a wave group exceeds the critical wave group. For a single wave, $j = 1$, Equation 2.7 reduces to:

$$p\left[wg_{m,1}^{(k)}\right] \;=\; p\left[H_1 > h_{cr,1,m}^{(k)}, \mathbf{T}_1 \in T_{cr,m}\right] \;=\; p\left[H_1, T_1\right] \tag{2.11}$$

where H_i corresponds to the i^{th} wave in the group exceeding the height of the i^{th} wave in the critical wave group and T_i resides in the region defined by $T_{cr,m}$. The notation of H_i and T_i in Equations 2.12 through 2.14 is intended to simplify the probability calculations for wave groups with more than one wave. Equation 2.11 corresponds to the joint probability of the single wave exceeding a critical wave height and the modal period of the wave being in the range of interest.

For two consecutive waves, $j = 2$, Equation 2.11 expands to:

$$\begin{aligned} p\left[wg_{m,2}^{(k)}\right] &= p\left[H_1, H_2, T_1, T_2\right] \\ &= p\left[T_1, T_2 | H_1, H_2\right] \times p\left[H_1, H_2\right] \end{aligned} \tag{2.12}$$

and increases in complexity for three consecutive waves, $j = 3$ to:

$$\begin{aligned} p\left[wg_{m,3}^{(k)}\right] &= p\left[H_1, H_2, H_3, T_1, T_2, T_3\right] \\ &= p\left[H_3, T_3 | H_1, H_2, T_1, T_2\right] \times p\left[H_1, H_2, T_1, T_2\right] \\ &= p\left[H_3, T_3 | H_2, T_2\right] \times p\left[wg_{m,2}^{(k)}\right] \\ &= \frac{p\left[H_2, H_3, T_2, T_3\right]}{p\left[H_2, T_2\right]} \times p\left[wg_{m,2}^{(k)}\right] \\ &= \frac{p\left[T_2, T_3 | H_2, H_3\right]}{p\left[H_2, T_2\right]} \times p\left[H_2, H_3\right] \times p\left[wg_{m,2}^{(k)}\right] \end{aligned} \tag{2.13}$$

In Equation 2.13, the Markov chain assumption from *Anastopoulos and Spyrou* (2019) is employed to simplify the conditional probability by assuming that H_3 and T_3 do not depend on H_1 and T_1. Additionally, in the probability of three consecutive waves appears the probability of two consecutive waves, and the same observation is true for larger values of j. Therefore, Equation 2.7 can be generalized to:

$$p\left(\mathbf{H}_j, \mathbf{T}_j\right) = p\left(H_1, T_1\right) \prod_{j=2} \frac{p\left(T_{j-1}, T_j | H_{j-1}, H_j\right) p\left(H_{j-1}, H_j\right)}{p\left(H_{j-1}, T_{j-1}\right)} \tag{2.14}$$

Following the research of *Anastopoulos and Spyrou* (2019), Equation 2.7 can be rewritten as:

$$p\left[wg_{m,j}^{(k)}\right] = p_0 \times \prod_{n=2}^{j} \frac{p_1^{(n)} \times p_2^{(n)}}{p_{01}^{(n-1)} \times p_{02}^{(n-1)}} \tag{2.15}$$

where Equations 2.16 through 2.20 elaborate the calculation of p_0, $p_1^{(n)}$, $p_2^{(n)}$, $p_{01}^{(n)}$, and $p_{02}^{(n)}$ respectively, and provide a systematic probability calculation for any Markov

chain wave group with arbitrary j.

$$p_1^{(n)} = \int_{T_{cr,m}} \int_{T_{cr,m}} f_{T_n,T_{n-1}|\mathbf{H}_n}\left(t_n, t_{n-1}|\mathbf{H}_n > \mathbf{h}_{cr,n}\right) dt_n dt_{n-1} \tag{2.16}$$

$$p_2^{(n)} = \int_{h_{cr,n}}^{+\infty} \int_{h_{cr,n}}^{+\infty} f_{H_n,H_{n-1}}\left(h_n, h_{n-1}\right) dh_n dh_{n-1} \tag{2.17}$$

$$p_{01}^{(n)} = \int_{T_{cr,m}} f_{T_n|\mathbf{H}_n}\left(t_n|\mathbf{H}_n > \mathbf{h}_{cr,n}\right) dt_n \tag{2.18}$$

$$p_{02}^{(n)} = \int_{h_{cr,n}}^{+\infty} f_{H_n}\left(h_n\right) dh_n \tag{2.19}$$

$$p_0 = p_{01}^{(1)} \times p_{02}^{(1)} \tag{2.20}$$

CHAPTER III

Computational Fluid Dynamics (CFD)

This chapter describes the CFD solver utilized throughout the case studies in this dissertation. The CFD simulations were performed with the open-source toolkit OpenFOAM® v2006 with customized CFD solvers and libraries developed for simulating ship responses in nonlinear seaways by the CSHL at The University of Michigan (*Filip et al.*, 2017; *Piro and Maki*, 2013). The flow field is described by the incompressible URANS equations, where the conservation of mass and momentum respectively are:

$$\nabla \cdot \mathbf{u} \;=\; 0 \tag{3.1}$$

$$\frac{\partial \rho \mathbf{u}}{\partial t} + \nabla \cdot \rho \mathbf{u}\mathbf{u} = -\nabla p + \rho \mathbf{g} + \nabla \cdot \left[\mu_{\text{eff}} \left(\nabla \mathbf{u} + \nabla \mathbf{u}^{\text{T}}\right)\right] - \rho \mathbf{f}_{\mathbf{u}} \tag{3.2}$$

where ρ is the fluid density, $\mathbf{u}$ is the fluid velocity vector, p is the pressure, $\mathbf{g}$ is the gravity vector, $\mathbf{f}_{\mathbf{u}}$ is a relaxation source term, and μ_{eff} is the effective dynamic viscosity, which is equal to the sum of the physical viscosity μ, and the eddy viscosity μ_T. This dissertation employs a $k-\omega$ SST turbulence model (*Menter et al.*, 2003) to solve for the eddy kinematic viscosity ν_T, which is then translated to the eddy dynamic viscosity as $\mu_T = \rho \nu_T$

The two-phase flow in URANS is achieved through a Volume-of-Fluid (VOF)

method where the water and air are distinguished with a volume-fraction parameter α, where an α value of one denotes to water, and a value of zero corresponds to air, and anything greater than zero but less than one is the air-water interface region. The transport of α in space and time is described by:

$$\frac{\partial \alpha}{\partial t} \; + \; \nabla \cdot \mathbf{u}\alpha \; + \; \nabla \cdot \mathbf{w}\left(\alpha\left(1 \; - \; \alpha\right)\right) + f_{\alpha} \; = \; 0 \tag{3.3}$$

where $\mathbf{w}$ is a compression velocity that acts normal to the air-water interface and prevents diffusion to maintain a sharp interface and f_{α} is a relaxation source term. The volume fraction is introduced into Equations 3.1 and 3.2 through the density and viscosity fields described for the two-phase flow by:

$$\rho\left(\mathbf{x}, t\right) \; = \; \rho_{w}\alpha\left(\mathbf{x}, t\right) \; + \; \rho_{a}\left(1 \; - \; \alpha\left(\mathbf{x}, t\right)\right) \tag{3.4}$$

$$\mu\left(\mathbf{x}, t\right) \; = \; \mu_{w}\alpha\left(\mathbf{x}, t\right) \; + \; \mu_{a}\left(1 \; - \; \alpha\left(\mathbf{x}, t\right)\right) \tag{3.5}$$

where ρ_w and ρ_a are the density of water and air, respectively, and μ_w and μ_a are the dynamic viscosity of water and air, respectively.

A tightly-coupled algorithm is implemented to solve the rigid-body and fluid equations, where the fluid is acted upon by the body through a no-slip velocity boundary condition on the moving body, while the fluid provides external forcing on the body. Within each time step, an explicit acceleration relaxation technique is applied to ensure that the coupling between the fluid and body stays numerically stable. Body motion is achieved through an Arbitrary Lagrangian-Eulerian (ALE) method, where the entire domain translates and rotates with the body motions.

3.1 Wave Generation

Waves within the OpenFOAM® simulations are generated with the `waves2Foam` toolkit (*Jacobsen et al.*, 2012) with a modified version of the solver, `waveDyMFoam`. All the waves simulated in CFD for the present dissertation utilized the earth-fixed irregular wave description:

$$\eta\left(\mathbf{x},t\right) \;=\; \sum_{f} a_f cos\left(\omega_f t \;-\; \mathbf{k}_f \cdot \mathbf{x} \;+\; \phi_f\right) \tag{3.6}$$

where $\eta\left(\mathbf{x},t\right)$ is the instantaneous wave elevation in both space and time, a_f, ω_f, and ϕ_f are Fourier components of amplitude, frequency, and phase, respectively, and $\mathbf{k}_f$ is the wavenumber, specified as a vector, to denote direction of the wave components. The wavenumber k_f, comes from the dispersion relation:

$$\omega_f^2 = g k_f \tanh(h k_f) \tag{3.7}$$

where g is acceleration due to gravity and h is the water depth. As h trends toward infinity for deep water, $\tanh(hk_f)$ approaches one and the dispersion relation simplifies to:

$$\omega_f^2 = g k_f \tag{3.8}$$

In addition to prescribing the wave description at the boundary, an implicit relaxation zone approach is also used to maintain wave propagation throughout the domain and blend the prescribed wave kinematics with the computed fluid solution. The implicit wave relaxation is imposed through an addition of a source term to the momentum and volume-fraction equations. For the momentum shown in Equation 3.2 and the volume-fraction transport in Equation 3.3, the relaxation source terms $\mathbf{f_u}$ and f_α can be described by:

$$\mathbf{f_u} = \frac{\chi\left(\sigma\right)}{\Delta t}\left(\mathbf{u} - \mathbf{u}_{\text{theory}}\right) \tag{3.9}$$

$$f_\alpha = \frac{\chi(\sigma)}{\Delta t}(\alpha - \alpha_{\text{theory}}) \tag{3.10}$$

where $\mathbf{u}$ and α are the calculated velocity and volume-fractions fields, respectively, $\mathbf{u}_{\text{theory}}$ and α_{theory} are the theoretical wave velocity and volume-fraction from the prescribed wave description, χ is a blending function described by Equation 3.11, σ is a non-dimensional radial coordinate, and Δt is the time step size.

$$\chi(\sigma) = 1 - \frac{\exp(\sigma^{3.5}) - 1}{\exp(1) - 1} \tag{3.11}$$

Figure 3.1 shows the cylindrical relaxation zones utilized in this dissertation, where a value of one for χ near the boundaries corresponds to a purely analytical wave description and a χ value of zero indicates a purely computational solution in the interior of the domain.

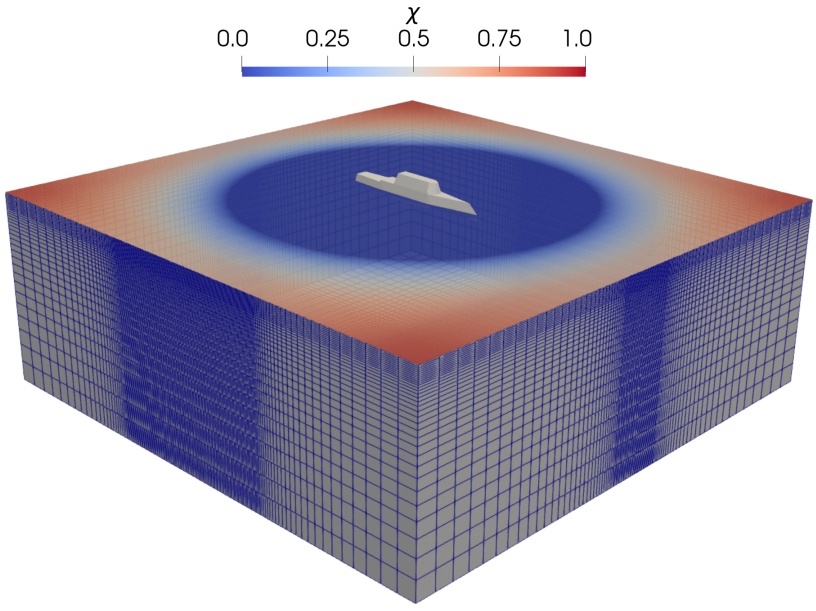

Figure 3.1: Depiction of the cylindrical relaxation zones and the associated relaxation weights.

The non-dimensional radial coordinate σ is calculated throughout the domain with Equation 3.12 to indicate the location of the relaxation zones through an inner radius r_i and outer radius r_o for dimensional radial coordinates r. Typical values of r_i

and r_o in terms of the ship's length between perpendicular (L_{pp}) are $1.2L_{pp}$ and $2L_{pp}$, respectively (*White*, 2020). The relaxation scheme described in Equations 3.9 through 3.12 and illustrated in Figure 3.1 allows for large amplitude waves to be generated and propagated accurately and also ensures that the relaxation techniques are not being applied too close to the vessel, which would interfere with the fluid-body solution.

$$\sigma(r) = \frac{r - r_i}{r_i - r_o} \quad \text{for} \quad r_i < r < r_o \tag{3.12}$$

3.2 Boundary Conditions

Solution of the governing equations described in Equations 3.1 through 3.3, and the $k - \omega$ SST turbulence model, require boundary conditions. Boundary conditions are required for the velocity $\mathbf{u}$, the dynamic pressure p', the volume fraction α, the eddy viscosity ν_T, the turbulent kinetic energy k, and dissipation rate ω. Table 3.1 lists of all the OpenFOAM® boundary conditions applied in the dissertation with a short description of each.

The computational domain shown in Figure 3.2 demonstrates how the domain boundaries are segmented into patches such as the *Top* patch in yellow, the *Inlet* in blue, and the *Hull* in red, where the *Hull* patch includes all of the appendages and relevant vessel geometry.

Table 3.1: Summary of OpenFOAM® boundary condition terminology.

Name	Description
fixedValue	Dirichlet boundary condition that applies a fixed value to either a scalar or vector field
zeroGradient	Neumann boundary condition where a zero normal gradient is applied.
inletOutlet	*fixedValue* is applied to cell faces with flux into the domain and *zeroGradient* is applied for cell faces with flux out of the domain.
pressureInletOutletVelocity	*zeroGradient* is applied to each velocity component for all outflow and assigns a *fixedValue* velocity based on the flux in the patch-normal direction. This condition works with the *totalPressure* boundary condition.
totalPressure	Applies a dynamic pressure $p' = -1/2\rho\|\mathbf{U}\|^2$ for inward flux and $p' = 0$ for outward flux and works with the *pressureInletOutletVelocity* boundary condition.
waveAlpha	Prescribes the volume fraction $\alpha(\mathbf{x}, t)$ at the boundary based on an analytical wave elevation and works with the *waveVelocity* boundary condition.
waveVelocity	Prescribes the velocity at the boundary based on an analytical wave velocity and works with the *waveAlpha* boundary condition.
movingWallVelocity	Applies the velocity $\mathbf{u}$ on the boundary patch from the equation of motion solver and enforces a no-slip condition.
nutkWallFunction	Provides a wall constraint on the turbulent viscosity ν_T based on the turbulent kinetic energy k.
kqRWallFunction	Provides a *zeroGradient* boundary conditions for the turbulent kinetic energy k.
omegaWallFunction	Applies a constraint on the specific dissipation rate ω and turbluence kinetic energy production contribution G.

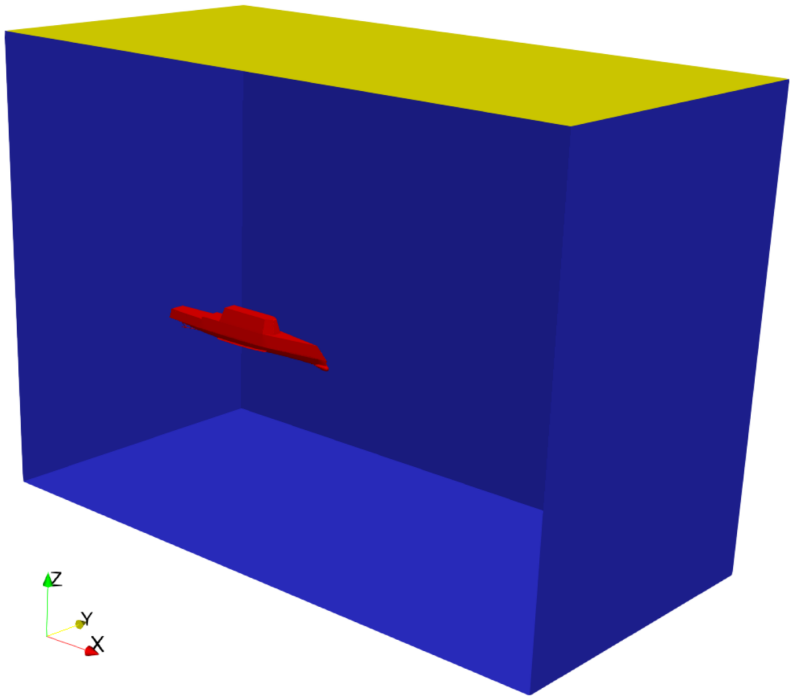

Figure 3.2: Separation of the computational domain boundaries into patches for $y \geq 0$.

Table 3.2 summarizes all the boundary conditions for the computational domain, separated by variables and patches. The *Top* boundary patch represents the atmosphere and considers the *pressureInletOutletVelocity* boundary condition for velocity, *inletOutlet* for α, *totalPressure* for p', and *zeroGradient* for all the turbulent quantities. The *Inlet* is responsible for handling the generation of the waves by prescribing the wave velocity and elevation at the boundary with *waveVelocity* and *waveAlpha*, respectively, *fixedFluxPressure* for p', and *inletOutlet* for the turbulent quantities. The final boundary patch is *Hull*, which corresponds to the entire vessel and all of its appendages. The no-slip boundary condition of the body is applied to the fluid through the *movingWallVelocity* boundary condition, while *zeroGradient* is enforced for *alpha*, *fixedFluxPressure* is applied to p', and the different wall functions are applied for the turbulent quantities.

Table 3.2: Summary of boundary conditions for each boundary patch in the CFD simulations.

Variable	Top	Inlet	Hull
$\mathbf{U}$	*pressureInletOutletVelocity*	*waveVelocity*	*movingWallVelocity*
α	*inletOutlet*	*waveAlpha*	*zeroGradient*
p'	*totalPressure*	*fixedFluxPressure*	*fixedFluxPressure*
ν_T	*zeroGradient*	*inletOutlet*	*nutkWallFunction*
k	*zeroGradient*	*inletOutlet*	*kqRWallFunction*
ω	*zeroGradient*	*inletOutlet*	*omegaWallFunction*

3.3 Propeller and Rudder Model

CFD-based seakeeping or maneuvering analysis with a discretized propeller and rudder can be accurate, but is computationally expensive and often requires the use of overset grids (*Shen et al.*, 2015). The computational expense is due to the small time and length scales required to resolve the flow around the propellers and rudders accurately. Body-force propeller models significantly reduce the computational cost of a free-running CFD simulation, but often apply simplifying assumptions such as using the open-water propeller curve and neglecting the propeller side-force (*Araki et al.*, 2012). The side force acting on the propeller can be significant on the maneuvering and seakeeping motions. The propeller side force contributes to sway and induces a yaw moment. The propellers operate in the behind condition and the hull-propeller interaction influences the forces of the propeller. One approach to maintain the accuracy of using a discretized propeller is to develop a data-driven propeller model that is trained with CFD simulations of the propeller operating in the behind condition, as developed by *Knight* (2021) and implemented for turning-circle and zig-zag maneuvers in *Knight et al.* (2022). *Knight et al.* (2020) demonstrated that the orbital-wave velocity and the behind condition effects are important to include in a propeller model for CFD seakeeping analysis in large amplitude waves.

The propeller and rudder model considered in this dissertation were developed and

implemented in the previous research of *Knight et al.* (2020); *Knight* (2021); *Knight et al.* (2022); *Silva et al.* (2022) and is included and described in this dissertation for completeness. The rudders operate in the wake of the hull, as well as the respective upstream propeller. When the rudder is discretized, it often requires overset grids and also that the upstream propeller force and body-force distribution be accurately modeled, if a propeller model is used. In this dissertation, a data-driven propeller model is trained with double-body CFD simulations with the propeller operating in the behind condition, employing the same approach as *Knight* (2021); *Knight et al.* (2022); *Silva et al.* (2022). The rudder forces are determined with the Whicker and Fehlner (WF) rudder model (*Whicker and Fehlner*, 1958). The effects of the hull and propeller wake on the rudder is modeled similarly to *Araki et al.* (2012). Wave velocity effects are accounted for by determining the analytical orbital wave velocity at the respective instantaneous propeller and rudder locations in the wave field.

The data-driven propeller model determines the axial force coefficient K_X in Equation 3.13 and the side force coefficient K_Y in Equation 3.14 for each propeller in terms of the axial force F_x, the side force F_y, the propeller revolution rate n, and the propeller diameter D.

$$K_X = \frac{F_x}{\rho n^2 D^4} \tag{3.13}$$

$$K_Y = \frac{F_y}{\rho n^2 D^4} \tag{3.14}$$

Eight CFD-based training simulations with the discretized propeller and undeflected rudder operating in the behind condition are used to develop a regression-based surrogate model for K_X and K_Y in terms of the advance coefficient J and the oblique flow angle at the propeller plane β_P. The eight training points are stratified in the J-β space that the vessel is expected to operate in during the free-running maneuver. The

CFD training simulations are described in *Knight et al.* (2022) and *Knight* (2021), in which the error of the data-driven propeller model is quantified in detail. The training simulations are performed with a double-body approximation, and unique forward speeds and drift angles are examined for each sample point. J is a function of the instantaneous surge velocity of the vessel u, the instantaneous analytical orbital wave velocity projected into the body frame u_w, n, and D as shown by Equation 3.15. β_P is defined by Equation 3.16 and is a function of the instantaneous sway velocity v, the instantaneous analytical orbital wave velocity projected into the sway degree of freedom of the body frame v_w, the longitudinal distance between the center of gravity of the vessel and the propeller plane d_{px}, the instantaneous yaw rate $\dot{\psi}$, u, and u_w.

$$J = \frac{u - u_w}{nD} \tag{3.15}$$

$$\beta_P = \tan^{-1}\left(\frac{v - v_w - d_{px}\dot{\psi}}{u - u_w}\right) \tag{3.16}$$

The wave velocities and the yaw rate are set to zero for the training simulations, which reduces the computational cost of training the model. When the propeller model is implemented in free-running CFD analysis, the wave velocities and yaw rate are accounted for. The form of the regression model is denoted in Equations 3.17 and 3.18. For a twin-screw vessel, symmetry can also be assumed to simplify the training. The CFD training simulations are performed with negative β_P, such that the starboard side is windward and the port side is leeward. During a free-running CFD simulation, when the sign of β_P changes, the side that is treated as windward and leeward switch, and the direction of the propeller side force changes as described in *Knight* (2021). The force in the axial direction and the side force are applied to the equations of motion, and the body-force is applied uniformly in the swept volume of each propeller. The yaw moment of the propeller M_{Pz}, defined by Equation 3.19, is

also applied to the equations of motion. M_{Pz} is a function of F_x, d_{px}, and F_y, as well as the lateral distance of the propeller from the center of gravity of the vessel d_{py}.

$$K_X = a_1 + a_2 J + a_3 J^2 + a_4 |\beta_P| + a_5 \beta_P^2 + a_6 J |\beta_P| \tag{3.17}$$

$$K_Y = b_1 + b_2 J + b_3 J^2 + b_4 |\beta_P| + b_5 \beta_P^2 + b_6 J |\beta_P| \tag{3.18}$$

$$M_{Pz} = -(F_y d_{px} + F_x d_{py}) \tag{3.19}$$

The WF rudder model implementation is performed similarly to *Knight et al.* (2022), with the exception that the wave orbital velocity effect is also accounted for, like in *Silva et al.* (2022). The rudder force depends upon the induced velocity of the upstream propeller for each respective rudder as shown by Equations 3.20 through 3.23. The axial velocity at the rudder plane is described by Equation 3.21, in terms of u, the wake fraction w, and u_w. The lateral velocity at the rudder plane is represented by Equation 3.22 in terms of v, v_w, $\dot{\psi}$, the straightening coefficient γ, and the longitudinal distance from the center of gravity to the rudder stock d_r. The velocity magnitude at each rudder is shown in Equation 3.23.

$$C_T = \frac{8 K_X}{\pi J^2} \tag{3.20}$$

$$U_x = u(1 - w) - u_w \tag{3.21}$$

$$U_y = \gamma(v - v_w - d_r \dot{\psi}) \tag{3.22}$$

$$u_R = \sqrt{(U_x \sqrt{1 + C_T})^2 + (U_y)^2} \tag{3.23}$$

The angle of attack of the rudder α_r, is calculated by Equation 3.24, which is a function of the rudder angle δ, U_y, U_x, and C_T. The WF rudder model (*Whicker and*

Fehlner, 1958) is considered to determine the coefficient of lift C_L and the coefficient of drag C_D of the rudder. The C_L is determined by Equation 3.25, in terms of the cross-flow drag coefficient $C_{Dc} = 0.9$, the aspect ratio of the rudder Λ, α_r, and the lift curve slope as defined by Equation 3.26. The lift curve slope is determined as a function of the Oswald efficiency factor ϵ, the aspect ratio Λ, and the sweep of the quarter-chord ϕ. The C_D is determined as a function of the minimum drag coefficient C_{do} and the C_L. The lift L_R and drag D_R are calculated as a function of the lateral surface area of the rudder S, ρ, and U_R as shown by Equations 3.28 through 3.29. L_R and D_R are used to determine the rudder axial force, side force, and yaw moment for each rudder. The force is applied to the equations of motion and is uniformly distributed to the respective rudder zone as a body force.

$$\alpha_r = \delta - tan^{-1}\left(\frac{U_y}{U_x\sqrt{1+C_T}}\right) \tag{3.24}$$

$$C_L = \left(\frac{\partial C_L}{\partial \alpha_r}\right)\alpha_r + \frac{C_{Dc}}{\Lambda}\alpha_r^2 \tag{3.25}$$

$$\frac{\partial C_L}{\partial \alpha_r} = \frac{2\pi\epsilon\Lambda}{cos\ \phi\sqrt{\frac{\Lambda^2}{cos^4\phi}+4}+1.8} \tag{3.26}$$

$$C_D = C_{do} + \frac{C_L^2}{\pi\Lambda\epsilon} \tag{3.27}$$

$$L_R = \frac{1}{2}\rho U_R^2 S C_L \tag{3.28}$$

$$D_R = \frac{1}{2}\rho U_R^2 S C_D \tag{3.29}$$

A Proportional–Integral–Derivative (PID) controller is implemented for the rudder motion to maintain heading during course-keeping. Given a desired heading ψ_d and the instantaneous yaw ψ and yaw rate $\dot{\psi}$ of the vessel, a proportional G_p, integral G_i,

and derivative G_d gain can be prescribed to calculate a rudder angle command with:

$$\delta_c = G_p(\psi_d - \psi) + G_i \int_0^t (\psi_d - \psi(\tau))d\tau - G_d\dot{\psi} \tag{3.30}$$

The propeller and rudder models considered in this dissertation neglect the effects of emergence above the free-surface. In the case studies described in this dissertation, propeller emergence does not occur until the extreme event and is a consequence of the event itself. Therefore, propeller emergence does not play a large role in influencing the extreme response of the vessel.

CHAPTER IV

Initial Conditions

The CWG method provides the most comprehensive means of both observing and quantifying the probability of extreme events, while CFD can provide high fidelity predictions of the ship responses in extreme waves. When combined, the CWG method can construct deterministic wave groups with associated probabilities and then CFD can simulate the wave groups with different encounter conditions to identify the critical wave groups that subsequently feed back into the CWG method to calculate the probability of exceedance at different thresholds. However, previous research with CWG and other wave group methods have not fully addressed the enforcement of encounter conditions prior to a sequence of waves of interest. Extreme events can be strongly nonlinear, and different encounter conditions are expected to influence the response for a wave group that leads to a large response. Traditionally, this encounter condition is referred to as the initial condition, which originates from previous research only considering 1-DoF roll ODE models. In the ODE models, the wave group starts instantaneously without any preceding wave information, Therefore, the encounter condition is the initial condition of the ODE.

The primary challenge of implementing CWG with CFD, or experiments, is that both the encounter state and wave group must be physically realizable and cannot be impulsively instantiated with initial conditions. With ODE models, the wave group

can instantaneously start just like the body motion, and does not require any preceding wave information. This is not physically possible and cannot be reproduced in an experimental or simulation environment. Wave groups need to be generated from a wavemaker and propagate in both space and time. When utilizing CFD or experiments, additional DoF that describe the fluid must also be considered in addition to the body state. The research of *Anastopoulos et al.* (2016); *Bassler et al.* (2019) proposes a mechanism (see Figure 4.1) to release the ship at a desired encounter condition. While restraining a model in a desired orientation and then releasing it at a prescribed time is difficult but possible, releasing the model with a desired velocity is much more difficult. To arrive at a velocity from rest, acceleration is necessary. The manner in which the model accelerates will influence the radiation force and wave field, and hence, influence the hydrodynamic response. The fact that such a release mechanism requires the selection of an acceleration profile now introduces an additional parameter that must be selected. It is not clear how to distinguish phenomena associated with the encounter conditions from that which is caused by the release method of the ship model. All of these experimental drawbacks also arise in application of the CWG in CFD. Even though a great deal of control exists within CFD to prescribe encounter conditions explicitly (like in ODE models), the impact of the acceleration or impulsive start of the body motion on its subsequent response is of concern.

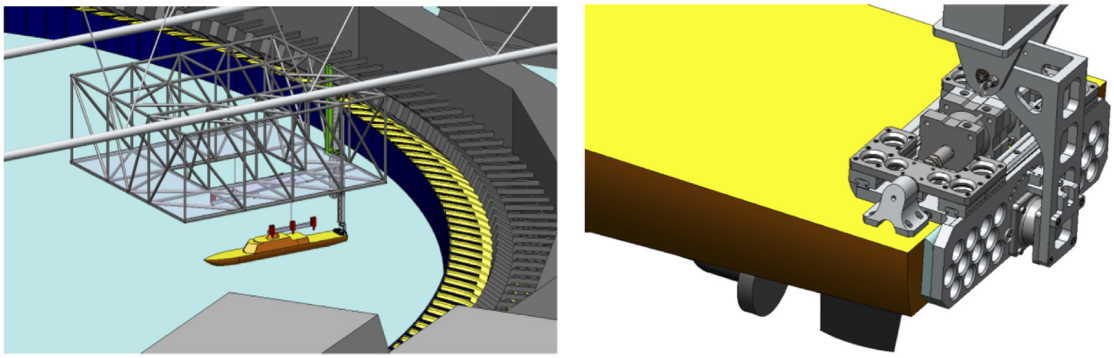

(a) Carriage (b) Mechanism

Figure 4.1: Illustration of a proposed initial condition enforcement mechanism from *Anastopoulos et al.* (2016).

A free-running vessel requires even more consideration when it pertains to the enforcement of encounter conditions. *Knight et al.* (2020) implemented the DLG methodology for a self-propelled ship in head seas that is fixed in sway, roll, and yaw, but free in heave and pitch. Surge is constrained to a constant speed up until the moment the wave group is encountered and then it is released to surge freely. Although the event is experienced in a self-propelled state, there may be some transients from the release that are present in the extreme response. Additionally, a 6-DoF example of this methodology in quartering seas would require surge, sway, and yaw to be constrained until the moment the wave group is encountered. The consequence of releasing all the DoF is unknown and does not produce a realistic wave group encounter.

To address this issue, the natural initial condition method is proposed that embeds the deterministic wave groups produced in the CWG method into an irregular seaway with a known response referred to as the irregular prelude. The composite wave system possesses a consistent set of initial conditions for the fluid and body motion that satisfies the encounter condition at the moment the wave group is encountered for the CWG method, and provides physically realizable wave trains for the CFD simulations.

4.1 Natural Initial Condition

This dissertation proposes a new method for prescribing the encounter conditions by introducing the idea of a *natural* initial condition. Natural initial conditions are achieved by embedding deterministic wave groups into an ensemble of irregular seaways that will naturally produce different encounter conditions as a ship reaches the wave group of interest. This methodology avoids the issues associated with explicitly prescribing initial conditions, and instead allows for the fluid flow and ship responses to develop naturally. Additionally, prescribing the encounter conditions in this manner preserves the integrity of the CWG methodology developed for an ODE, while making the method accessible for higher-fidelity numerical hydrodynamic tools and physical experiments.

Consider a single realization of a free-running vessel starting from rest and traveling through a random seaway that evolves in space and time. Throughout the realization, a specific encounter condition of interest identified for the CWG method occurs at time t_e. The waves experienced by the vessel in the encounter frame can be approximated as the wave elevation function $\eta_{\text{IP}}^{(\text{E})}(t)$, which up until time t_e is referred to as the irregular prelude. The ship speed $U_e = x_e/t_e$, can also be estimated based on the ship traveling a distance of x_e in time t_e. The deterministic wave groups are defined in the earth-fixed frame with Markov Chains as described in Chapter II, which result in a wave group elevation time-history at the origin $(x, y = 0, 0)$:

$$\eta_{\text{WG}}(t) \;=\; \sum_{f} a_{g_f} cos\left(\omega_{g_f} t \;+\; \phi_{g_f}\right) \tag{4.1}$$

where a_{g_f}, ω_{g_f}, and ϕ_{g_f} are the Fourier amplitudes, frequencies, and phases found through trigonometric interpolation of the Markov chain predictions, as well as the wave group constraints detailed in Figure 2.3 that describe the wave group. Figure 4.2 shows the wave elevation at the origin described by the Fourier components for the

wave group, a_{g_f}, ω_{g_f}, and ϕ_{g_f}. The Fourier components only correspond to the wave group. Therefore, the wave group continuously repeats in time.

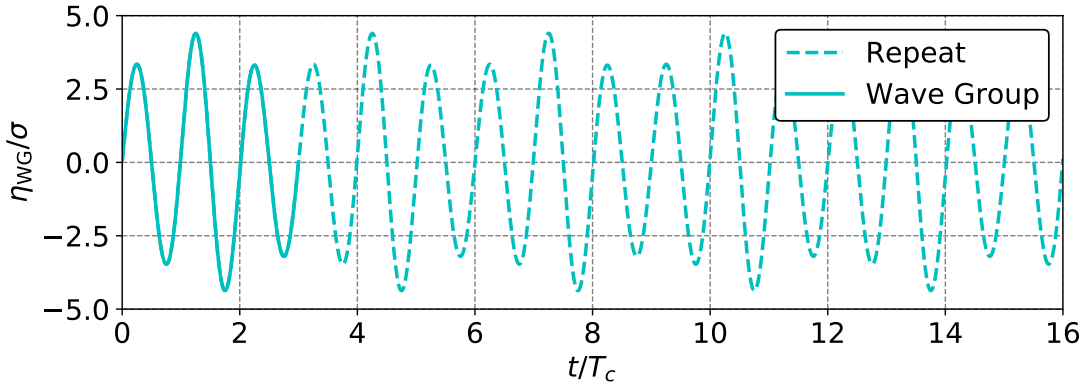

Figure 4.2: Representation of deterministic wave group at origin with Fourier components.

An estimate of encountering the wave group in a constant moving frame can be made by utilizing the deep water dispersion relation for the wavenumber, $k_{g_f} = \omega_{g_f}^2/g$, along with U_e to transform the wave group time-history at a single point into a wave train that repeats in space and time. This modifies Equation 4.1 to describe the wave group in the estimated encounter frame:

$$\eta_{\mathrm{WG}}^{(\mathrm{E})}(t) \;=\; \sum_f a_{g_f} cos\left(\omega_{g_f} t \;-\; k_{g_f}(\cos(\mu) U_e t) \;+\; \phi_{g_f}\right) \tag{4.2}$$

where μ is the wave heading defined such that 180 deg is head seas, 0 deg is following seas, and 90 deg is starboard beam seas. Figure 4.3 shows the encountered wave field as a vessel travels through the origin at $t = 0$ at constant speed and heading. The wave group of interest is encountered over a different time-interval due to the forward speed of the vessel. Like the wave group wave elevation at the origin, the encountered wave group is repeated in time for the Fourier representation.

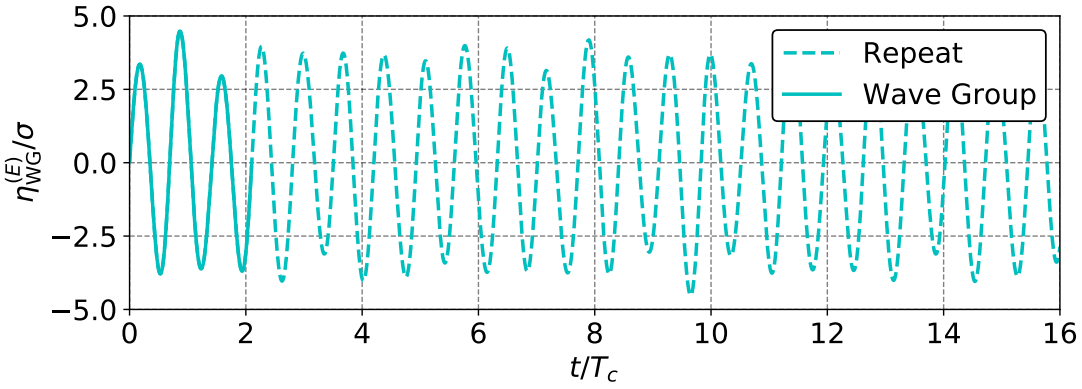

Figure 4.3: Encountered wave elevation traveling through the repeating wave group wave field with constant speed and heading.

To implement the CWG method with CFD, the deterministic wave group in the estimated encounter frame $\eta^{(\mathrm{E})}_{\mathrm{WG}}(t)$ is embedded into the encountered irregular prelude $\eta^{(\mathrm{E})}_{\mathrm{IP}}(t)$. The encountered wave group $\eta^{(\mathrm{E})}_{\mathrm{WG}}$ is shifted by t_e such that the group starts at location x_e, thus ensuring that the encountered wave group $\eta^{(\mathrm{E})}_{\mathrm{WG}}(t)$ will start directly t_e. The new composite seaway in the estimated encounter frame $U_e t$ is formed with the blending functions β_1 and β_2 as:

$$\eta^{(\mathrm{E})}_{\mathrm{C}}(t) = (1-\beta_2)\left[(1-\beta_1)\eta^{(\mathrm{E})}_{\mathrm{IP}}(t) + \beta_1\eta^{(\mathrm{E})}_{\mathrm{WG}}(t-t_e)\right] + \beta_2\eta^{(\mathrm{E})}_{\mathrm{IP}}(t) \tag{4.3}$$

where each blending function is defined as:

$$\beta \;= \frac{1}{2}\left(1+\tanh\left(\frac{t\;-\;t_e}{t_o}\right)\right) \tag{4.4}$$

The functions β_1 and β_2 correspond to the blending at the start and end of the wave group, respectively. Figure 4.4 shows the blending process for embedding the wave group into an irregular wave train to create a single composite wave train. The wave elevation and time in Figure 4.4 are non-dimensionalized by the standard deviation of

the height from the specified wave spectrum σ and the period of the largest wave in the group T_c, respectively.

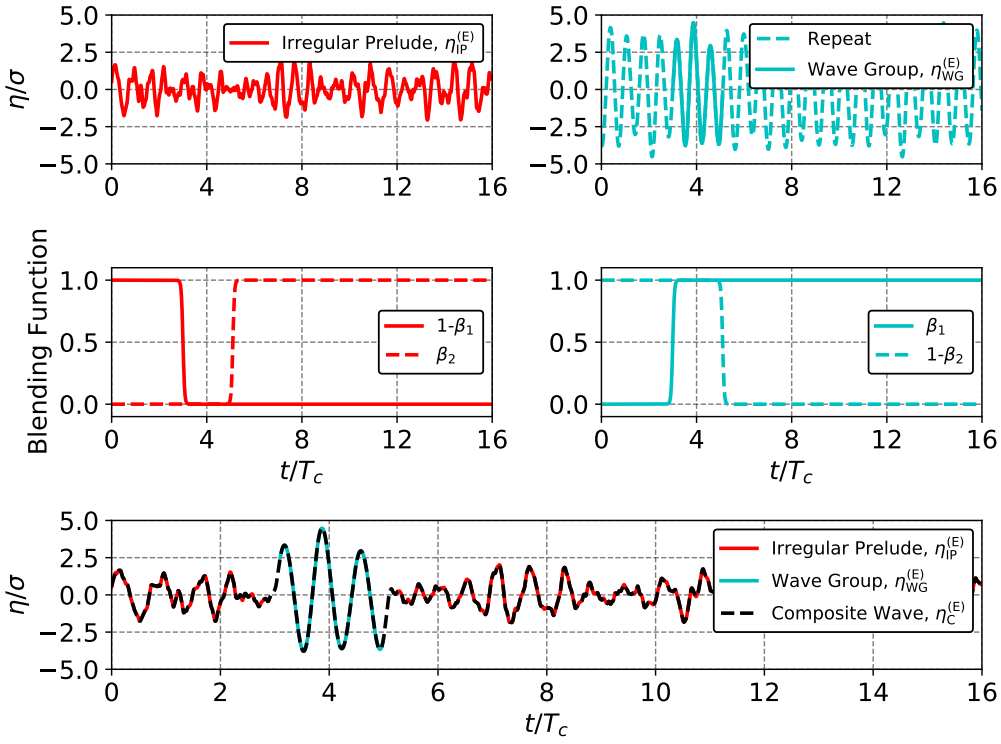

Figure 4.4: Formation of a composite wave by embedding a deterministic wave group into the irregular prelude in the estimated encounter frame.

The two parameters that define the blending function, control the time shift and time scale of the overlap of the two signals: t_e and t_o. The time shift is selected to be $t_e/T_p = 0.1$ from the start or end of the wave group, such that at the start of the wave group t_e, 95 % of the signal is the irregular wave train. Here, T_p is the peak modal period of the selected wave spectrum and is included to provide a time scale for blending that is specific to the wave environment. Therefore, the magnitude of blending is dependent on the specified wave spectrum. The sensitivity to these parameters has not been fully tested, and future research should explore using the period of the largest wave in the embedded wave group instead, as it would enable the blending process to be specific to the actual wave group.

The time scale t_o is selected with Equation 4.5 where the factor of 0.9 corresponds to approximately 95 % of the first signal at the start of the interval and 95 % of the second signal at the end. Equation 4.5 results in a composite wave, where the majority of the blending process occurs within two time intervals of duration $T_p/5$. To form the full composite wave train, t_o is the same for β_1 and β_2, while t_e depends on the start and end of the wave group. The portion of the composite wave train after the wave group is not considered when assessing the extreme ship response, but is required for the wave generation within CFD to ensure that the wave group sequences of interest are not repeated in the observed simulation time.

$$t_o = \frac{T_p}{10 \cdot \tanh^{-1}(0.9)} \tag{4.5}$$

The blending procedure outline in Figure 4.4 produces a description of the composite wave train in the estimated encounter frame $\eta_{\mathrm{C}}^{(\mathrm{E})}(t)$. To generate the necessary waves for CFD, a full spatial and temporal description of the wave field is required. Therefore, $\eta_{\mathrm{C}}^{(\mathrm{E})}(t)$ must be transformed to an earth-fixed frame. In beam to head seas (90-180 deg/180-270 deg), the transformation is straight forward utilizing the relationship $\omega_e = \omega_o - \Psi\omega_o^2$, where $\Psi = \cos(\mu)U_e/g$. With the conversion of the frequencies to the absolute frame and calculation of the wavenumber through the dispersion relation, the resulting composite wave train $\eta_{\mathrm{C}}^{(\mathrm{E})}(\mathbf{x}, t)$ is a function of both space and time, as is required by CFD. However, in beam to following seas (0-90 deg, 270-360 deg), the Doppler effect causes the transformation to be multi-valued due to do the movement of ship relative to the direction of the waves. Figure 4.5 illustrates the 3-to-1 mapping problem, where under the right conditions, an encounter frequency ω_e can correspond to three separate absolute frequencies ω_o. *Nielsen* (2017) introduced an algorithm to address this issue. In cases where this multi-valued problem exists, the encounter

frequency can be mapped to the three separate absolute frequencies. A scale factor is then applied to the original corresponding amplitude Fourier components, based on a nominal wave spectrum estimated from the Fourier components in the encounter frame. This dissertation includes a case study for a 3-D free-running ship in stern-quartering seas and implements the *Nielsen* (2017) methodology to address this 3-to-1 mapping problem.

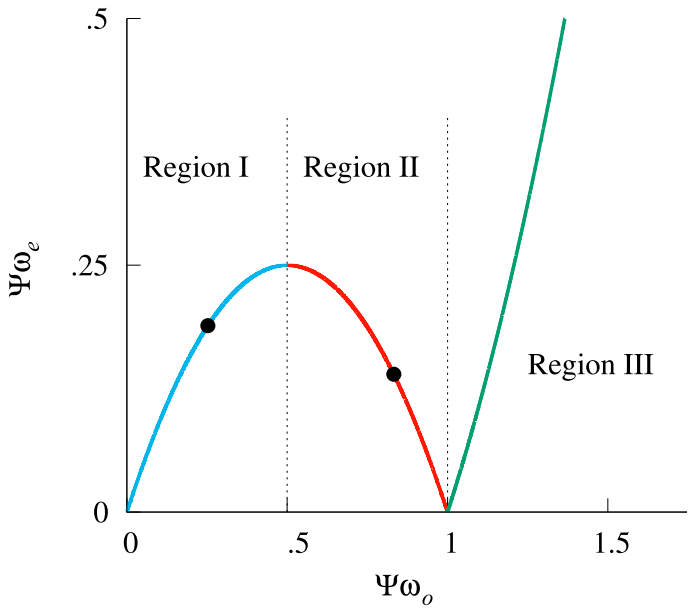

Figure 4.5: Relationship between encounter (ω_e) and absolute (ω_o) frequencies (*Xu et al.*, 2020)

The natural initial condition method allows for enforcement of the encounter conditions of interest and generation of the wave group in a natural manner without intrusive and nonphysical measures or mechanisms (physical or virtual). All of the necessary information needed for the CFD is contained within the composite wave train. Figure 4.6 reflects an ensemble of composite waves that possess the same wave group with different irregular preludes. The time-histories in Figure 4.6 have been shifted such that the peak of the largest wave in the group occurs at the same time for the composite wave trains to illustrate the methodology. All of the irregular preludes must account for the ramping up of the wave generation and the vessel reaching it's

target speed. This logic ensures that the vessel will reproduce the previously simulated results that led to the encounter condition.

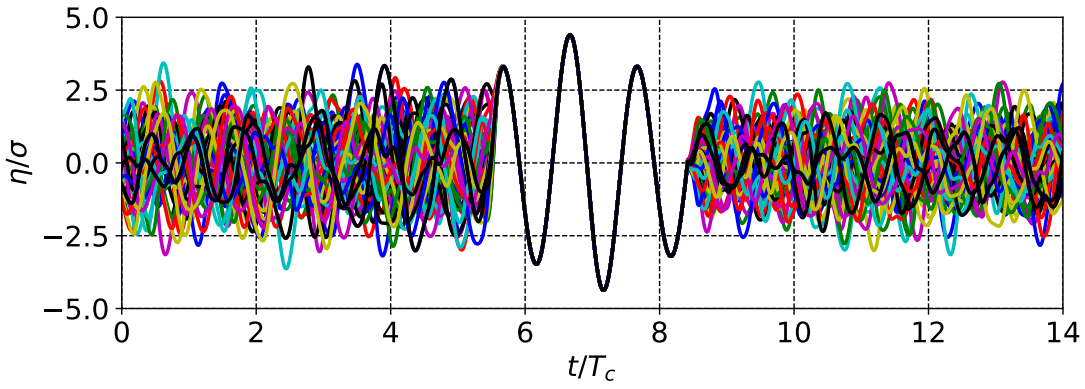

Figure 4.6: Ensemble of various waves with corresponding different irregular preludes for the same wave group that is shifted in time such that the largest wave in the group's peak occurs at the same time.

An added benefit of the natural initial condition method is that a separate set of irregular wave trains that satisfy the same encounter condition can be determined. This identification allows for the construction of an ensemble of composite wave trains that can be studied to further understand sensitivity to encounter conditions. For instance, if only roll and roll velocity are considered for the encounter condition, but sway velocity contributes significantly, then irregular preludes with different sway velocities can be found to assess the importance of sway. Conversely, if unfavorable encounter conditions are selected such as heave motion and surge velocity when considering large roll, recognition of unsuitable quantities would be simple. Significant differences would occur in the ship response for the same encounter condition and wave group. This aspect of the natural initial condition methodology yields greater utility with more complicated failure mechanisms like capsizing due to broaching-to, where the quantities considered for the encounter conditions are not evident.

CHAPTER V

System Identification with LSTM Neural Networks

This dissertation is focused on both the probabilistic quantification and observation of extreme ship response events. To reduce the computational cost of implementing the CWG method with CFD, a prediction-focused surrogate modeling technique is required in order to retain the temporal response of a vessel, allowing for insight into the mechanisms behind a particular response. This chapter details the SI modeling methodology developed to reproduce the 6-DoF response of a free-running vessel in large amplitude waves with LSTM neural networks.

The overall objective of an SI technique is to develop a model that, given an input, can produce an output that is representative of the underlying system of interest. In the case of a causal dynamical system *e.g.* ship responses in waves), the output is not only dependent on the external forcing at the current time step, but it also depends on the history of both the external forcing as well as the state of system. The output of a discrete dynamical system y_t at any time index t can be described by:

$$y_t = f(x_t, x_{t-1}, x_{t-2}, \cdots) \tag{5.1}$$

where f is a mapping function and x_t corresponds to the input at time index t. Equation 5.1 shows that the output state y_t not only depends on the current input x_t, but also the previous values $(x_{t-1}, x_{t-2}, ...)$. The overall goal of any surrogate modeling

technique is to develop the best nonlinear mapping f that describes the system.

5.1 Neural Networks

The developed methodology leverages LSTM neural networks (*Hochreiter and Schmidhuber*, 1997), which are an implementation of RNN that attempt to solve the vanishing gradient problem. The vanishing gradient problem is a consequence of gradient values in the optimization scheme becoming too small during training, and can result in the training completely stopping. LSTM neural networks address this issue through the implementation of different gates that regulate how much information is transferred between time-steps and how weights are optimized. Figure 5.1 demonstrates a single LSTM cell and demonstrates how a cell input x_t is translated into the cell output h_t through the mathematical operations outlined in Equations 5.2 through 5.7, where $\sigma(\cdot)$ is the sigmoid function and $*$ is the elementwise multiplication, while W_f, b_f, W_i, b_i, W_C, b_C, W_o, and b_o are the LSTM parameters to learn from the data.

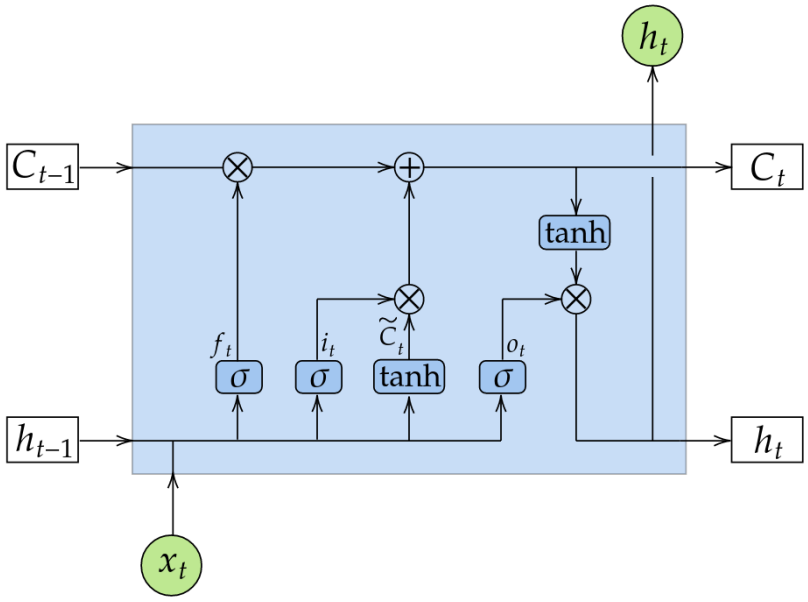

Figure 5.1: Diagram of an LSTM cell.

$$f_t = \sigma(W_f \underbrace{[h_{t-1}, x_t]}_{\text{concatenate}} + b_f) \tag{5.2}$$

$$i_t = \sigma(W_i \underbrace{[h_{t-1}, x_t]}_{\text{concatenate}} + b_i) \tag{5.3}$$

$$\tilde{C}_t = \tanh(W_C \underbrace{[h_{t-1}, x_t]}_{\text{concatenate}} + b_C) \tag{5.4}$$

$$C_t = f_t * C_{t-1} + i_t * \tilde{C}_t \tag{5.5}$$

$$o_t = \sigma(W_o \underbrace{[h_{t-1}, x_t]}_{\text{concatenate}} + b_o) \tag{5.6}$$

$$h_t = o_t * \tanh(C_t) \tag{5.7}$$

The singular LSTM cell in Figure 5.1 can extend to multiple cells and layers to build a *deep* neural network. Figure 5.2 displays an example neural network architecture with five LSTM layers, followed by a dense layer. Inputs and outputs are denoted as x_t and y_t, respectively, where t is the time step index that ranges from 1 to T. C_t^n and h_t^n correspond to state and output of LSTM cell n at time index t. h_t^n is the output of the cell but it (along with C_t) are also shared with neighboring cells. The stacking of LSTM layers allows for the output of the previous layers to be used as the input for the next layer. Generally, adding layers to the neural network model architecture creates a greater level of abstraction within the trained model, which helps establish generalized predictions of input scenarios that are not considered during the model training. The dense layer in Figure 5.2 employs a linear activation function and receives the last of the LSTM layers as input, and outputs the final result of the neural network model.

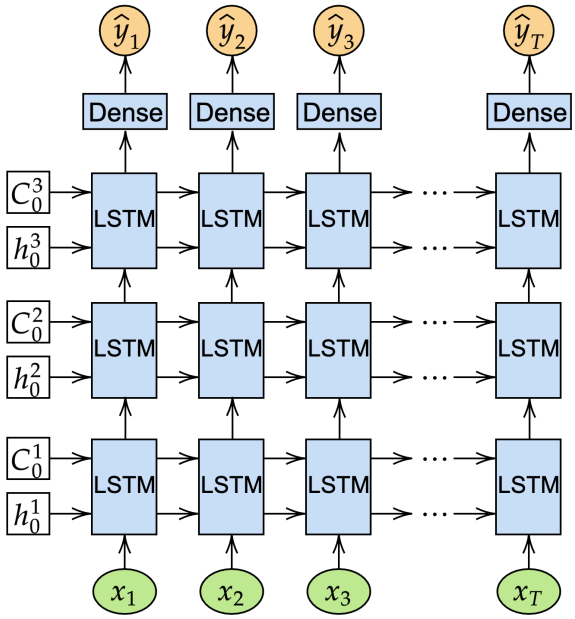

Figure 5.2: Diagram of the neural network architecture.

Machine learning and neural networks in particular have gained a tremendous amount of popularity in recent years and are being implemented across many disciplines in both academia and industry. Although much focus has been placed on development of the most accurate models to describe a dataset, knowing when the models are not applicable can be just as or even more important. Therefore, the quantification of uncertainty in neural network predictions is a necessity in any of their applications. This dissertation considers the Monte Carlo Dropout approach developed by *Gal and Ghahramani* (2016a,b) to quantify uncertainty. Dropout is a common regularization technique employed in training neural networks, where a portion of the neurons are randomly excluded from activation and weight updates while training the model. This technique, demonstrated in Figure 5.3, helps to prevent the model from over-fitting, as well as propels the optimization scheme toward a more generalized model capable of producing accurate predictions outside of the training dataset.

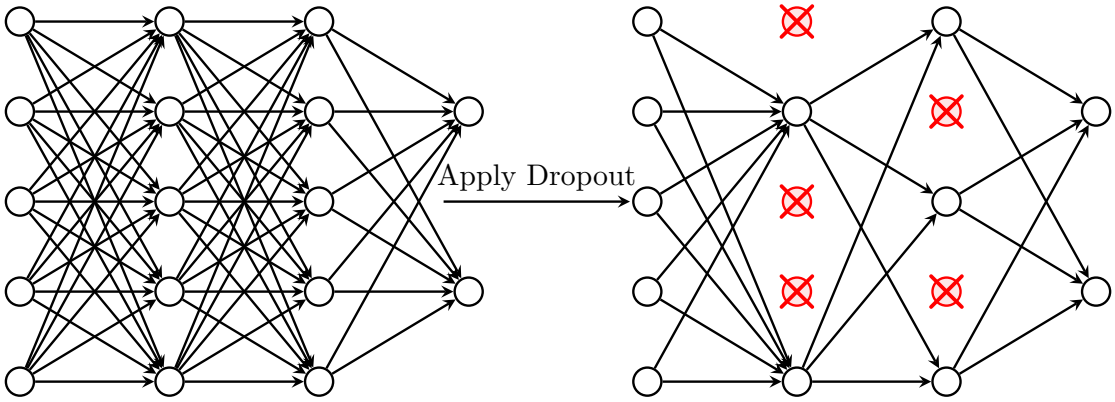

Figure 5.3: Application of dropout regularization technique.

Gal and Ghahramani (2016a,b) proposed the Monte Carlo dropout approach, where dropout is also performed during prediction, thus providing an ensemble of predictions. This ensemble of predictions can then be used to provide uncertainty estimates. In the context of this dissertation, a dropout layer is added after each LSTM layer to implement the Monte Carlo dropout methodology. This type of uncertainty estimate is extremely useful, as it does not require any intrusive modification to the neural network architecture, other than adding the dropout layers. Previous research with the Monte Carlo dropout method has demonstrated its effectiveness in providing larger uncertainty estimates when a model performs a prediction that is outside of the training dataset. Figure 5.4 shows an example with the Monte Carlo dropout approach for uncertainty. The observed function in red resides to the left of the dashed line, while the predictive mean is in black and an uncertainty of plus and minus two standard deviations is reflected in blue, where each shade represents half of a standard deviation. With the Monte Carlo dropout approach, the model is able to denote an area of large uncertainty outside of what was previously observed, indicating a region where a lower accuracy prediction is more probable. The ability to produce larger uncertainty estimates for cases where the model is more likely to perform poorly is desirable in its application to extreme, events as the model uncertainty can propagate

through the probability calculations to provide uncertainty estimates on the relevant statistics to inform decisions.

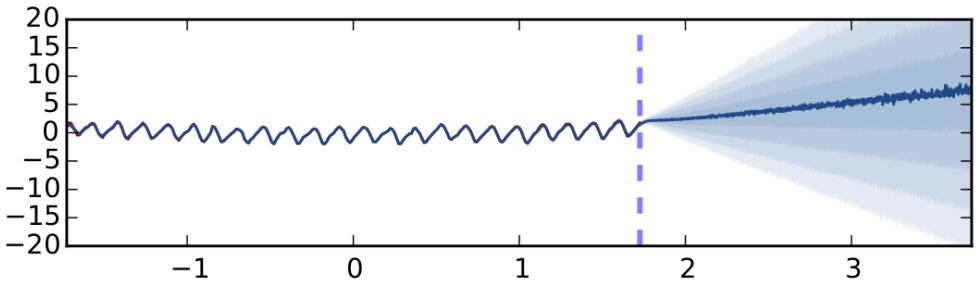

Figure 5.4: Demonstration of Monte Carlo dropout from *Gal and Ghahramani* (2016a).

5.2 Framework

The majority of the previous research modeling ship responses with neural networks has typically focused on simpler application such as a 2-D midship sections (*Xu et al.*, 2021), constant speed and heading (*del Águila Ferrandis et al.*, 2021), or extremely short time windows (*D'Agostino et al.*, 2022). *Xu et al.* (2021), which drew inspiration from *Xu* (2020), was able to represent the heave and roll of a 2-D midship section that was constrained in surge, sway, and yaw by developing a relationship between the wave elevation at the inlet of the URANS computational domain and the motions of the hull. However, a methodology capable of predicting the response of a free-running vessel must account for the ship moving in space, and static wave probes are not sufficient as input into the neural network. Not only must the model learn the resulting ship motions, but it also must be trained to understand the wave propagation from a static wave probe to a moving vessel with unknown trajectory.

The primary concept driving the present methodology is that a vessel experiences wave excitation in the encounter frame-of-reference. Therefore, instantaneous wave elevation around the hull should serve as the input into the model. However, the trajectory of the vessel and thus the instantaneous encounter frame, is not known

a priori and must be estimated. The following procedure describes the proposed modeling approach and training process:

1. Select K wave probe locations in the initial earth-fixed coordinate frame.
2. Estimate the encounter frame with the surge, sway, and yaw motions from the training data.
3. Find the instantaneous wave elevation at each wave probe moving with the estimated encounter frame.
4. Standardize the datasets for each respective wave probe and ship motion DoF.
5. Train the model to develop a relationship between the wave elevation time histories of the moving wave probes, and the 6-DoF motions of the vessel.

The first step in the training procedure is to select K wave probe locations in the initial coordinate frame around the hull. The probe locations should be somewhat close to the hull (*e.g.* within one wavelength corresponding to the peak modal period of the waves). Then, the encounter frame is estimated from the surge, sway, and yaw motions in the training dataset. Figure 5.5 demonstrates an example of estimated encounter frames developed with a series of training data trajectories from course-keeping and turning circle simulations. The encounter frame is estimated by averaging the position of the vessel at every time step, thus accounting for an arbitrary maneuver. The encounter frame can also be estimated for course-keeping, with the nominal speed and heading, but would not include any appreciable drift or speed gain/loss that may be more evident in large amplitude waves.

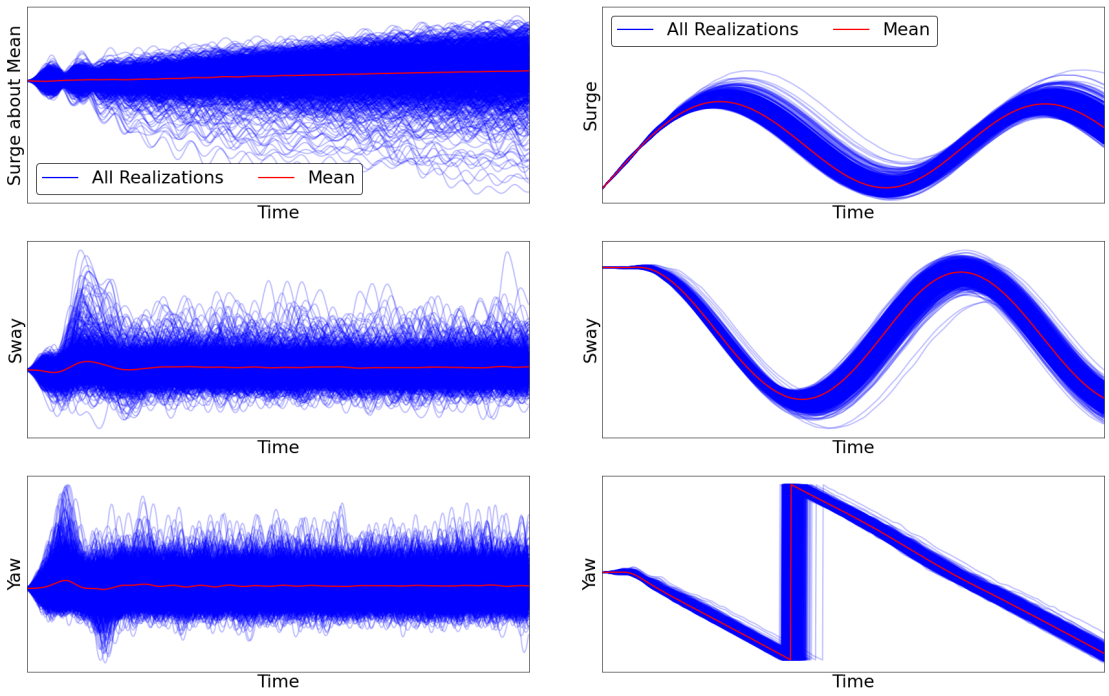

(a) Course-keeping (b) Turning Circle

Figure 5.5: Estimation of encounter frame based on training data.

With an estimate of the encounter frame through the mean trajectories observed in the training data, and a wave definition in the earth-fixed frame, the instantaneous wave elevation time-histories for a set of K wave probes that move with the estimated encounter frame can be characterized. Given a wave probe k, the instantaneous estimated encounter wave elevation $\eta_k(\mathbf{x}_k, t)$ can be described by:

$$\eta_k(\mathbf{x}_k, t) = \sum_f a_f cos(\omega_f t - \mathbf{k}_f \cdot (\mathbf{x}_E(t) + \mathbf{R}_E(t)\mathbf{x}_k) + \phi_f) \tag{5.8}$$

where a_f, ω_f, and ϕ_f correspond to the amplitude, frequency, and phase of the F wave Fourier components, $\mathbf{k}_f$ is a vector describing the wavenumber and direction of each component, $\mathbf{x}_E(t)$ is the coordinate location of the estimated encounter frame with respect to time t, $\mathbf{x}_k$ is the coordinate location of probe k in the initial earth-fixed

frame, and $\mathbf{R}_E(t)$ is a rotation matrix of the mean yaw trajectory described by:

$$\mathbf{R}_E(t) = \begin{bmatrix} \cos\psi_E(t) & -\sin\psi_E(t) \\ \sin\psi_E(t) & \cos\psi_E(t) \end{bmatrix} \tag{5.9}$$

Equation 5.8 provides a wave elevation time-history of T time steps for probe k that travels with the estimated encounter frame. Additionally, the wave elevation in the encounter frame is known for K wave probes around the ship. Thus, for M different training cases, a 3-D input matrix can be defined as:

$$\mathbf{X} = \begin{bmatrix} \mathbf{x_{11}} & \mathbf{x_{12}} & \cdots & \mathbf{x_{1T}} \\ \mathbf{x_{21}} & \mathbf{x_{22}} & \cdots & \mathbf{x_{2T}} \\ \vdots & \vdots & \vdots & \vdots \\ \mathbf{x_{M1}} & \mathbf{x_{M2}} & \cdots & \mathbf{x_{MT}} \end{bmatrix} \tag{5.10}$$

where each entry, $\mathbf{x_{mt}} = \left[x_{mt}^{(1)},\ x_{mt}^{(2)},\ ...,\ x_{mt}^{(K)}\right]$, corresponds to all of the wave elevation values for the K probes. The output matrix is described by:

$$\mathbf{y} = \begin{bmatrix} \mathbf{y_{11}} & \mathbf{y_{12}} & \cdots & \mathbf{y_{1T}} \\ \mathbf{y_{21}} & \mathbf{y_{22}} & \cdots & \mathbf{y_{2T}} \\ \vdots & \vdots & \vdots & \vdots \\ \mathbf{y_{M1}} & \mathbf{y_{M2}} & \cdots & \mathbf{y_{MT}} \end{bmatrix} \tag{5.11}$$

where each entry, $\mathbf{y_{mt}} = \left[y_{mt}^{(1)},\ y_{mt}^{(2)},\ ...,\ y_{mt}^{(6)}\right]$, corresponds to the surge and sway velocity, heave, roll, pitch, and yaw response of the vessel. The surge and sway velocities are included since their values in time typically oscillate about a more stationary mean.

Once the input and output training matrices are constructed, both are standardized with respect to each input feature (*i.e.* individual wave probe) and output label (*i.e.*

a single motion DoF). The standardization results in each feature and label entering the training phase with zero mean and a standard deviation of one. After the data has been standardized, the training process begins where the various parameters in the neural network are continuously updated through several iterations within an optimization scheme that aims to minimize the loss function shown in Equation 5.12, where $\hat{y}$ is the prediction of the model, y is the true output label, and N is the number of elements in the output matrix y reflected in Equation 5.11, which corresponds to $N = 6MT$.

$$L(\hat{y}, y) = \frac{1}{T}\sum_{t=1}^{N}(\hat{y}_n - y_n)^2 \tag{5.12}$$

The current implementation develops a neural network for a single vessel and loading condition. The neural network does not contain any explicit information about the hull geometry or mass properties, and is not a generally applicable independent hydrodynamic model. The modeling methodology requires training in the form of external data from either simulations, model tests, or full-scale trials, in order to build the relationship between the wave environment and the associated dynamical response of the vessel. The model architecture in this dissertation is implemented with the toolbox Keras (*Chollet et al.*, 2015) with TensorFlow (*Abadi et al.*, 2015) as its backend.

5.3 Case Study: 3-D 6-DoF 5415

The proposed surrogate modeling methodology for representing 6-DoF ship responses with an LSTM neural network is demonstrated with simulations performed with LAMP for the David Taylor Model Basin (DTMB) 5415 hull form shown in Figure 5.6 for both course-keeping and turning circles. This case study is largely based on the case study from *Silva and Maki* (2022a) and is included here for completeness.

LAMP is a potential flow time-domain ship motion and wave loads simulation tool. LAMP invokes a time-stepping scheme where all forces and moments acting upon the ship (*e.g.* wave-body interaction, appendages, control systems, green-water-on-deck, etc.) are evaluated at each time step and the 6-DoF equations of motion are integrated in time to advance the solution. At the center of the LAMP calculation scheme is the solution of the 3-D wave-body interaction problem (*Lin and Yue*, 1990; *Lin et al.*, 1994). A 3-D perturbation velocity potential is computed by solving an initial boundary value problem with a potential flow BEM. Subsequently, Bernoulli's equation is used to compute the hull pressure distribution, including the second-order terms. The current case study employed the LAMP-3 approach, where the perturbation velocity potential is solved over the mean wetted surface (body-linear), while the nonlinear Froude-Krylov and hydrostatic restoring forces are solved over the instantaneously wetted area of the hull below the incident wave (body-nonlinear). This blended nonlinear methodology captures the significant portion of nonlinear effects in most ship-wave problems at a fraction of the computational effort required for the general body-nonlinear formulation. LAMP-3 also allows for large lateral motions and generalized 6-DoF motions. LAMP is considered in this case study as a proving ground for the 6-DoF methodology before its application to high-fidelity CFD. Although LAMP does not provide as quantitative of a prediction as CFD, some of the main sources of nonlinearity, such as the hydrostatic restoring and Froude-Krylov forces, are included. Performance of the surrogate modeling methodology with LAMP provides insight into its applicability to CFD and physical experiments.

Table 5.1 shows the loading condition and fluid properties for the DTMB 5415 case study. The loading condition is derived from CFD validation studies performed for the 5415M in *Sadat-Hosseini et al.* (2015), while the fluid properties represent seawater at 20 °C (*ITTC*, 2011).

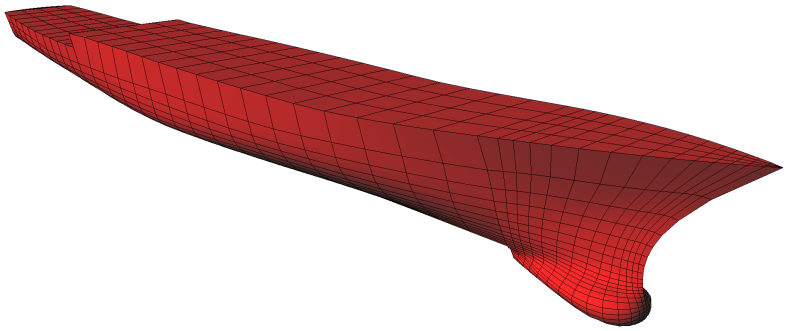

Figure 5.6: LAMP representation of the DTMB 5415 hull form.

Table 5.1: Loading condition of DTMB 5415 hull and fluid properties.

Properties	Units	Value
Length Between Perpendiculars, L_{pp}	m	142.0
Beam, B	m	19.06
Draft, T	m	6.15
Displacement, ∇	tonnes	8431.8
Longitudinal Center of Gravity, LCG (+Fwd of AP)	m	70.317
Vertical Center of Gravity, KG (ABL)	m	7.51
Transverse Metacentric Height, GMT	m	1.95
Roll Gyradius, k_{xx}	m	7.62
Pitch Gyradius, k_{yy}	m	35.50
Yaw Gyradius, k_{zz}	m	35.50
Density of Water, ρ_w	kg/m^3	1024.81
Kinematic Viscosity of Water, ν_w	m^2/s	1.0508e-06
Acceleration due to Gravity, g	m/s^2	9.80665

Table 5.2 demonstrates a summary of the operating and seaway conditions considered for the case study, as well as other details of the simulation dataset. The DTMB 5415 hull is set to operate at 20 knots in Sea State 7, stern-quartering long-crested seas described by the Bretschneider spectrum (*Bretschneider*, 1959). The significant wave height H_s, corresponds to the middle of the Sea State 7 band, while the peak modal period T_p, is the most probable modal period for Sea State 7 in the North Atlantic (*Bales*, 1983). All of the simulations are performed in random irregular seaways with 250 Fourier components. Although rare and extreme wave events are not expected to

occur regularly throughout the dataset produced in this case study, the data provides a means of testing the surrogate modeling methodology as well as the effectiveness of the estimated encounter frame.

Table 5.2: Operating and seaway conditions for the DTMB 5415 case study.

Properties	Units	Value
Speed	knots	20
Wave Heading	deg	45 (Stern Quartering)
Sea State	-	7
Spectrum	-	Bretschneider
Significant Wave Height, H_s	m	7.5
Peak Modal Period, T_p	s	15
Fourier Components	-	250
Proportional Gain, G_p	deg/deg	4
Integral Gain, G_i	1/s	0
Differential Gain, G_d	deg/(deg/s)	1
Max Rudder Rate, $\dot{\delta}_{\max}$	deg/s	9
Max Rudder Deflection, $\delta_{\max}$	deg	35
Rudder Deflection (Turning Circle), δ_{turn}	deg	35

The DTMB 5415 hull is free to surge, sway, heave, roll, pitch and yaw in the simulations. The LAMP simulations utilize a quasi-steady propeller performance model from *Lee et al.* (2003) for both the course-keeping and turning circle cases. Course-keeping is maintained with two rudders modeled as low aspect ratio foils operated by the PID-controller in Equation 3.30. For course-keeping, the commanded rudder deflection δ_c is calculated with the proportional G_p, integral G_i, and derivative G_d gains as well as the desired heading ψ_d and the current heading ψ. All the gains for the course-keeping case study are tabulated in Table 5.2. The turning circle cases maintained a 35 deg rudder deflection during the entire simulation.

Various neural network architectures are examined and the final selection is determined from a grid-search of different values of the cells per LSTM layer, number of LSTM layers, and the dropout value. Each neural network is trained with the 27 probes and 640 training runs, and the accuracy is evaluated with the loss function

calculation for the validation dataset. Table 5.3 demonstrates a comparison of all the considered neural network architectures and the corresponding loss function in Equation 5.12 for the validation dataset described in Table 5.4. The dropout quantity refers to the percentage of the network that is randomly excluded during training. Overall, the architecture with 250 cells per LSTM layer, 3 LSTM layers, and dropout of 10% provided the most accurate predictions and is utilized in building all of the models in this dissertation for free-running vessels.

Table 5.3: Comparison of loss function for validation data using different neural network architectures for the 27 probe and 640 training runs course-keeping DTMB 5415 case study.

Cells per Layer	Dropout	2 Layers	3 Layers
50	10%	0.1231	0.1195
50	20%	0.1405	0.1374
100	10%	0.0972	0.0817
100	20%	0.1057	0.1000
150	10%	0.0768	0.0525
150	20%	0.0844	0.0727
200	10%	0.0484	0.0434
200	20%	0.0576	0.0539
250	10%	0.0433	0.0359
250	20%	0.0512	0.0446
300	10%	0.0407	0.0361
300	20%	0.0518	0.0396
350	10%	0.0363	0.0360
350	20%	0.0435	0.0381

The complete training dataset consists of 640 simulations, each 360 s in length, for a total exposure window of 64 hours. Several models are constructed in the case study and vary in the quantity of data in the training, but they all draw from the same collection of 640 simulations. For example, 10 run models utilize training data that is a subset of the 20 run models, the 20 run models consider training data that is a subset of the 40 run models, and so on. Additionally, all the models were evaluated with the same validation dataset that is independent of the training dataset and contained

1000 simulations, corresponding to 100 hours of total exposure time. To evaluate the efficacy of the proposed LSTM neural network model building methodology, understanding the behavior and convergence is imperative for models trained with different quantities of data and the fidelity of the wave field description. Table 5.4 reflects the different neural network parameters utilized in the training of the models. The course-keeping and turning circle case studies in Sections 5.3.1 and 5.3.2 employ completely different datasets, but each of the case studies consider the same neural network architecture and total quantity of simulations for the respective training and evaluations shown in Table 5.4. The number of training runs for each case study varies from 10 to 640, while the number of wave probes for the input ranged from 1 to 27, for a total of 28 unique models. The same neural network architecture, hyper-parameters, and training approach are implemented for each of the constructed models. The hyper-parameters refer to the the quantities (e.g. learning rate, epochs) that guide the optimization algorithm when training the model.

Table 5.4: Training matrix, neural network architecture, and hyper-parameters for the DTMB 5415 course-keeping and turning circle case studies.

Properties	Units	Value
Total Training Runs	-	10, 20, 40, 80, 160, 320, 640
Total Validation Runs	-	1000
Total Wave Probes	-	1, 3, 9, 27
Time Steps per Run	-	720
Individual Run Length	s	360
Units per Layer	-	250
Layers	-	3
Dropout	-	0.1
Learning Rate	-	0.00001
Epochs	-	2000
Optimizer	-	Adam (*Kingma and Ba*, 2014)

The probe locations considered for the case study are shown in Figure 5.7, where λ_p is a nominal wavelength, calculated based on T_p. When only one probe is considered,

that wave probe is located at the center of gravity (CG). Models built with more than one wave probe share the same extents based on λ_p, but the spacing between probes $\Delta\lambda_p$ is described by:

$$\Delta\lambda_p = \frac{\lambda_p}{K-1} \quad \text{for} \quad K = 3,\ 9,\ 27 \tag{5.13}$$

In this dissertation, wave probe locations varied either longitudinally along the ship centerline for the 3-D case studies in Chapter VIII and V or aligned with the wave direction for the 2-D case study in Chapter VII. For the 3-D cases, no improvement in model accuracy is observed when probes are placed away from the ship centerline. This may be specific to the current case and future research is required in order to investigate the influence of lateral wave probe locations.

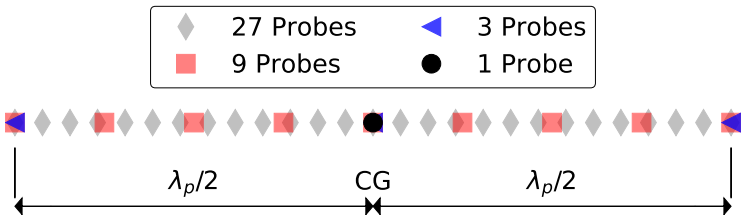

Figure 5.7: Probe locations relative to the ship's CG.

5.3.1 Course-keeping in Random Irregular Waves

A series of models are constructed to evaluate their accuracy and convergence with respect to the quantity of input wave probes and training data for course-keeping LAMP simulations. The accuracy of the different models are evaluated with the L_2 and L_∞ error between the LAMP simulations y and neural network predictions $\hat{y}$. The L_2 error in Equation 5.14 is a measure of the Root Mean Square Error (RMSE), which is the same as the loss function, across a particular time series with time indices ranging from i to T. The L_∞ error in Equation 5.15 quantifies the largest error observed in a given time series.

$$L_2(y, \hat{y}) = \sqrt{\frac{1}{T}\sum_{i=1}^{T}(y_i - \hat{y}_i)^2} \tag{5.14}$$

$$L_\infty(y, \hat{y}) = \max_{i=1,\cdots,T} |y_i - \hat{y}_i| \tag{5.15}$$

Figures 5.8 and 5.9 show comparisons of the L_2 and L_∞ error for each DoF of each neural network model trained with various quantities of training data and wave probes as input into the models. Each marker denotes the median error for all of the validation runs, while the upper and lower error bars correspond to the 75% and 25% quantiles, respectively. The data trends toward smaller error, as both the wave probe and training data quantities are increased. As the median error decreases, so does the spread of the total error denoted by the error bars. Although the error is decreased by increasing the number of wave probes from 9 to 27, the difference is much smaller in comparison to the coarser wave descriptions with 1 and 3 probes. Additionally, although the difference between models decreases as number of training runs increases from 320 to 640, the overall trends of the models indicate that the predictions continue to improve as the training data quantity increases. This convergence provides confidence in the modeling approach and indicates that when applied to extreme events, the continual addition of more data will provide an increase in accuracy.

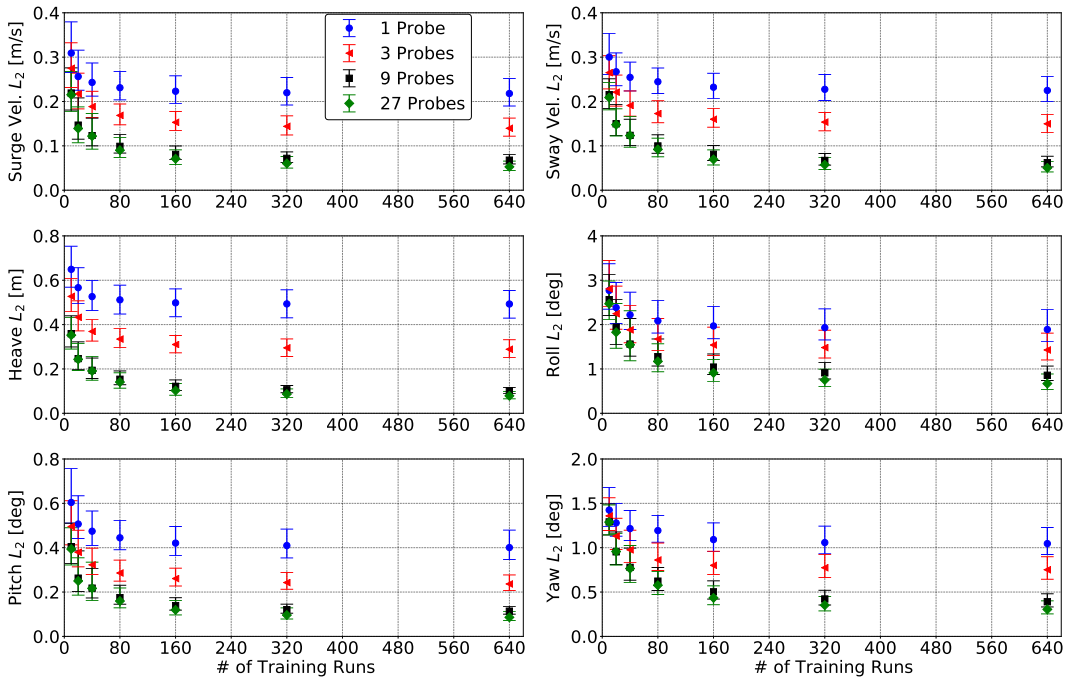

Figure 5.8: Comparison of L_2 error for each DoF in the course-keeping DTMB 5415 case study.

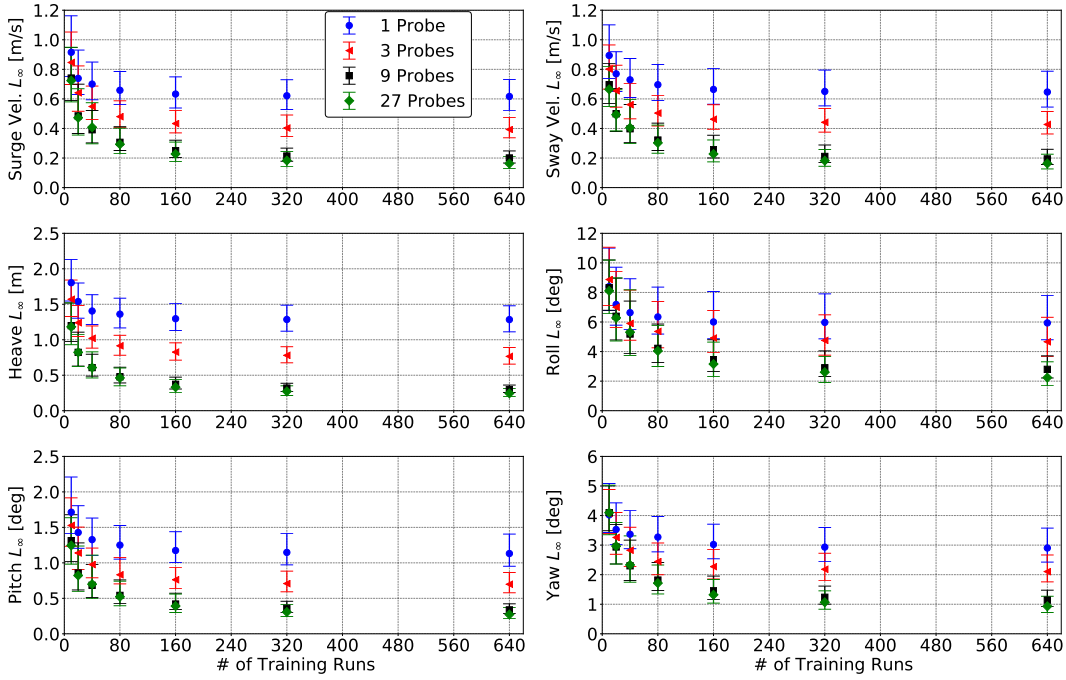

Figure 5.9: Comparison of L_∞ error for each DoF in the course-keeping DTMB 5415 case study.

Figures 5.8 and 5.9 demonstrate an increase in accuracy as the quantity of wave probes and training data is increased, resulting in the most accurate model being built with 27 wave probes and 640 training data runs. Though the comparison of L_2 and L_∞ provides an overall assessment of the models, one benefit of considering a prediction-focused surrogate modeling technique is the ability to produce an accurate temporal response. Figures 5.10 and 5.11 show comparisons between LAMP and the neural network model built with 27 wave probes and 640 training data runs for the three validation runs with the smallest L_2 and L_∞ error for each DoF. The LSTM prediction, denoted by a red dashed line, is the mean of the stochastic predictions made by the Monte Carlo dropout approach, while the uncertainty U_{LSTM}, highlighted in red, is calculated to be $\pm 5\sigma$ based on the Monte Carlo dropout realizations. $\pm 5\sigma$ is chosen for the uncertainty interval, as the overall uncertainty in the developed models is low and increasing the interval size allowed the larger uncertainty regions to be observed visually. Overall, for the cases with the lowest L_2 and L_∞ error, the LSTM model predicts the 6-DoF response well and the uncertainty U_{LSTM}, predicted with the Monte Carlo dropout approach, is small.

Figures 5.12 and 5.13 illustrate the comparisons between LAMP and the LSTM model built with 27 wave probes and 640 training data runs for the three validation cases with the largest L_2 and L_∞ error for each DoF. The magnitude of the responses is much greater in Figures 5.12 and 5.13 than in Figures 5.10 and 5.11, thus the model is capable of providing better predictions for cases with an overall smaller response. In contrast with Figures 5.10 and 5.11, the uncertainty is larger in Figures 5.12 and 5.13, especially for the DoF and sequences where the LSTM prediction is poor, such as the roll and yaw motions between 40-120 s. Although the predictions are not as accurate as what is shown in Figures 5.10 and 5.11, the amplitude and phase of the LSTM and LAMP predictions are similar, and the uncertainty estimates are larger in areas where the model accuracy is lower.

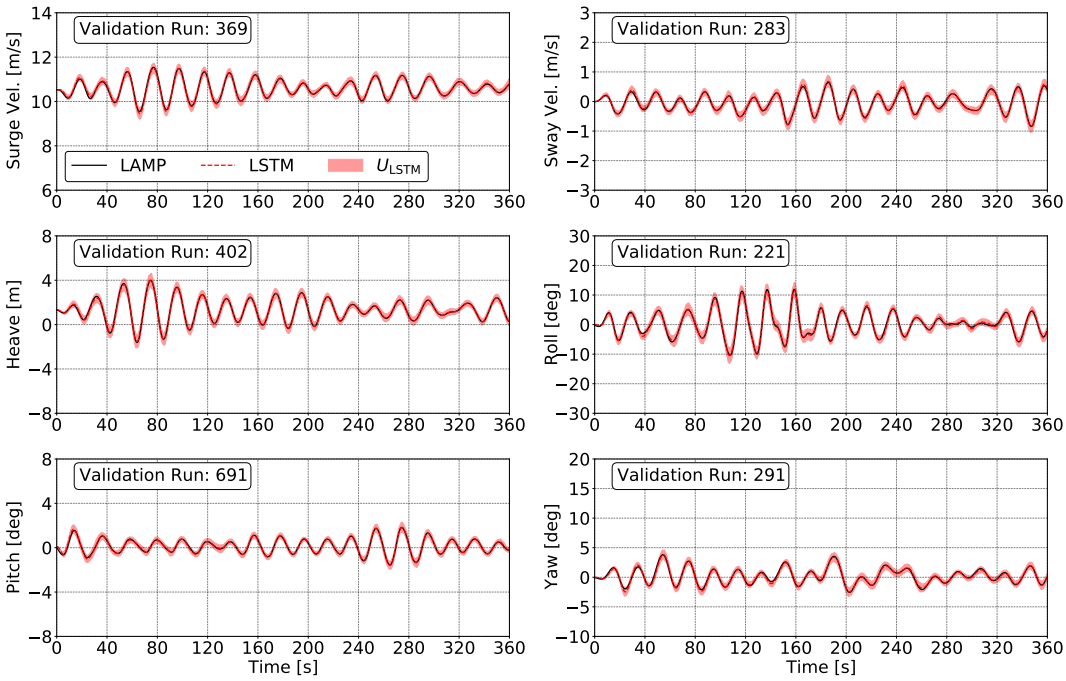

Figure 5.10: Best (ranked by L_2 error) motion predictions for a model with 27 probes and 640 training runs in the course-keeping DTMB 5415 case study.

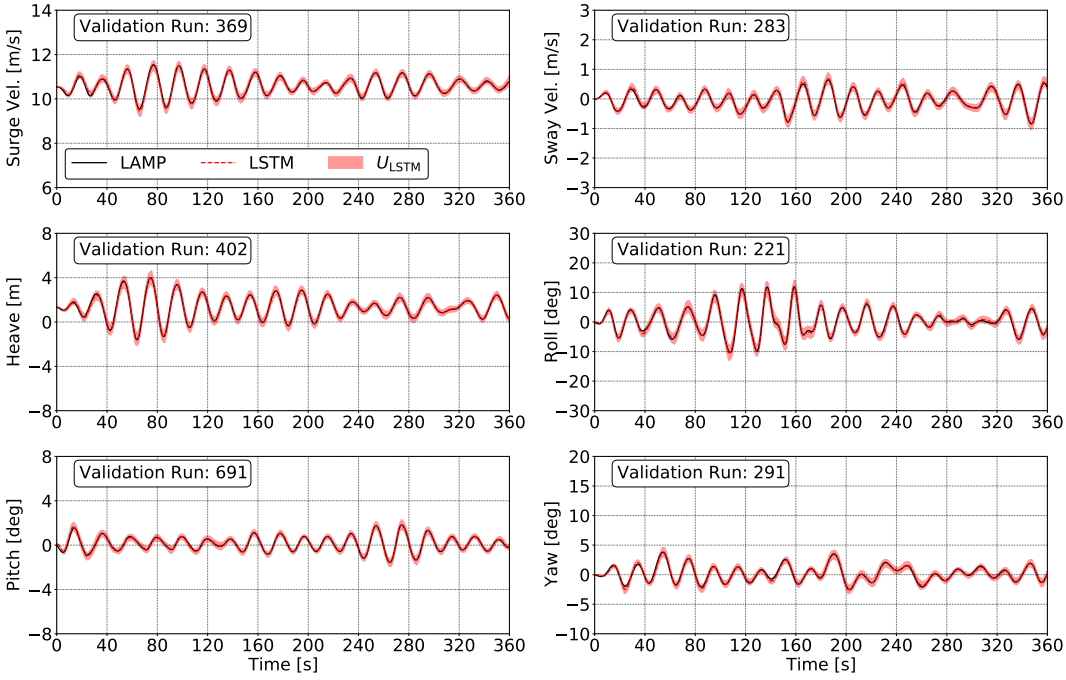

Figure 5.11: Best (ranked by L_∞ error) motion predictions for a model with 27 probes and 640 training runs in the course-keeping DTMB 5415 case study.

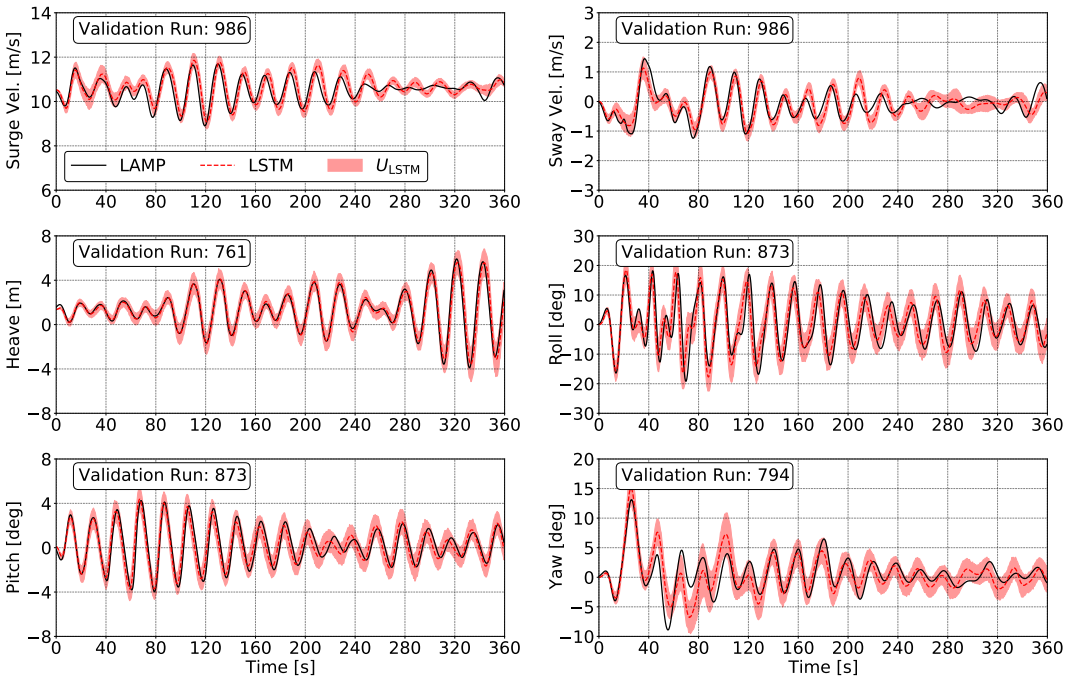

Figure 5.12: Worst (ranked by L_2 error) motion predictions for a model with 27 wave probes and 640 training runs in the course-keeping DTMB 5415 case study.

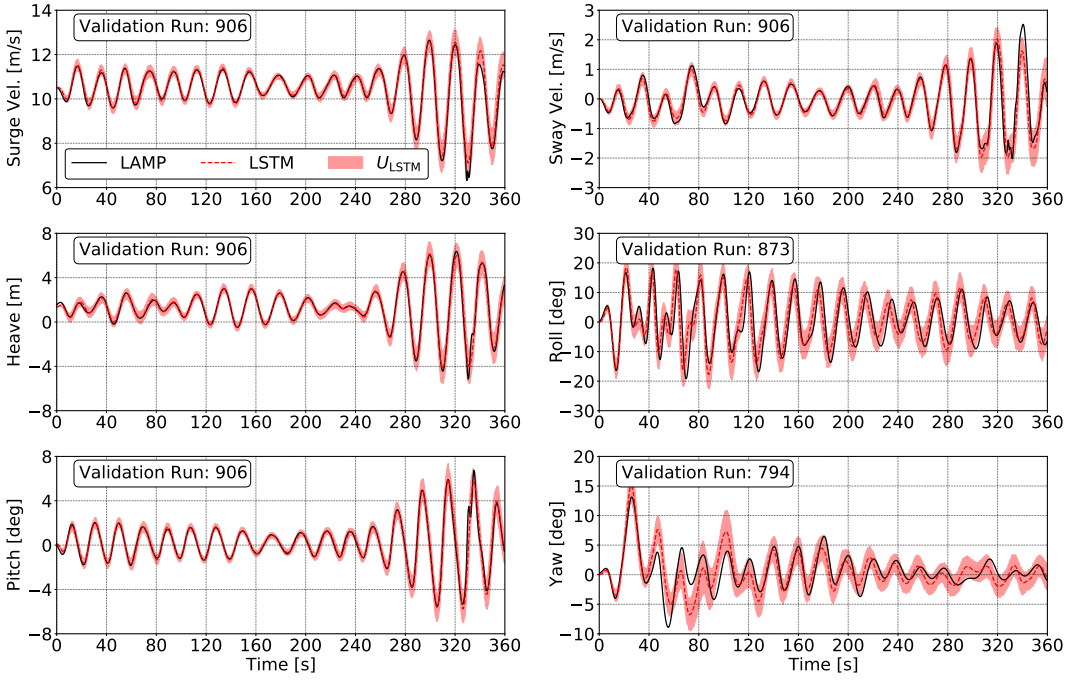

Figure 5.13: Worst (ranked by L_∞ error) motion predictions for a model with wave 27 probes and 640 training runs in the course-keeping DTMB 5415 case study.

Although temporal responses are critical for understanding the mechanisms of large amplitude responses, understanding the probability distribution of a particular response is necessary to produce a statistical description of the ship's operability. In particular, this dissertation is concerned with extreme events. Therefore, the models must be able to also represent extreme events. Comparisons of probability distributions also provide a useful method of validating models and have been used in previous research validating CFD tools in *Serani et al.* (2021).

Figure 5.14 shows a comparison of the probability distribution function (PDF) for each DoF, for models built with 27 wave probes and training data of 10, 80, and 640 runs. The PDF is displayed with a logarithmic scale to emphasize the response in the tails of the distributions, and also includes the uncertainty estimates from the neural network models using the Monte Carlo dropout technique. The neural network predictions perform well in reproducing motions larger than the statistical mean. However, the model trained with 10 runs demonstrates a larger difference for surge velocity and yaw. When the quantity of training data is increased, the models converge toward the LAMP predictions, and the uncertainty in the tail region also reduces. Figure 5.14 indicates that this approach, with some considerations about what wave sequences are considered during training, could be useful for predicting extremes. However, the models are limited by their training data, and it remains unlikely that any random set of training contains extremes. Therefore, targeted training runs containing extremes can provide an avenue forward for producing surrogate models that yield responses that are statistically representative of the high-fidelity predictions of the dynamical quantities.

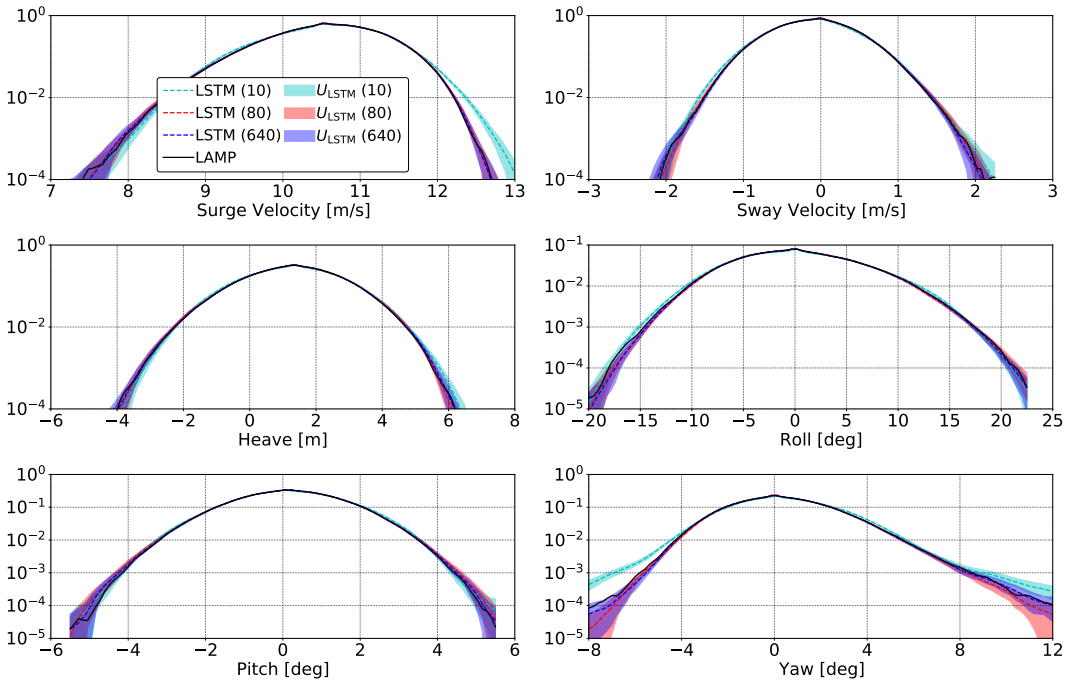

Figure 5.14: Comparison of the PDF tails for each DoF with models trained with 27 wave probes in the course-keeping DTMB 5415 case study.

A key limitation of the present methodology is that the encounter frame must be estimated, as the actual trajectory of the vessel in waves is not known *a priori*. Therefore, the wave probes utilized as input into the neural network models are not in the actual instantaneous encounter frame of the vessel. Considerable deviations between the estimated and actual frames can produce poor predictions. To investigate the accuracy of the estimated encounter frame methodology, separate models are built with 27 wave probes and the actual encounter frame from each training run. Predictions are also made with validation dataset with the new model as well as the actual encounter frame from each of those runs. The difference between these new set of models and the ones built with the estimated encounter frame, is a direct quantification of the consequences of estimating the encounter frame.

Figures 5.15 and 5.16 directly compare models with the actual and estimated encounter frames for both the L_2 and L_∞ error for each DoF. By utilizing the actual encounter frame in the training and inference of the model, the error is roughly half of the estimated frame. These comparisons indicate that a better estimate of the encounter frame could further reduce the error, without requiring more training data. Future research should explore an encounter frame estimator that is wave excitation-dependent to further improve the models presented.

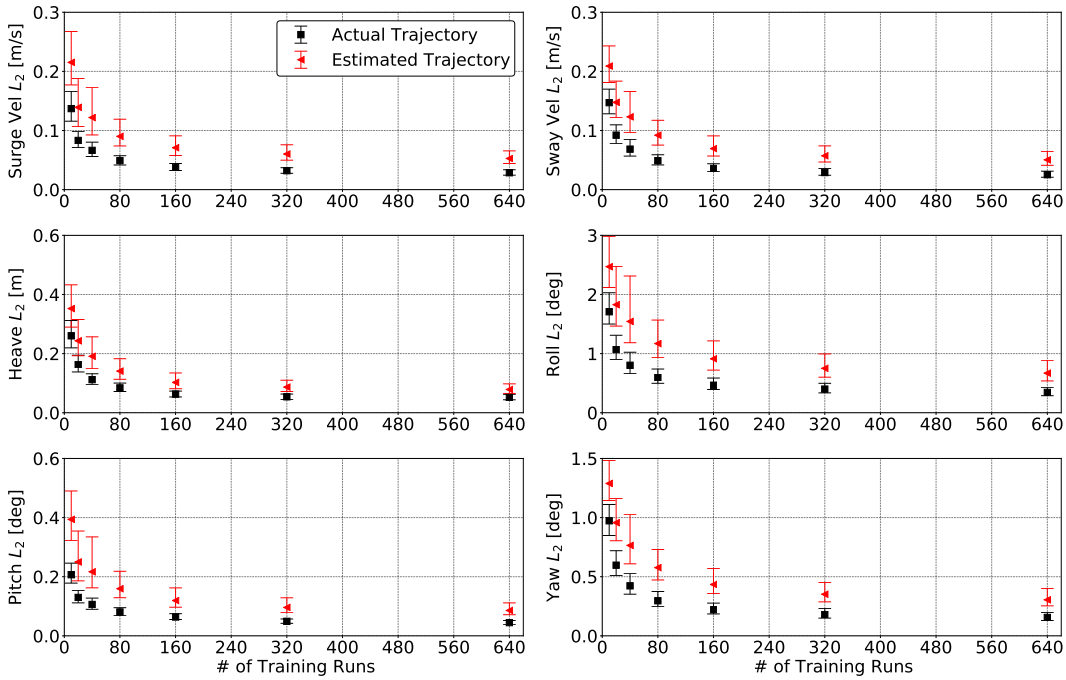

Figure 5.15: Comparison of L_2 error for each DoF with models trained with the actual and estimated encounter frames in the course-keeping DTMB 5415 case study.

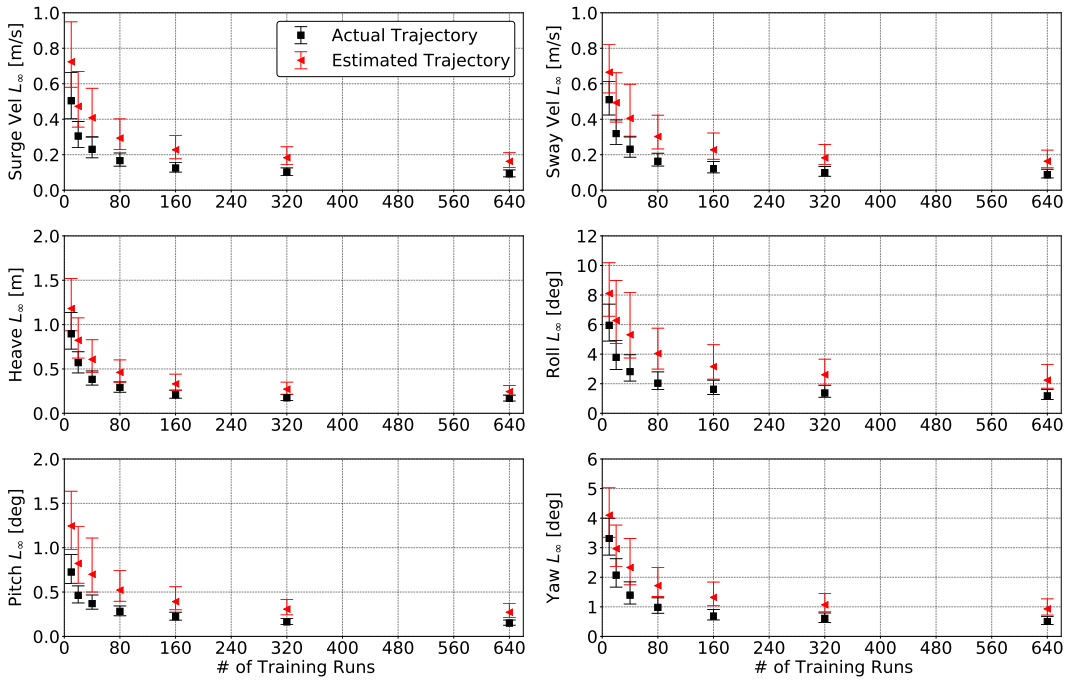

Figure 5.16: Comparison of L_∞ error for each DoF with models trained with the actual and estimated encounter frames in the course-keeping DTMB 5415 case study.

5.3.2 Turning Circle in Random Irregular Waves

A separate set of models are constructed for turning circle simulations. The models are then evaluated for their accuracy and convergence with respect to the quantity of input wave probes and training data in the same manner that is performed for the course-keeping case study. The turning circle models are built and evaluated identically to the course-keeping models, aside from the fact that the encounter frame is estimated and the models are trained and evaluated with turning circle simulations. Figures 5.17 and 5.18 show the comparison of L_2 and L_∞ error for each DoF for the turning circle case study with the validation runs. The trends are similar to what is observed for course-keeping, where increasing the quantity of wave probes and training data leads to a more accurate model. However, the decrease in error as the quantity of wave probes increases is less dramatic for the turning circles, and the overall error for all models is larger in comparison to the course-keeping.

Similar to the course-keeping case, the most accurate model for the turning circle case is built with 27 wave probes and 640 training data runs. Figures 5.19 and 5.20 illustrate the temporal response comparison between LAMP and the LSTM model for the validation runs with the lowest L_2 and L_∞ error for each DoF in the turning circle case study. Overall, the LSTM model predicts the 6-DoF response well with low uncertainty.

Figures 5.21 and 5.22 compare LAMP and the LSTM model built with 27 wave probes and 640 training data runs for the validation runs with the largest L_2 and L_∞ error for each DoF in the turning circle case study. Some regions of the temporal response are predicted well, while others reveal a large discrepancy between LAMP and the LSTM model that drives the error. The overall uncertainty in the time-histories is larger in those regions, which can provide an indicator of a lower-accuracy prediction. The response of the vessel in the turning circle leads to a higher frequency response than what is observed in the course-keeping simulations. The difference in response frequency could the cause of the overall error increase for the turning circle and indicates that these dynamical responses are more difficult to learn with the current methodology.

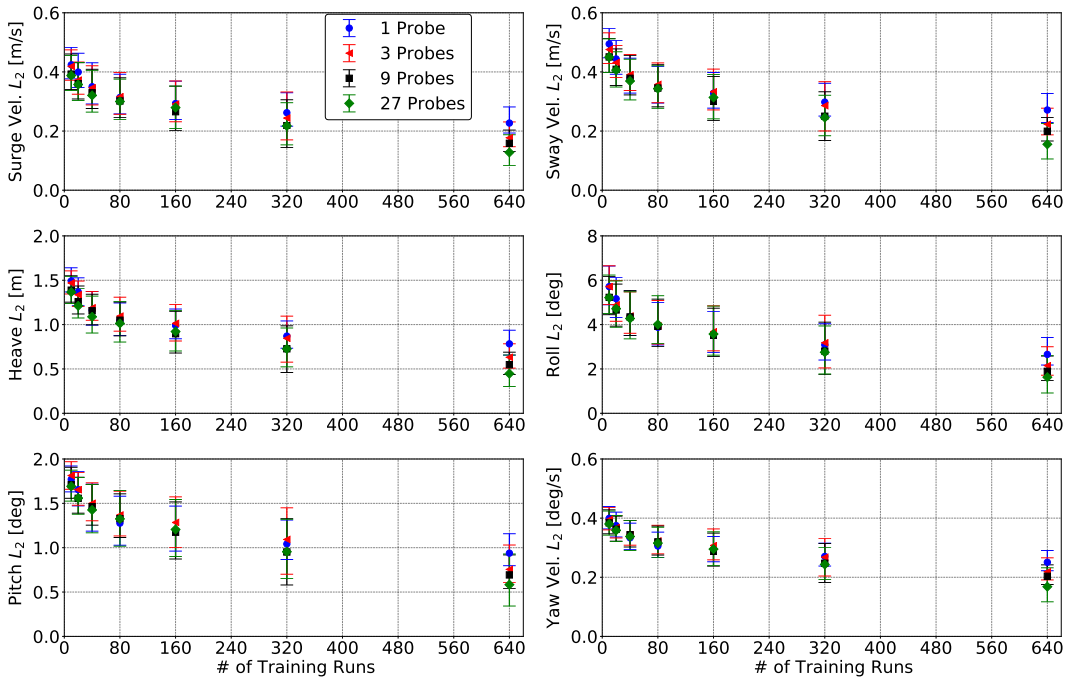

Figure 5.17: Comparison of L_2 error for each DoF in the turning circle DTMB 5415 case study.

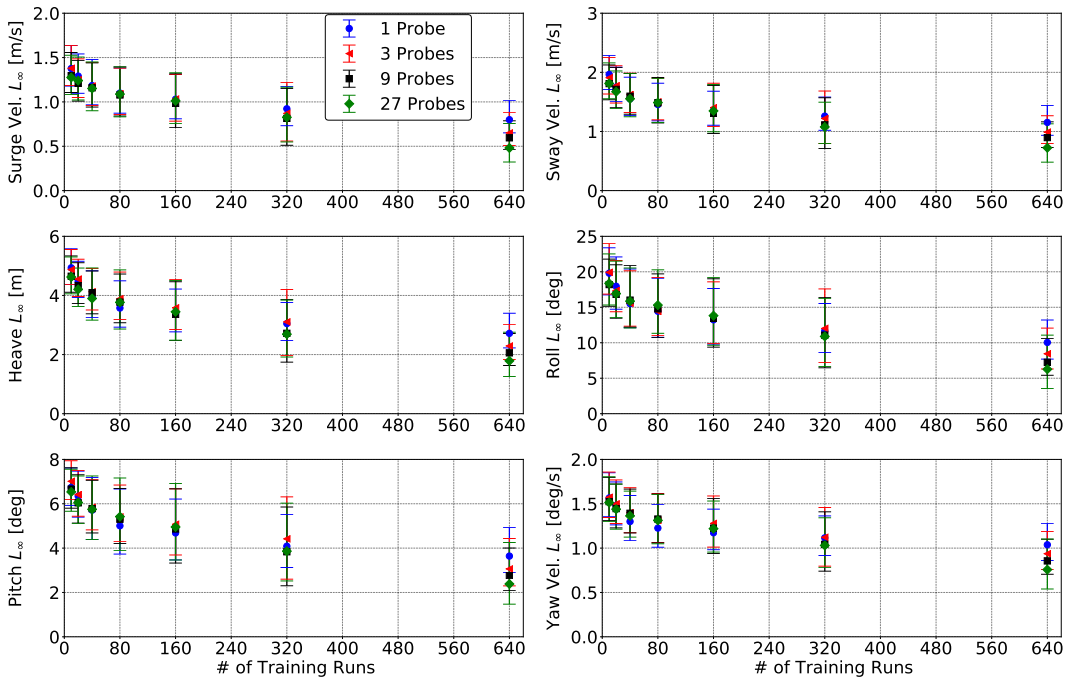

Figure 5.18: Comparison of L_∞ error for each DoF in the turning circle DTMB 5415 case study.

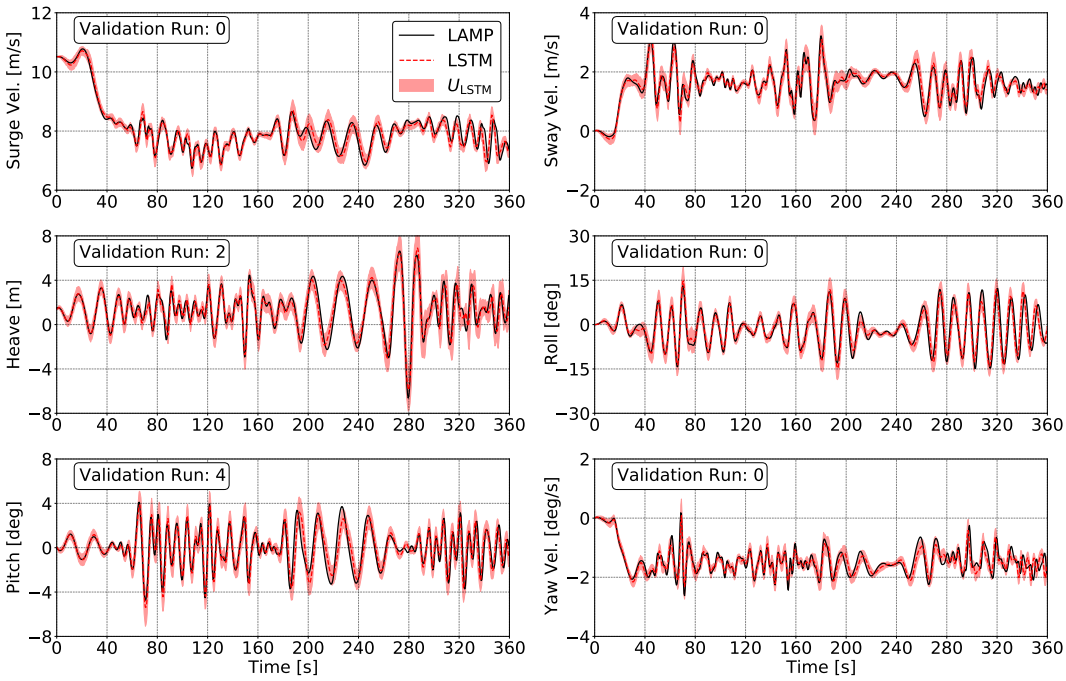

Figure 5.19: Best (ranked by L_2 error) motion predictions for a model with 27 probes and 640 training runs in the turning circle DTMB 5415 case study.

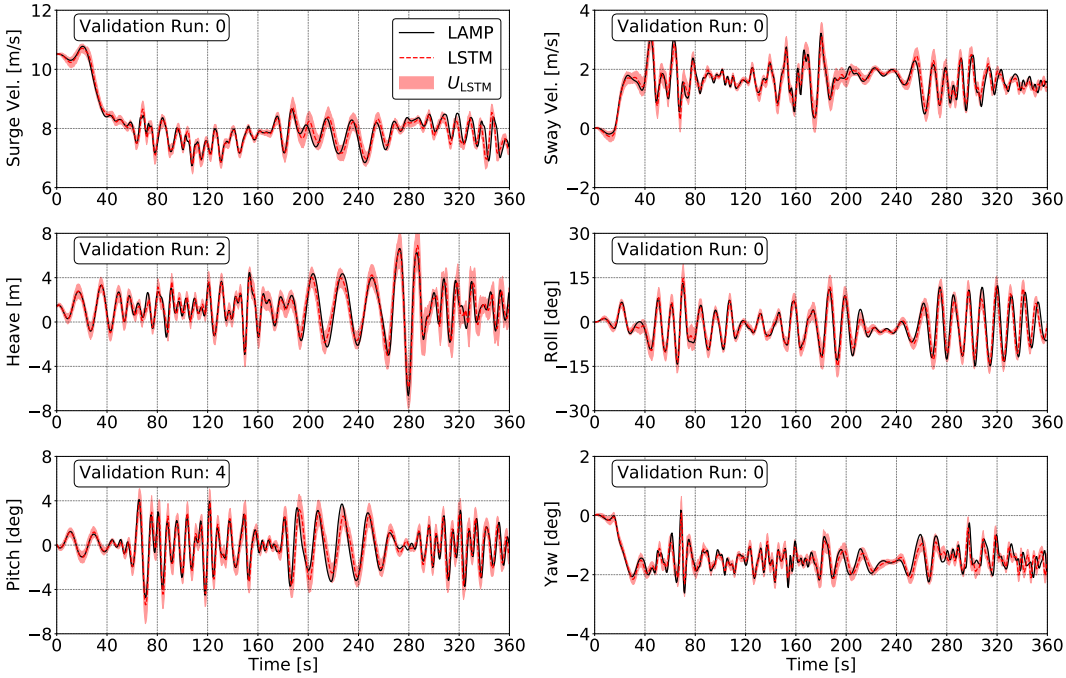

Figure 5.20: Best (ranked by L_∞ error) motion predictions for a model with 27 probes and 640 training runs in the turning circle DTMB 5415 case study.

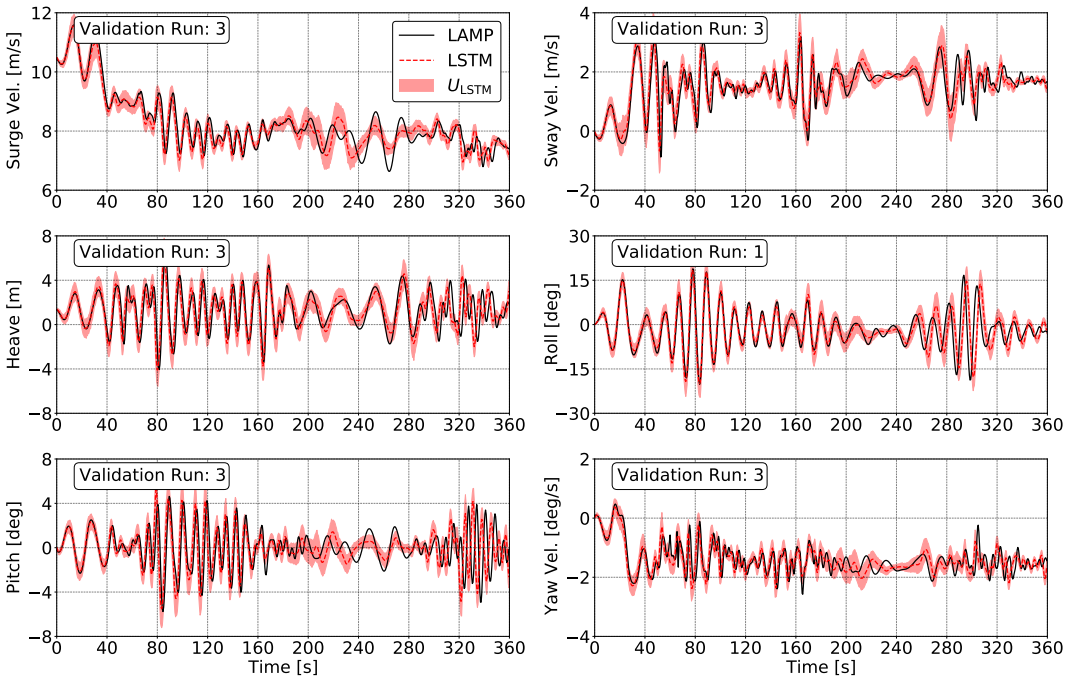

Figure 5.21: Worst (ranked by L_2 error) motion predictions for a model with 27 probes and 640 training runs in the turning circle DTMB 5415 case study.

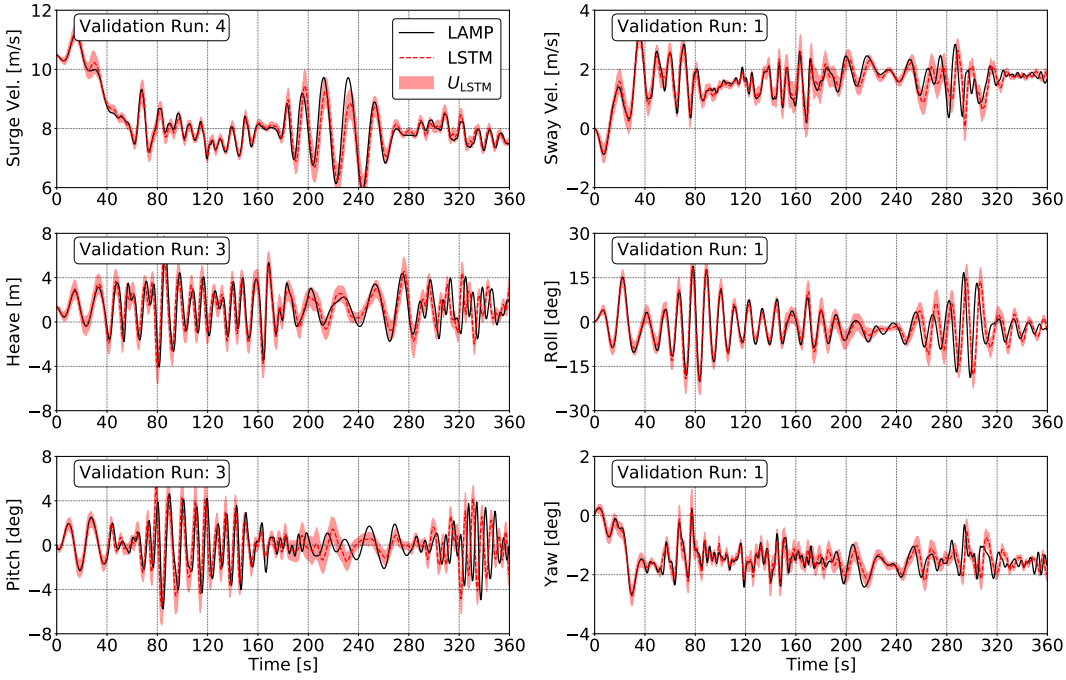

Figure 5.22: Worst (ranked by L_∞ error) motion predictions for a model with 27 probes and 640 training runs in the turning circle DTMB 5415 case study.

The comparison between LAMP and the LSTM models for the PDF of each DoF is displayed in logarithmic scale in Figure 5.23 for turning circle models built with 27 waves probes and training data quantities of 10, 80, and 640 runs. Similar to the course-keeping case study, Figure 5.23 shows that the PDF constructed from LSTM predictions closely represent the models trained with 80 and 640 runs. However, the model trained with 10 runs performs poorer than that of its course-keeping counterpart.

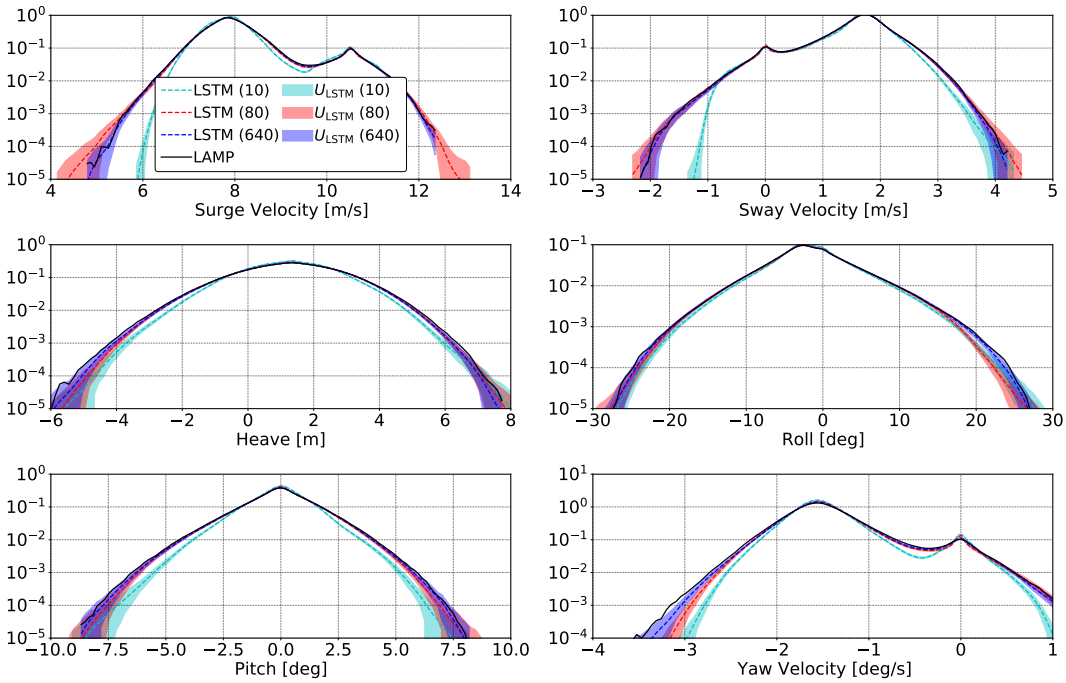

Figure 5.23: Comparison of the PDF tails for each DoF with models trained with 27 wave probes in the turning circle DTMB 5415 case study.

In all of the previous evaluations demonstrated for the turning circle LSTM models, the differences between LAMP and the LSTM predictions is shown again to be larger for turning circles than it is for course-keeping. Although the higher frequency response could be the root cause, the encounter frame is also much more complicated for the turning circle, as highlighted in Figure 5.5. Figures 5.24 and 5.25 illustrate the comparisons of different LSTM models built with 27 wave probes and 640 training runs for turning circles, where the only difference is the encounter frame. Again, the differences are much more dramatic for the turning circle, where knowing the actual frame can greatly improve the predictions made by the LSTM model. These results further indicate that an accurate prediction of the encounter frame will enhance the model's accuracy.

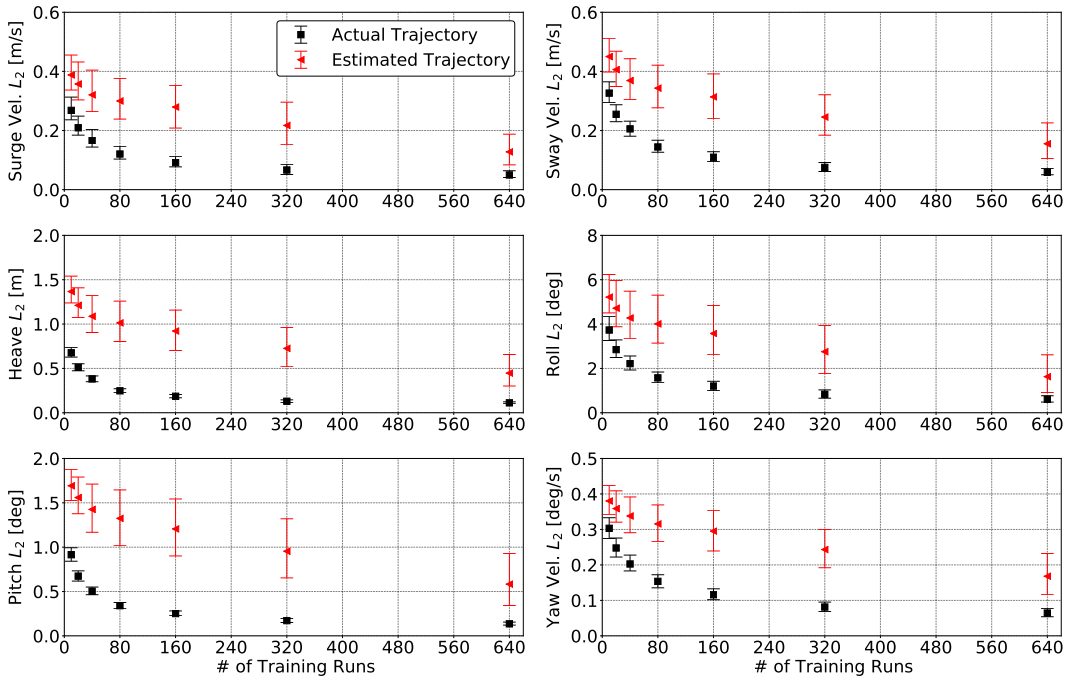

Figure 5.24: Comparison of L_2 error for each DoF with models trained with the actual and estimated encounter frames in the turning circle DTMB 5415 case study.

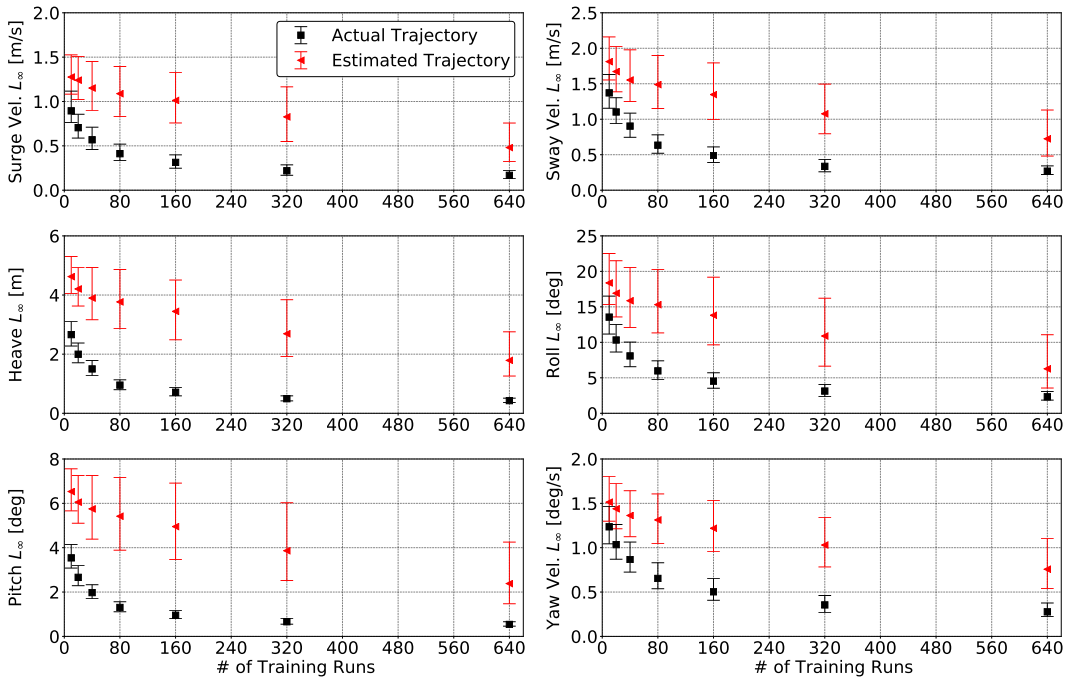

Figure 5.25: Comparison of L_∞ error for each DoF with models trained with the actual and estimated encounter frames in the turning circle DTMB 5415 case study.

5.4 Case Study: Multiple Speeds, Headings and Sea States

Sections 5.3.1 and 5.3.2 describe case studies for the DTMB 5415 for course-keeping and turning circles, respectively, for a single vessel speed, relative wave heading, and sea state. However, predictions of vessel response are typically required for multiple maneuvers, ship speeds, wave headings, and sea states. Training separate models for each condition requires sufficient data at each discrete condition and the individual models are not capable of producing predictions for alternative conditions. Therefore, a generalized model capable of producing predictions for multiple conditions is extremely desirable.

The case study in this section extends the case studies in Sections 5.3.1 and 5.3.2 to multiple speeds, headings, and sea states. Table 5.5 outlines the operating and seaway conditions considered. The dataset consists of a total of 60 conditions comprising of

four speeds, five headings, and three seaways, all representing the top of the sea state in terms of H_c and the most probable modal period with respect to T_p.

Table 5.5: Operating and seaway conditions for the DTMB 5415 case study with multiple conditions.

Properties	Units	Value
Speeds	knots	5, 10, 20, 30
Wave Heading	deg	0, 45, 90, 135, 180
Sea State	-	4, 5, 6
Significant Wave Height, H_s	m	2.5, 4.0, 6.0
Peak Modal Period, T_p	s	8.8, 9.7, 12.4
Spectrum	-	Bretschneider
Fourier Components	-	250
Proportional Gain, G_p	deg/deg	4
Integral Gain, G_i	1/s	0
Differential Gain, G_d	deg/(deg/s)	1
Max Rudder Rate, $\dot{\delta}_{\max}$	deg/s	9
Max Rudder Deflection, $\delta_{\max}$	deg	35

The case study explores four different modeling approaches. The *general* approach trains the model with data from all conditions. The *speed*, *heading*, and *sea state* approaches each consider data for a discrete speed, heading, and sea state, respectively. For example, there are four speeds considered in the case study. Therefore the *speed* approach would build an individual model for each discrete speed. The same is true for the *heading* and *sea state* approaches. The four different modeling approaches are employed to investigate the accuracy of the *general* approach to develop models that are generalized across a wide range of conditions. For all the approaches, there is a separate encounter frame estimated for each speed, heading, and sea state.

Table 5.6 describes the neural network architecture as well as the training and validation datasets. The datasets are divided such that each modeling approach uses the same training data. The only difference is the manner in which the data is divided between the models. For example, the 3,840 training runs for the *general* approach is the same dataset as the four *speed* approach models with 960 training runs each. All of

the modeling approaches are evaluated on the same validation dataset as well, which is divided similarly to the training dataset across the approaches. All the constructed models considered 27 wave probes for the input wave elevation.

Table 5.6: Training matrix, neural network architecture, and hyper-parameters for the DTMB 5415 case study with multiple conditions.

Properties	Units	Value
Total Training Runs	-	60, 120, 240, 480, 960, 1920, 3840
Training Runs/Model (*Speed*)	-	15, 30, 60, 120, 240, 480, 960
Training Runs/Model (*Heading*)	-	12, 24, 48, 96, 192, 384, 768
Training Runs/Model (*Sea State*)	-	20, 40, 80, 160, 320, 640, 1280
Total Validation Runs	-	6000
Validation Runs/Model (*Speed*)	-	1500
Validation Runs/Model (*Heading*)	-	1200
Validation Runs/Model (*Sea State*)	-	2000
Total Wave Probes	-	27
Time Steps per Run	-	720
Individual Run Length	s	360
Units per Layer	-	250
Layers	-	3
Dropout	-	0.1
Learning Rate	-	0.00001
Epochs	-	2000
Optimizer	-	Adam (*Kingma and Ba*, 2014)

Figures 5.26 and 5.27 depict the L_2 and L_∞ error across all the modeling approaches for various quantities of training data. Each marker denotes the median error for all of the validation runs, while the upper and lower error bars correspond to the 75% and 25% quantiles, respectively. Overall, the *general* approach is the most accurate, and the *heading* approach is the least accurate across all DoF and quantities of training data. Additionally, with less total training data, the *general* and *sea state* approaches are more accurate than the other two approaches. The higher accuracy of the *sea state* approach is due to the training runs spanning a range of different speeds and headings, as well as more training data per model. With a sufficient amount of training data, all of the approaches converge and the differences between them decrease.

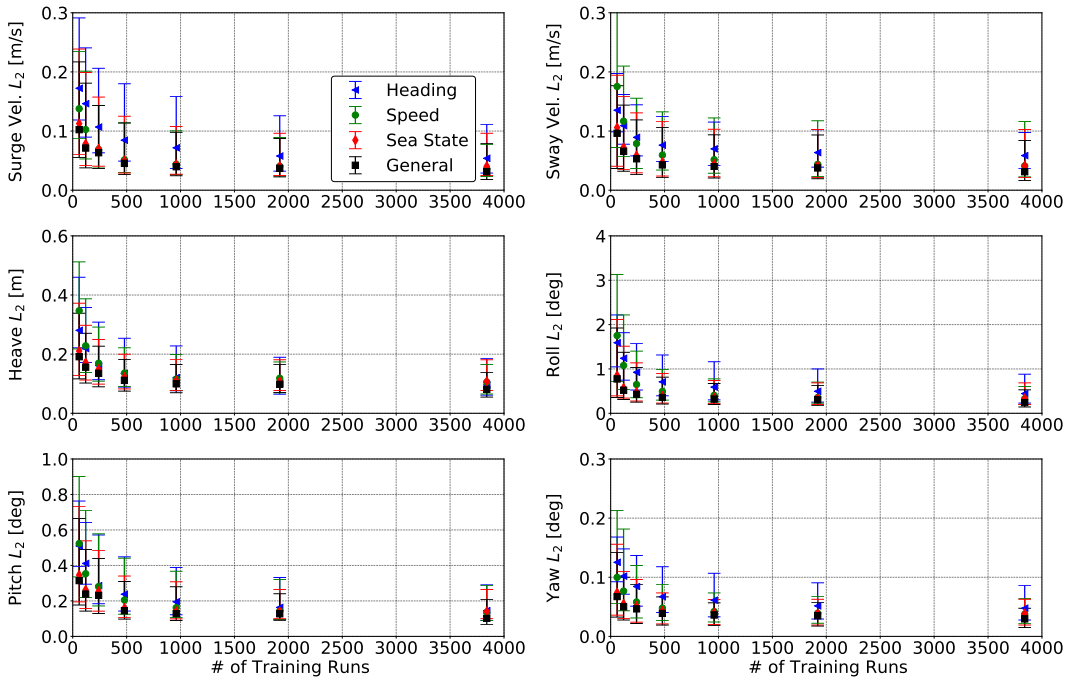

Figure 5.26: Comparison of L_2 error for each DoF with different modeling approaches for the DTMB 5415 case study with multiple conditions.

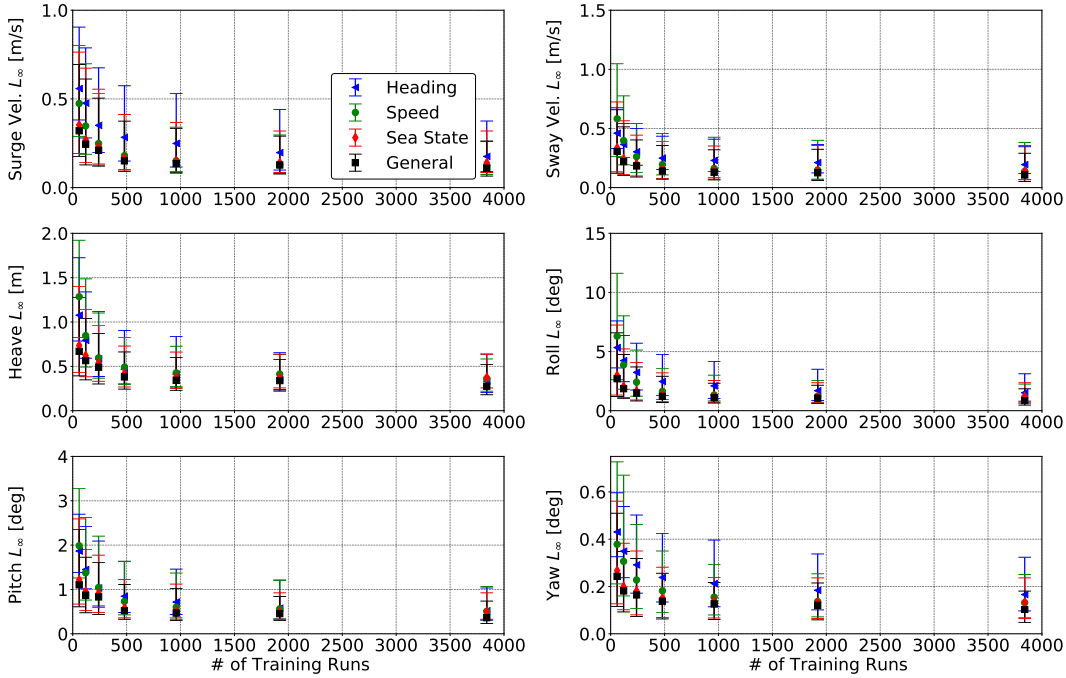

Figure 5.27: Comparison of L_∞ error for each DoF with different modeling approaches for the DTMB 5415 case study with multiple conditions.

Figures 5.28 and 5.29 compare the validation runs with the smallest L_2 and L_∞ error for each DoF using the general approach LSTM models trained with 3840 simulations, consisting of multiple speeds, headings, and sea states. Overall, the LSTM predictions match the phase and amplitude of the best-predicted LAMP validation runs for all the DoF.

Figures 5.28 and 5.29 compare the validation runs with the largest L_2 and L_∞ error for each DoF utilizing the general approach LSTM models trained with 3,840 simulations, comprising of multiple speeds, headings, and sea states. The results in Figures 5.28 and 5.29 consist of the worst-predicted validation runs that the LSTM model produced. In general, the LSTM model still yields responses that are representative of the LAMP predictions.

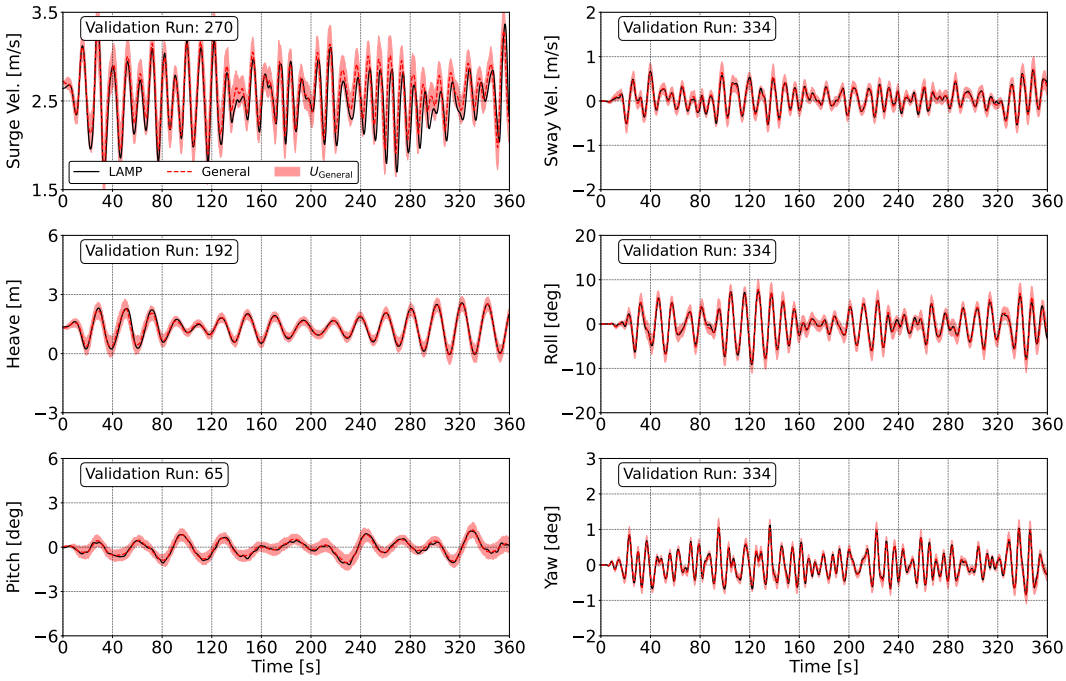

Figure 5.28: Best (ranked by L_2 error) motion predictions from the general approach for the DTMB 5415 case study with multiple conditions.

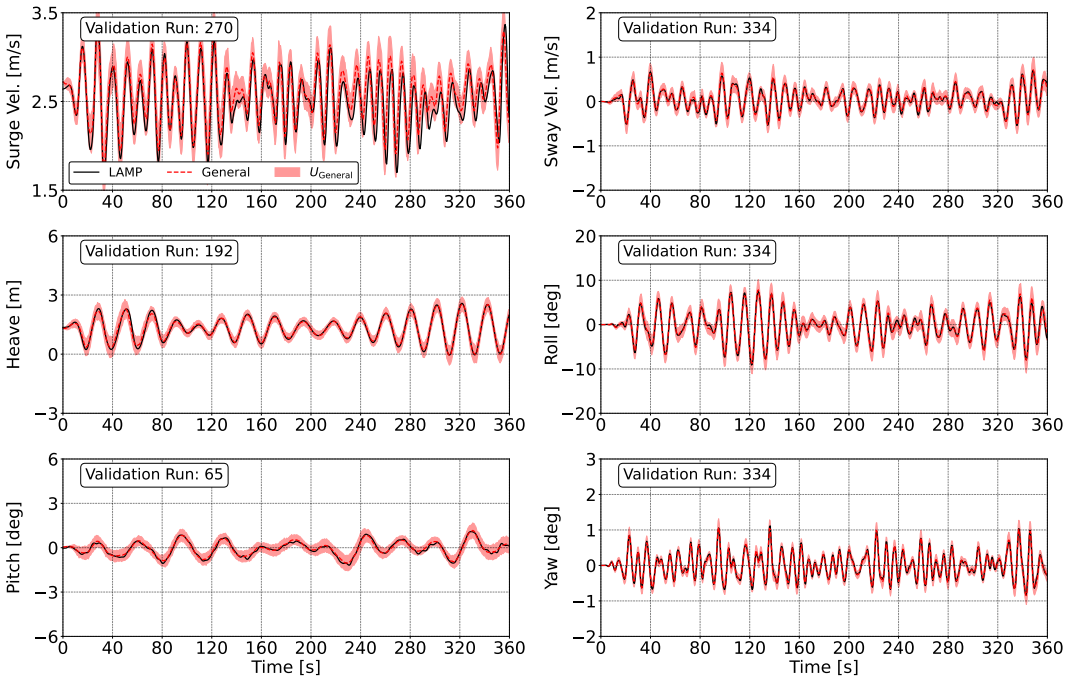

Figure 5.29: Best (ranked by L_∞ error) motion predictions from the general approach for the DTMB 5415 case study with multiple conditions.

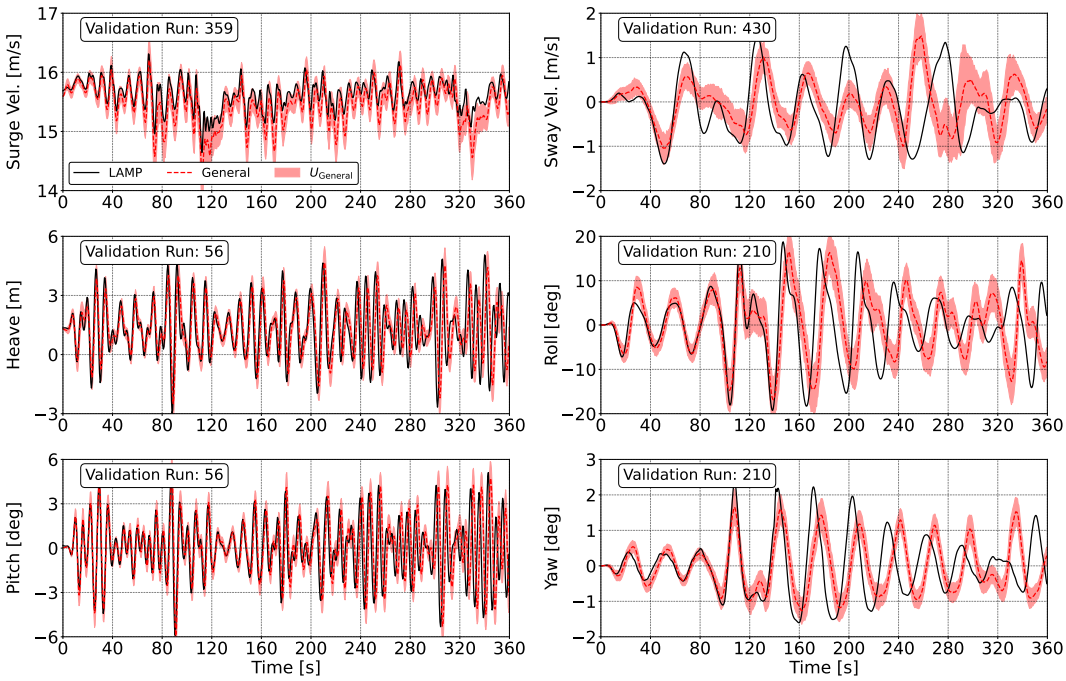

Figure 5.30: Worst (ranked by L_2 error) motion predictions from the general approach for the DTMB 5415 case study with multiple conditions.

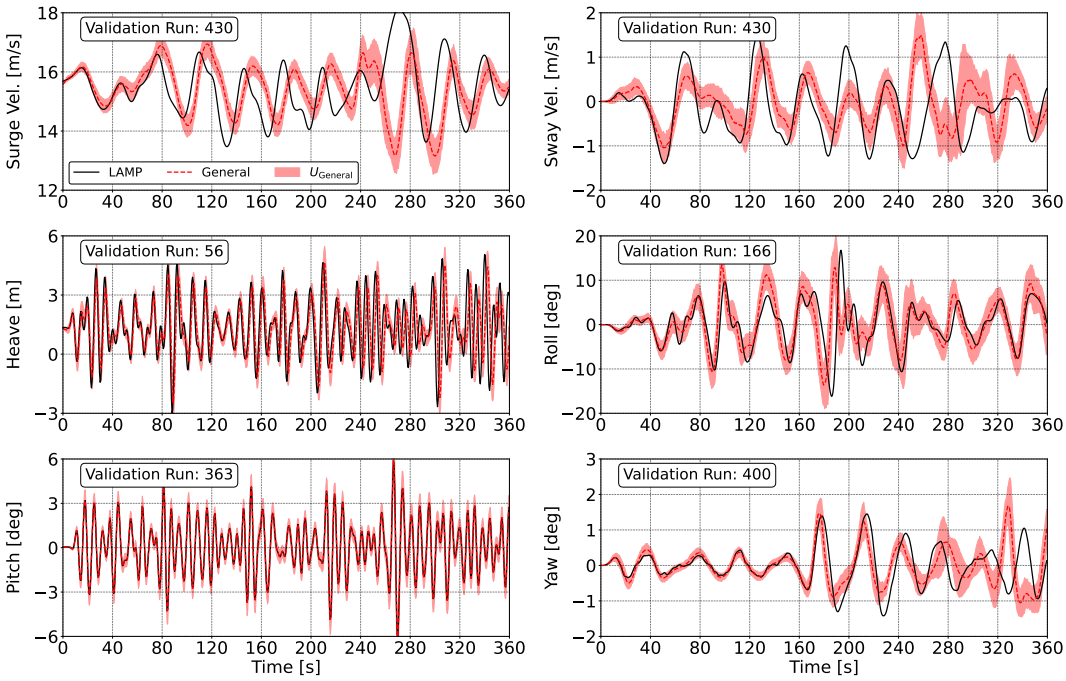

Figure 5.31: Worst (ranked by L_∞ error) motion predictions from the general approach for the DTMB 5415 case study with multiple conditions.

Introducing the general approach to LSTM modeling methodology shows promise in developing models that can predict ship responses for arbitrary speeds, headings, and sea states. However, the difference between the estimated and actual encounter frames is exacerbated when the models must now consider an estimated frame for each individual condition that differs from the actual frame of each condition and irregular wave train. Future research developing enhanced predictions of the estimated encounter frame could enable the general methodology to increase in accuracy greatly and possibly reduce the computational cost of training the models.

CHAPTER VI

CCS Framework

The CWG method, CFD, and LSTM neural networks described in Chapters II, III, and V provide an avenue forward, not only for efficiently quantifying the probability of extreme ship response events, but also observing them to understand the mechanisms that trigger them. This chapter presents the CCS framework, which combines the best aspects of each of these methodologies into a single system that can systematically observe and quantify extreme events practically, efficiently, and without inherent dynamic constraints. An overview of the proposed framework for implementing the CWG method with CFD and LSTM neural network surrogate models is outlined in Figure 6.1. Although LSTM neural networks are considered in this dissertation, any prediction-focused surrogate modeling technique would be appropriate provided it maintains the same accuracy shown for the LSTM. The framework begins with the selection of a vessel and its respective properties (loading condition, appendages, autopilot, etc.), the speed, the heading, the maneuver (*e.g.* course-keeping, turning circle, etc.), the seaway description, the response of interest, and the thresholds to characterize exceedances, as well as the selection of response quantities for encounter conditions. The selection of these parameters sets the stage for the remainder of the framework and the associated probability calculations.

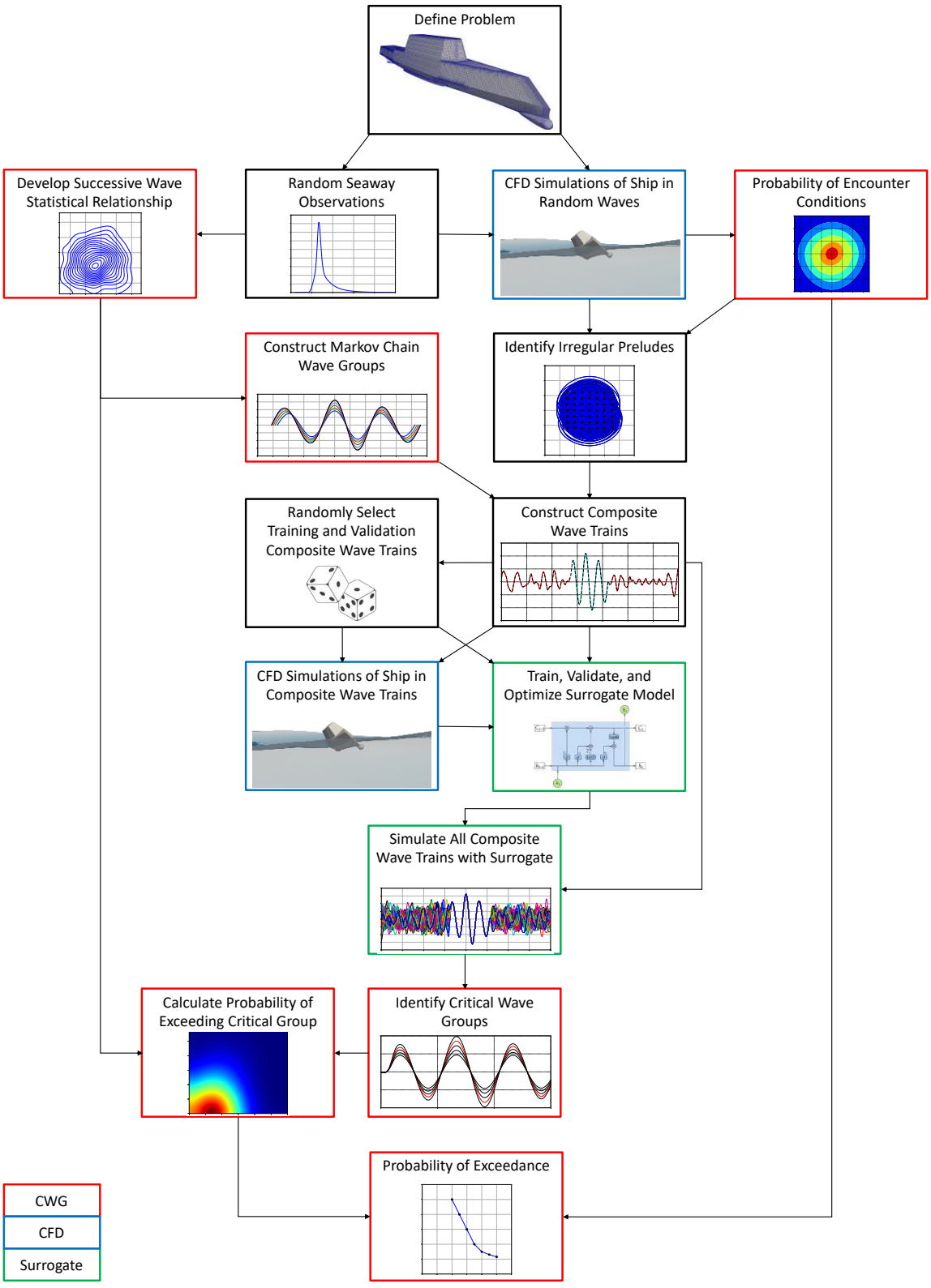

Figure 6.1: Flow chart of the proposed CCS framework.

The seaway is described with a random wave spectrum, such as the Bretschneider (*Bretschneider*, 1959) or JONSWAP (*Hasselmann et al.*, 1973), which are typically defined by a significant wave height H_s and the peak modal period T_p. An example wave spectral density, S is depicted in Figure 6.2, where S is described as a function of the wave frequency ω.

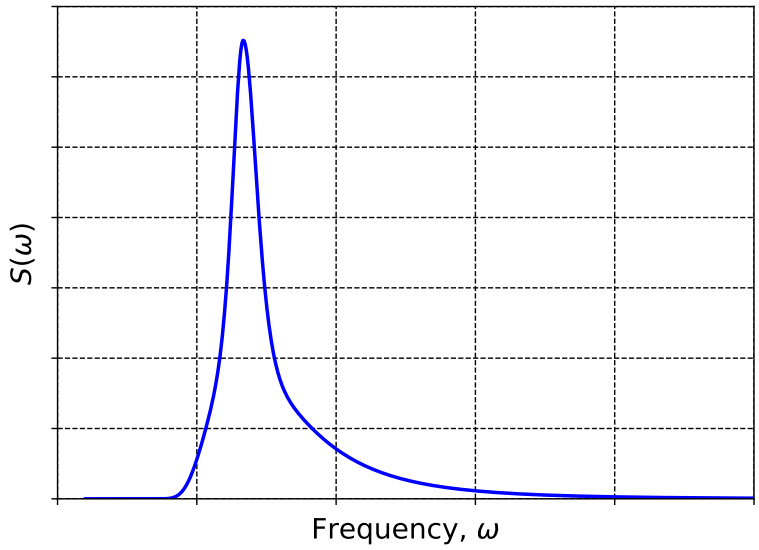

Figure 6.2: Example JONSWAP wave spectrum.

The wave spectrum is then discretized into F Fourier components with uniform frequency spacing $d\omega$, and the amplitudes are described by:

$$a_f \;=\; \sqrt{2\; S_f\; d\omega} \tag{6.1}$$

where S_f reflects spectral density at the f^{th} frequency. With the wave spectrum discretized into amplitudes a_f and frequencies ω_f, random phases ϕ_f are generated with uniform random sampling from 0 to 2π to produce independent and random realizations of a unidirectional wave field η, with respect to time t and space $\mathbf{x}$:

$$\eta\left(\mathbf{x},t\right) \;=\; \sum_f a_f cos\left(\omega_f t \;-\; \mathbf{k}_f \cdot \mathbf{x} \;+\; \phi_f\right) \tag{6.2}$$

Several realizations ($\geq$100,000 hours) of the wave field are produced with Equation 6.2 at the origin $(x, y = 0)$ and individual waves are identified in the observations by detecting all zero-upcrossings. The period of each wave is calculated with the time between the zero-upcrossings and the wave height is calculated by adding the maximum and minimum wave elevation between zero-upcrossings. With wave heights and periods for each individual wave, the height and period of the waves directly preceding and following each wave are also recorded. The identification of these successive waves allows for the development of the statistical relationships that are needed to build the deterministic wave groups with Markov chains and calculate their associated probabilities (see Section 2.2).

When constructing the deterministic wave groups, the values for H_c, T_c, and j need to be selected specifically for the desired problem to ensure an exhaustive collection of the possible wave groups. This dissertation utilizes values of H_c of 4σ, 5σ, 6σ, 7σ, 8σ, and 9σ, T_c values of T_p - $2\Delta T$, T_p - ΔT, T_p, T_p + ΔT, and T_p + $2\Delta T$, and j of one and two, where σ is the standard deviation of the wave height, T_p is the peak modal period, and ΔT is the size of the m wave period ranges, which is set to a full scale value of one second in this dissertation, in accordance with *Anastopoulos and Spyrou* (2019). The selection of H_c, T_c, and j should be catered to the problem of interest, as different responses may be excited by modal periods outside the outlined period ranges or could be more sensitive to resonance and require larger values of j.

Additionally, CFD simulations of the vessel in random waves described by Equation 6.2 are performed to characterize the probability of the encounter conditions, the selection of the encounter conditions, and the identification of the irregular preludes (*i.e.* random wave trains that lead to the encounter condition of interest). The random wave ship simulations are focused on recognizing *non-rare* ship response events and typically only require on the order of 0.5 full-scale hours of exposure time (100 encounters), as opposed to the large amount observations necessary to develop

statistical relationships for wave groups. All of the simulations that record an event matching the selected encounter conditions within 1% are identified. The instances with lowest combined percent difference are selected as the primary irregular preludes. However, recording all of the instances that matched the initial conditions within 1% allows for ensembles of equivalent encounter conditions to be simulated in order to better understand if the selected states are appropriate for the problem, or if another quantity shows considerable influence.

After the irregular preludes are identified and the deterministic wave groups are constructed, the wave groups are embedded into the irregular preludes to create composite wave trains utilizing the blending methodology outlined in Section 4.1. A Fast Fourier Transform (FFT) is then applied to the composite wave train in the encounter frame to retrieve Fourier components in accordance with Equation 6.2. From the newly constructed composite wave trains, M composite waves are randomly selected for training, V composite wave trains are randomly selected for validation, and the $M + V$ cases are simulated with CFD to predict the corresponding ship response. Typical values for M and V are 400 and 100, respectively, which represents a 80/20 split for training and validation.

After all of the CFD simulations are complete, an LSTM neural network is trained with the M simulations. The resulting model is evaluated with the V validation simulations and the hyper-parameters are tuned to gain the best performance. This tuning is repeated until the best parameters are found for the M training simulations. The resulting neural network model then predicts the ship response due to all of the constructed individual composite wave trains. The case studies presented in Chapters VII and VIII provide insight into the quantity of M and V required to produce an accurate representation of the extreme events.

For each of the composite wave train predictions, the maximum response of the quantity of interest is recorded. The maximum of the quantity interest is calculated

within the time window $t_e \leq t \leq t_e + T_c(j+2)$ to ensure that maximum response occurs either during the wave group or directly following it. Therefore, for every encounter condition, H_c, T_c, and j, there is a corresponding maximum response. At each threshold ϕ_{crit}, and for each encounter condition, T_c, and j, the values of H_c and the maximum response are interpolated to distinguish the H_c that corresponds to a near exceedance of the threshold of interest, thus identifying all of the critical wave groups. The probability of exceeding each of these critical wave groups can then be calculated with Equation 2.15. With the probability of encounter conditions and all the critical wave groups pinpointed, as well as their associated probabilities calculated at each threshold, the probability of exceedance in Equation 2.6 is found. Additionally, the LSTM models each contain uncertainty estimates from the Monte Carlo dropout approach. Therefore, the upper and lower bands of the LSTM uncertainties can also be employed to uncover their own separate critical wave groups that have associated probabilities. The critical wave groups associated with the uncertainty estimates can then be compiled to produce uncertainty estimates for the the probability of exceedance calculations. The resulting uncertainty is solely based on the LSTM models.

Combining the CWG method, CFD, and LSTM neural networks into the CCS framework, described in this chapter, allows for a holistic and quantitative probabilistic evaluation and observation of extreme ship response events. The developed framework requires as few assumptions as possible, and produces realistic extreme events without unnatural dynamical constraints that are only suitable for simplified lower fidelity hydrodynamic predictions.

6.1 Uncertainty in Initial Conditions

The natural initial condition methodology enables the enforcement of prescribed encounter conditions through an irregular prelude and produces physically realizable

wave trains with embedded deterministic wave groups. If the entire body and fluid states were captured in the encounter condition, then the response to the deterministic wave group would be deterministic. However, this is impractical and requires discretization of the high-dimensional combination of the flow field and body state. Therefore, the encounter condition is a reduced-order series of quantities that attempts to summarize the dominating contributions of both the state of the body and the fluid. In the example of extreme roll, the encounter conditions are typically the roll and roll velocity. The roll and roll velocity attempt to capture all of the body dynamics and hydrodynamics into two simplified quantities. In the context of the natural initial condition, an infinite number of combinations of body and fluid states can lead to the same encounter condition for a free-running vessel. The irregular prelude only ensures that the prescribed encounter condition occurs, but it does not guarantee that the resulting ship response will be identical for different irregular preludes with the same encounter condition. Therefore, an uncertainty estimate is required to quantify the variation due to different irregular preludes.

It is important to quantify the uncertainty due to different irregular preludes that lead to the same encounter condition and understand how it propagates through the different calculations into the probability of exceedance calculations. In the case of the CWG method, the uncertainty from the irregular preludes is easily defined in the identification of critical wave groups. Figure 6.3 illustrates example observations of the absolute maximum roll for 18 different irregular preludes of the same encounter condition for wave groups with different H_c but the same shape (T_c and j). The variation of the maximums across different irregular preludes with the same encounter condition can vary across all observations with the same H_c.

A critical wave group can be identified for each irregular prelude at the various critical roll angle thresholds ϕ_{crit}, through the interpolation of H_c and and the absolute maximum roll predictions in Figure 6.3. Figure 6.4 demonstrates the mean and

uncertainty in the prediction of H_c, from the different irregular preludes for the same encounter condition. Different levels of uncertainty are shown in terms of the standard deviation s of the H_c predictions across all the irregular preludes. Overall, the uncertainty due to the irregular preludes increases as the critical roll angle threshold increases and there is more variation the roll response.

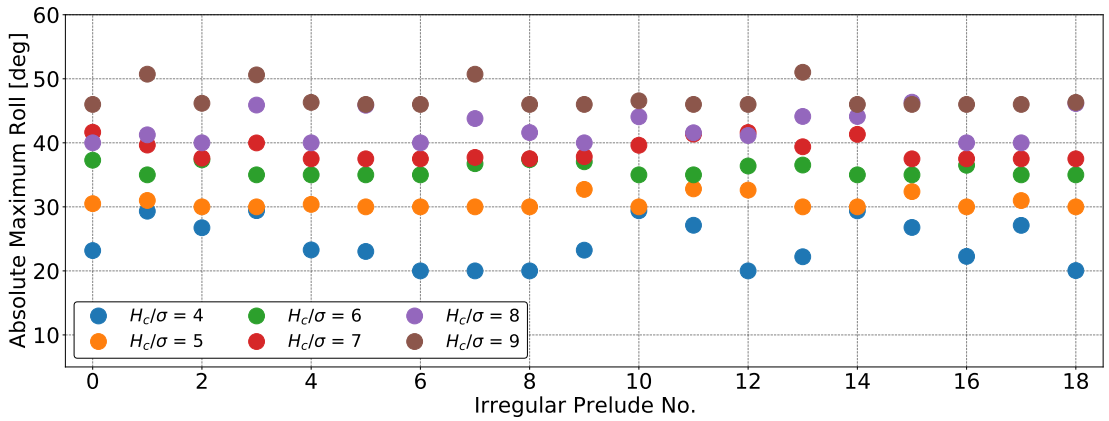

Figure 6.3: Example absolute maximum roll for different irregular preludes of the same encounter condition for wave groups with different H_c but the same shape (T_c and j).

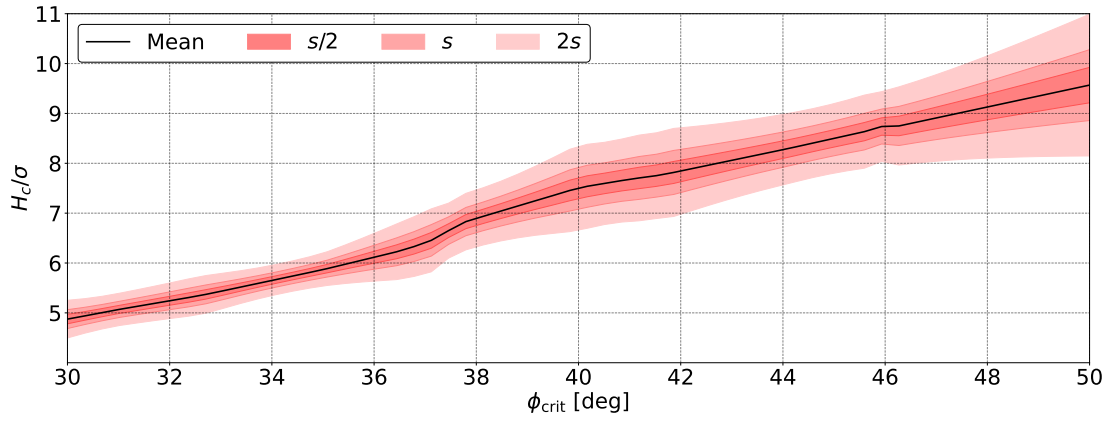

Figure 6.4: Illustration of quantification of the uncertainty due to the irregular preludes through the identification of critical wave groups.

Once the critical wave groups are identified as shown in Figure 6.4, they can be evaluated probabilistically for the mean, as well as a lower and upper bound,

individually with the CWG methodology in Chapter II. The only difference between the probability calculations would be that the mean, lower bound, and upper bound, all of their own set of unique critical wave groups for each encounter condition and wave group shape. The probability of encounter conditions remains the same and is independent of this irregular prelude variation.

If the uncertainty due to the irregular prelude were to be quantified purely with CFD without LSTM neural networks, the increase in computational cost would scale linearly with the quantity of irregular preludes per encounter condition. To maintain the accuracy and the decrease in computational cost that the LSTM provides, the training dataset should include some variation in irregular prelude for the same encounter condition so that the models better understand this variation. Currently, the same wave trains are used to develop irregular preludes for multiple encounter conditions and may introduce bias to the models. This section describes a methodology for quantifying the uncertainty due to the irregular prelude through identifying a different set of critical wave groups for a mean response as well as an upper and lower bound. However, this dissertation does not consider this uncertainty in the provided case studies and the procedure is described here to guide future exploration in the implementation of this methodology. Future research will have to investigate this phenomena further and quantify the uncertainty for a case study with a free-running vessel.

CHAPTER VII

Case Study: 2-D 2-DoF ONR Tumblehome Midship Section

This chapter presents a case study utilizing the CCS framework for a full-scale 2-D midship section of the ONRT geometry with bilge keels (*Bishop et al.*, 2005) shown in Figure 7.1 at zero speed in beam seas that is only free to heave and roll. A 2-D Two Degrees-of-Freedom (2-DoF) midship section is selected to evaluate CCS framework because it provides a problem with strong nonlinearity, but allows for events to be simulated quickly in order to demonstrate the framework's ability to calculate the probability of exceedance and to do so efficiently with a LSTM neural network.

The case study uses a JONSWAP spectrum (*Hasselmann et al.*, 1973) with a peak enhancement factor of 3.3 and a significant wave height $H_s = 7.5$ m, and a peak modal period $T_p = 15$ s, corresponding to a Sea State 7 (*NATO*, 1983) with longcrested seas. The response quantity of interest for the case study is the roll angle, and the probability of exceedance is evaluated for roll angles ranging from 30 to 57.5 deg. The roll angle and velocity are chosen to be the encounter conditions for the CWG method. The hull and fluid properties are shown in Table 7.1. The loading condition for the current study is derived from *Bishop et al.* (2005), where the vertical center of gravity KG is selected to achieve a transverse metacentric height GMT of 1.5 m.

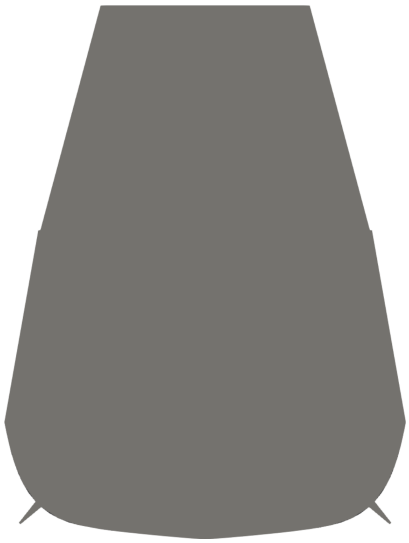

Figure 7.1: 2-D ONRT midship section geometry.

Table 7.1: Loading condition and fluid properties of the 2-D ONRT midship section.

Properties	Units	Value
Beam, B	m	18.8
Draft, T	m	5.5
Vertical Center of Gravity, KG (ABL)	m	7.881
Transverse Metacentric Height, GMT	m	1.5
Roll Gyradius, k_{xx}	m	7.118
Density of Water, ρ_w	kg/m^3	1000
Density of Air, ρ_a	kg/m^3	1
Kinematic Viscosity of Water, ν_w	m^2/s	1e-06
Kinematic Viscosity of Air, ν_a	m^2/s	1.48e-05
Accel. due to Gravity, g	m/s^2	9.80665

7.1 Mesh Sensitivity

Three separate 2-D computational meshes (G1, G2, and G3) were developed for the present case study and are summarized in terms of total cell count and near-hull spacing in Table 7.2. All the meshes were built with the native OpenFOAM® mesher, `snappyHexMesh`. Each of the structured domains are a square with a height and width of 370 m, which is roughly equivalent to $20B$. The only difference between the meshes

is the resolution throughout the domain that is characterized by the uniform spacing near hull. The G2 mesh in Figure 7.2 has a spacing 1 m near the hull and 2×1 (width and height) in the far field. The grading of the cell size was selected to ensure that as the domain rotates to large roll angles with the hull, the propagating wave is sufficiently resolved.

Table 7.2: Summary of mesh statistics for the 2-D ONRT midship section case study where H = 7.5 m and T=15 s.

Properties	G1	G2	G3
Width [m]	370	370	370
Height [m]	370	370	370
# of Cells (w/o Ship)	39,590	79,180	158,360
# of Cells (w/ Ship)	21,669	83,103	326,736
$\lambda/\Delta y$ (Uniform)	175	350	700
$H/\Delta z$ (Uniform)	3.5	7	14
$\lambda/\overline{\Delta y}$	101	202	404
$H/\overline{\Delta z}$	3.5	7	14

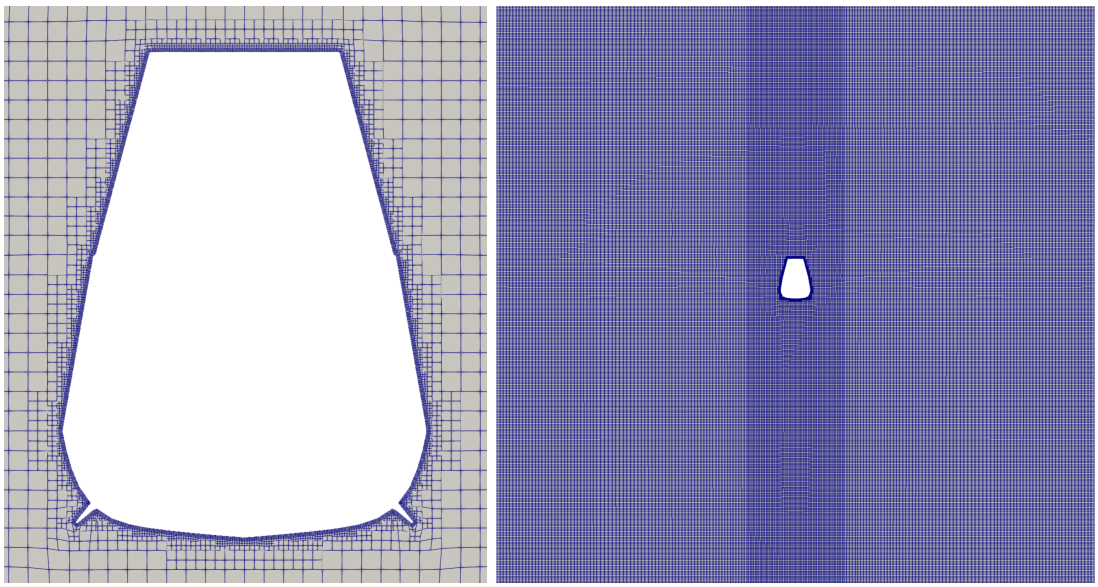

Figure 7.2: 2-D ONRT midship section case study computational mesh (G2).

A single composite wave train with a large embedded wave group was selected for a mesh refinement study. Figure 7.3 shows a comparison of the wave elevation at the

origin for the three mesh resolutions. The comparison of wave elevation in Figure 7.3 reflect computational meshes that only include the background mesh depicted in Figure 7.2, without the hull to investigate solely the wave propagation. Overall, the three meshes to able to produce wave elevations at the origin that resemble the analytical description of the wave. There is not a substantial difference between the three mesh resolutions.

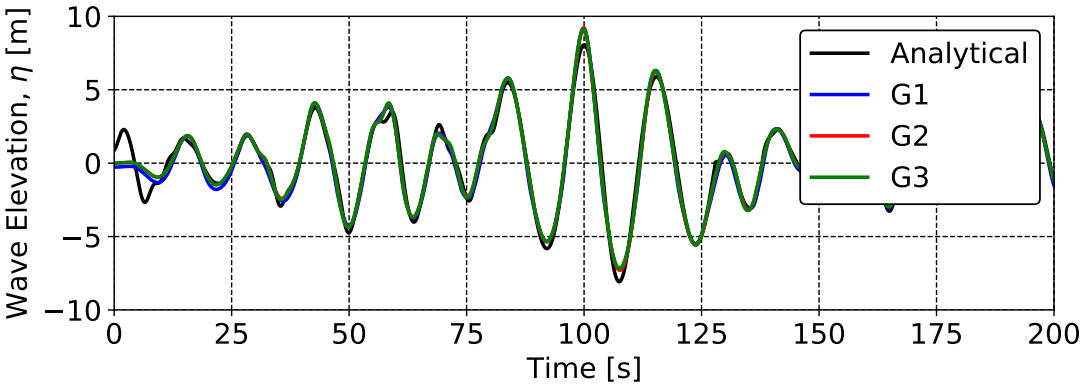

Figure 7.3: Mesh refinement evaluation (without the hull) of wave elevation at the origin for the 2-D ONRT midship section case study with a sample embedded wave group of $H_c = 16.875$ m, $T_c = 15$ s, and $j = 3$.

Figure 7.4 shows the heave and roll response predictions with the same wave train from Figure 7.3, but with the hull included in the mesh. Figure 7.4 elucidates some differences between the three different meshes for heave and roll. Overall, the phasing between the different meshes is consistent. However, the difference in magnitude of the roll during the largest event is distinct between G1 and either G2 or G3. The difference in the maximum roll is approximately 10 deg. The G2 and G3 meshes are in better agreement with each other and only differ by a maximum of 1-2 deg throughout the entire simulation.

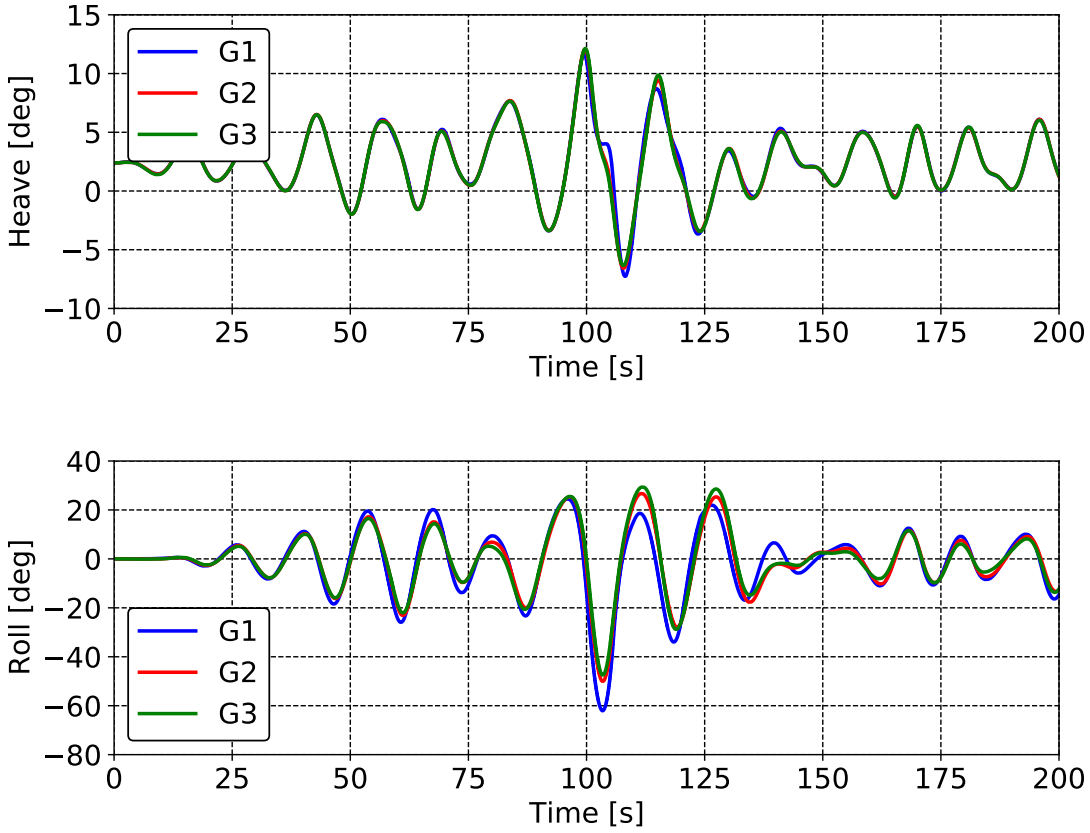

Figure 7.4: Mesh refinement evaluation of heave and roll for the 2-D ONRT midship section case study with a sample embedded wave group of $H_c = 16.875$ m, $T_c = 15$ s, and $j = 3$.

Table 7.3 summarizes the overall RMSE for both the wave propagation and motion mesh refinement cases. For the wave propagation case, the time-histories of wave elevation for each mesh are compared to the analytical wave elevation at the origin. Since there is no analytical solution for motion prediction, the RMSE for the G1 and G2 meshes is calculated with respect to the G3 mesh. Overall, both cases observe a decrease in RMSE as the mesh size increased. The evaluated cases provide confidence that the CFD setup is sufficient for demonstrating the different aspects of the CCS framework. Additionally, the results with the G2 mesh are comparable to predictions with the G3 mesh. Therefore, all simulations in the present case study are performed utilizing the G2 mesh to reduce the overall computational cost.

Table 7.3: Comparison of the RMSE for the various 2-D ONRT meshes.

Case	G1	G2	G3
Wave Probe Elevation [m]	1.4954	1.3860	1.3853
Heave [m]	0.4633	0.0962	-
Roll [deg]	5.1928	1.3998	-

7.2 Extreme Roll Response

The Sea State 7 JONSWAP spectrum is sampled to produce 100,000 hours of of random wave elevation observations at the origin. The 100,000 h of of random wave elevations consisted of 100,000 1 hours realizations with the superposition of 1000 Fourier components describing the wave field (see Equation 3.6). From the 100,000 hours, the successive wave relationships described in Section 2.2 are developed to construct the wave groups show in Figure 7.5. The current case study considered T_c of 13, 14, 15, 16, and 17 s, $j \leq 2$, and H_c of 9.375, 11.25, 13.125, 15, and 16.875, which corresponds to 5σ, 6σ, 7σ, 8σ, and 9σ respectively. In total, 10 T_c and j pairs are considered.

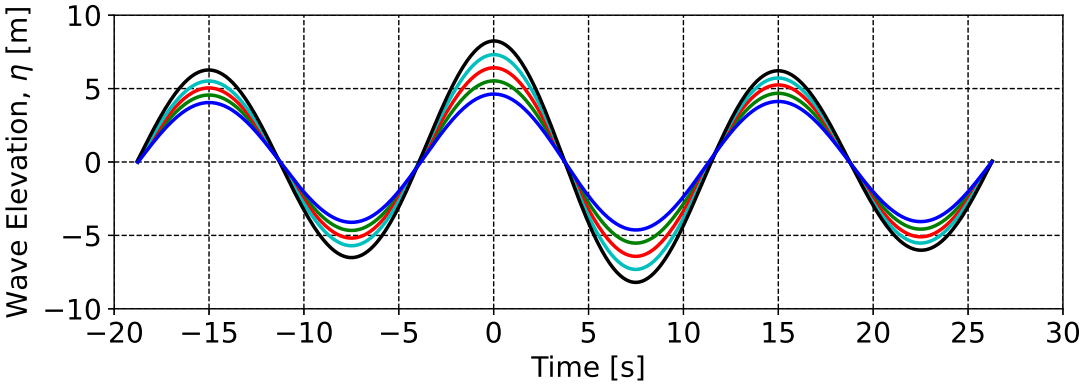

Figure 7.5: Ensemble of different wave groups with $\Delta T = 1$ s, $j = 3$, $T_c = 15$ s and $H_c = 5\sigma$, 6σ, 7σ, 8σ, and 9σ for the 2-D ONRT midship section case study.

Five six-minute (0.5 hours total) CFD simulations are also performed in the random waves for the 2-D ONRT to develop the probability of encounter conditions, and identify

wave trains that lead to the encounter conditions of interest (irregular preludes). Figure 7.6 showcases both the random wave observation and the corresponding joint probability of encounter condition for roll angle and roll velocity developed through Kernel Density Estimation (KDE) with the random wave ship response observations. Figure 7.6b also denotes with black circles, the selection of encounter conditions.

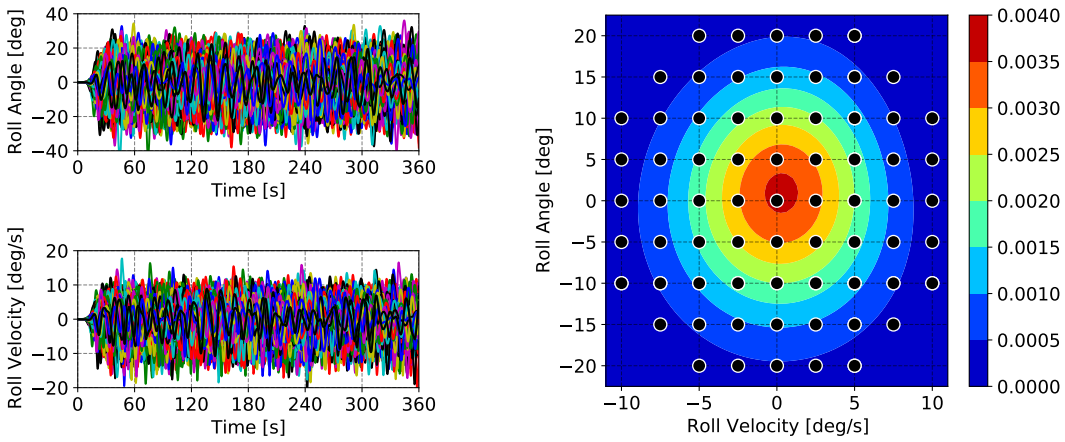

(a) Random Wave Observations

(b) Probability

Figure 7.6: Observation and probability distribution of encounter conditions for the 2-D ONRT midship section case study.

This case study considers both a general and an ensemble approach to train the neural network surrogate models. The *general* approach trains a single neural network model with randomly selected composite wave trains. The *ensemble* approach utilizes several models, each responsible for composite wave trains with a specified period of the largest wave T_c and run length j. Both modeling approaches are explored because although the general approach allows for more training runs per model compared to an ensemble approach in terms of total training runs required, it must predict the dynamics over a larger parameter range. The ensemble model approach only considers wave groups within a smaller subset of the total parameter range. Therefore, the ensemble model approach only has to differentiate between the height of the largest wave in the group and the various encounter conditions, which can enhance accuracy

and produce faster convergence with respect to training data quantity.

The training matrix, neural network architecture, and hyper-parameters for the case study are presented in Table 7.4. The CCS framework is evaluated with training datasets of 50, 100, 200, or 400 training runs for both the ensemble and general neural network modeling approaches. The training dataset is identical between the general and ensemble modeling approaches, and the smaller sized training datasets are a subset of the larger training runs. For example, the models with 100 total training runs utilize the same 50 runs as the models trained with only 50 training runs. For each total quantity level of training data, the runs are segregated equally across the 10 T_c and j pairs. For each T_c and j pair, training runs are selected randomly in terms of H_c and the encounter conditions. For the ensemble approach, a separate model is constructed for each of the T_c and j pairs. The general approach uses all of the training data as the ensemble model approach, but only builds a single model. For example, the ensemble model approach for 400 total training runs contains 40 runs for each of the 10 T_c and j, while the general approach would train off the same 400 runs. The same is true for other training dataset sizes. This consistency ensures that both modeling approaches have the same information available to remove bias in the training. In accordance with the case study in Section 5.3, 27 wave probes around the hull are utilized in the construction of the neural network.

Each model utilizes the same architecture and training methodology and is evaluated against 25,100 validation runs, which corresponds to all of CFD simulations required to calculate the probability of exceedance, purely considering CFD without any surrogate modeling. Every model is evaluated in terms of the L_2 (formulated as the root mean squared error) and L_∞ error, described in Equations 5.14 and 5.15, respectively, for each individual validation run.

Figures 7.7 and 7.8 compare the L_2 and L_∞ error, respectively, for heave and roll, employing both the ensemble and general approaches with various quantities of

Table 7.4: Training matrix, neural network architecture, and hyper-parameters for the case study.

Properties	Value
Total Training Runs	50, 100, 200, 400
Training Runs per Model (Ensemble)	5, 10, 20, 40
Total Validation Runs	25,100
Time Steps per Run	200
Units per Layer	50
Layers	2
Dropout	0.1
Learning Rate	0.001
Epochs	2,000
Optimizer	Adam (*Kingma and Ba*, 2014)

training data. The error calculation in Equations 5.14 and 5.15 are performed for each of the validation runs. The triangle and rectangle markers in Figures 7.7 and 7.8 correspond to the median error across all validation runs, while the error bars denote the 25$^{\text{th}}$ and 75$^{\text{th}}$ percentiles. For both the general and ensemble approaches, the L_2 and L_∞ error for heave and roll decreases as the quantity of training data increases. Additionally, the size of the error bars for the L_2 and L_∞ error decreases as the quantity of training data increases. Overall, the general approach provides better predictions for heave, but the roll predictions are similar between the two modeling approaches.

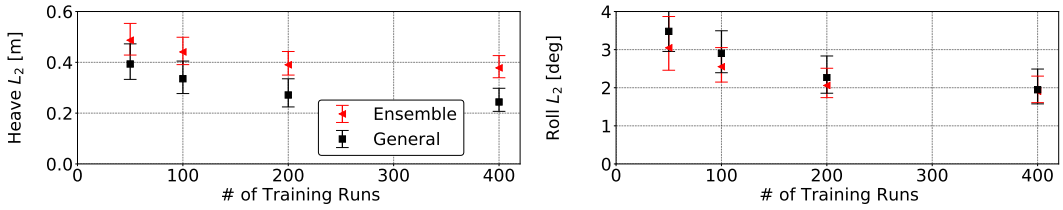

Figure 7.7: Comparison of L_2 error for heave and roll for the 2-D ONRT midship section case study.

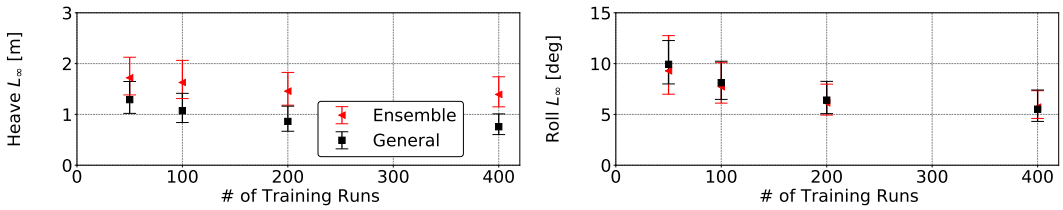

Figure 7.8: Comparison of L_∞ error for heave and roll for the 2-D ONRT midship section case study.

Figures 7.7 and 7.8 show the overall performance and accuracy of the neural network in terms of L_2 and L_∞, but do not show the actual temporal LSTM prediction error. Figures 7.9 and 7.10 demonstrate the three validation runs that resulted in the smallest L_∞ and L_2 error, respectively, for heave and roll for the general approach model trained with 400 runs. CFD is compared in Figures 7.9 and 7.10 to the LSTM predictions with uncertainty estimates from the Monte Carlo Dropout approach that corresponds to two standard deviations. The LSTM predictions are able to match both the phasing and magnitude of the CFD predictions well. Figures 7.11 and 7.12 showcase the three validation runs with the largest L_∞ and L_2 error, respectively. For both heave and roll, portions of the LSTM predictions match the CFD well, while other parts of the time-history are not predicted as accurately, especially after significant response magnitudes. Overall, the uncertainty is on the order of 1-2 deg for the largest roll angles and is typically larger at the response peaks.

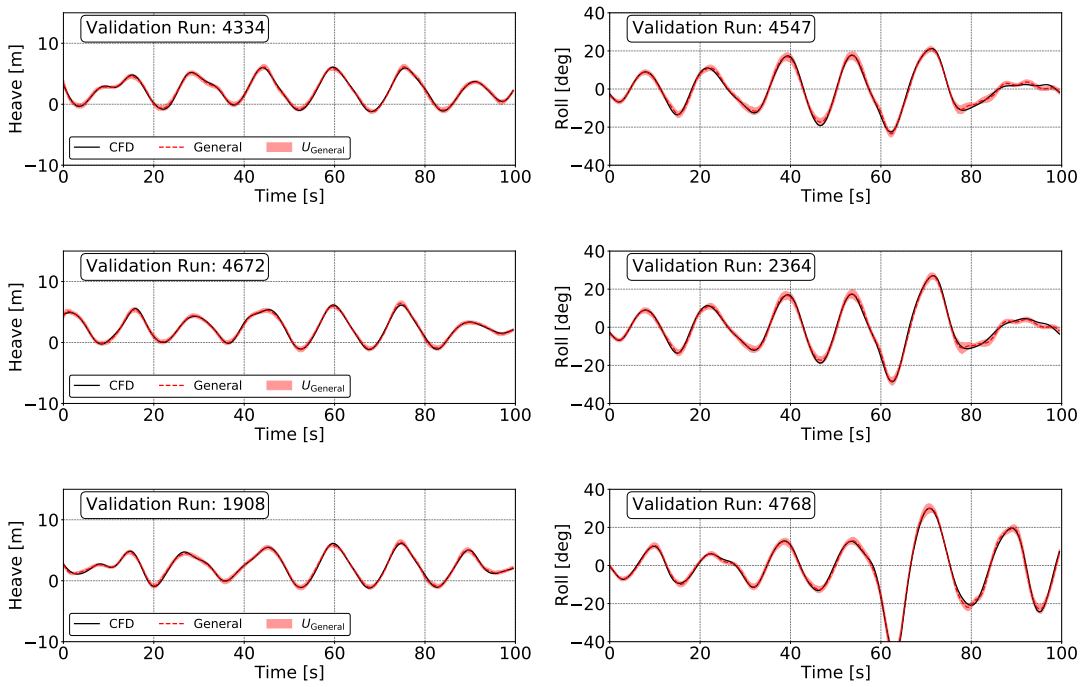

Figure 7.9: Three observations with the smallest L_∞ error for each DoF using a model trained with 400 simulations for the 2-D ONRT midship section case study.

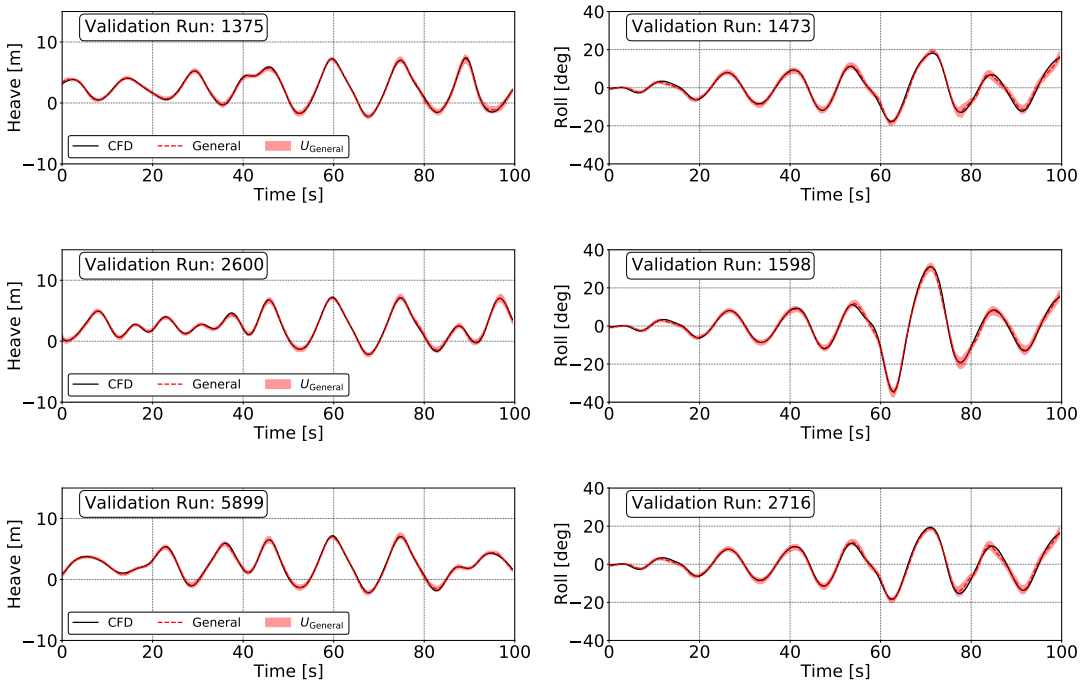

Figure 7.10: Three observations with the smallest L_2 error for each DoF using a model trained with 400 simulations for the 2-D ONRT midship section case study.

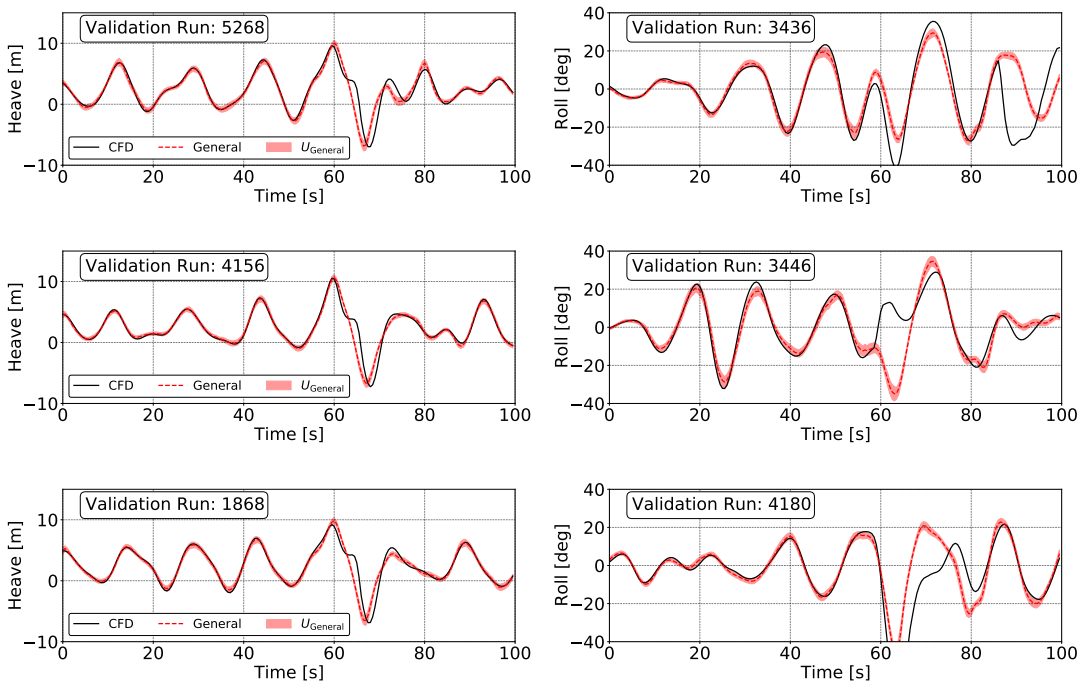

Figure 7.11: Three observations with the largest L_∞ error for each DoF using a model trained with 400 simulations for the 2-D ONRT midship section case study.

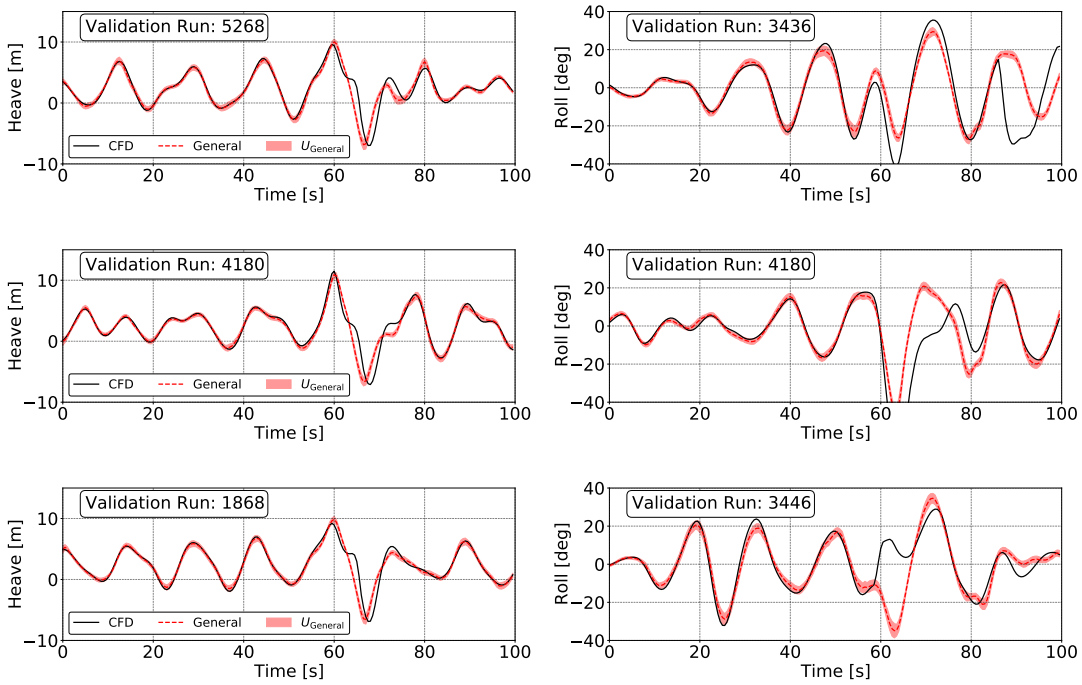

Figure 7.12: Three observations with the largest L_2 error for each DoF using a model trained with 400 simulations for the 2-D ONRT midship section case study.

Figures 7.7 through 7.11 provide overall assessments on the accuracy of the LSTM models to reproduce the temporal response of the CFD simulations. However, the CWG methodology is concerned with the extremes, and therefore, the absolute maximums are of greater importance than the temporal predictions. The CFD and LSTM predictions of the maximum heave and roll due to each composite wave train are compared in Figures 7.13 and 7.14, respectively, for the ensemble and general approaches.

Each marker in Figures 7.13 and 7.14 for a particular model corresponds to a single composite wave train and the corresponding CFD and LSTM predictions. The solid black line denotes identical values for CFD and LSTM. Similar to the comparisons of L_∞, the 400 training run models have similar trends, while there seems to be more spread in the data for models trained with less data. Both approaches demonstrate convergence towards better correlation. There is much more spread in the absolute maximum predictions of roll than heave. Overall, the LSTM neural networks are much more accurate in representing heave than roll.

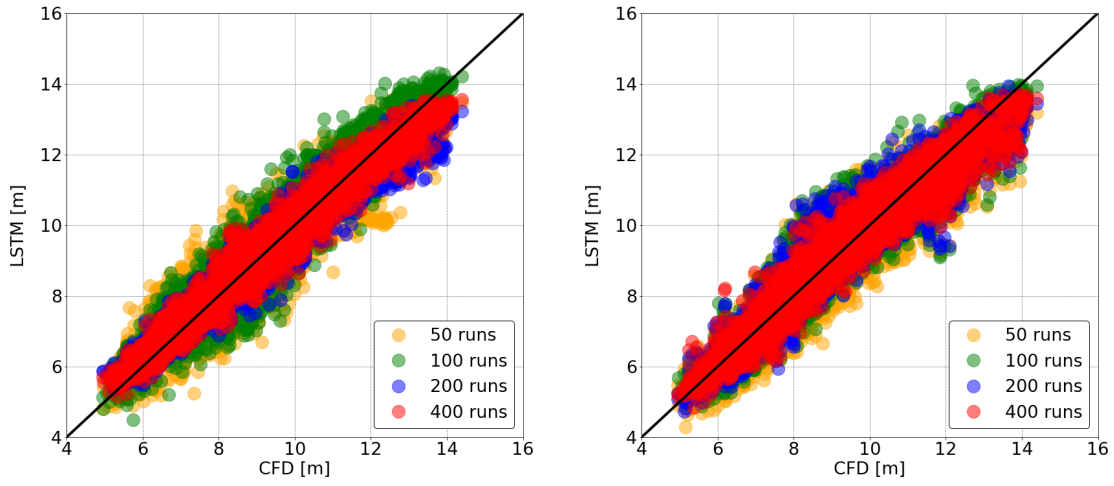

(a) Ensemble (b) General

Figure 7.13: CFD and LSTM predictions of the absolute maximum heave for all the composite wave trains for the 2-D ONRT midship section case study.

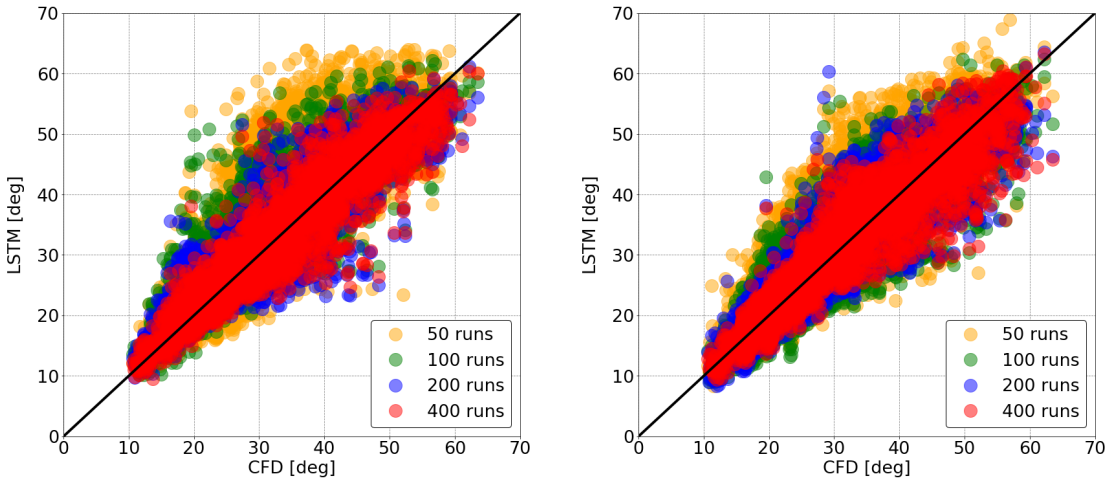

(a) Ensemble (b) General

Figure 7.14: CFD and LSTM predictions of the absolute maximum roll for all the composite wave trains for the 2-D ONRT midship section case study.

Figure 7.15 compares the probability of exceedance results of both modeling approaches with various amounts of training data, predictions that combine CWG and CFD without surrogate models (CC), and Monte Carlo results from 100 hours of exposure time. With 200 training runs, both approaches are able to represent results produced without surrogate modeling utilizing, only CFD. When less training data is available, the general model is more accurate. However, with at least 200 training runs available both are able to reproduce the CWG-CFD prediction of probability of exceedance.

Figure 7.15c compares the uncertainty in the LSTM predictions with both approaches for 400 total training runs. The uncertainty for both approaches increases as the roll angle of interest increases. Although the uncertainty is low in the time-history predictions in Figures 7.7 through 7.11, it compounds across all the considered composite wave trains. The compounding of uncertainty and the sensitivity of the probability of exceedance calculation yields uncertainty in the probability calculation that is of the same order of magnitude as the probability itself at the largest roll angles. The large uncertainty highlights that as a response of interest becomes more

extreme and rare, the probability calculation is detrimentally sensitive to underlying LSTM error.

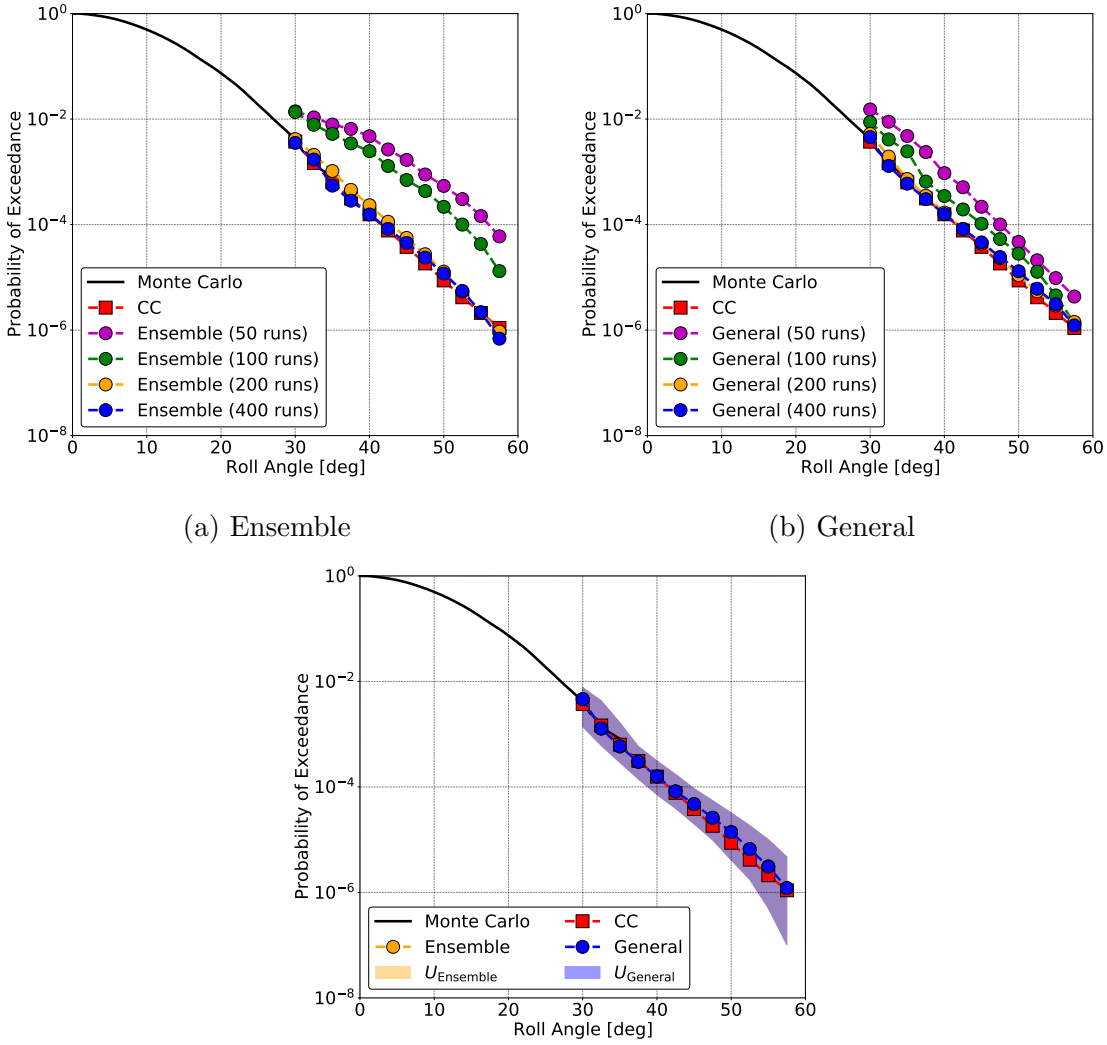

(a) Ensemble

(b) General

(c) With Uncertainty

Figure 7.15: Probability of exceedance of roll in Sea State 7 for the 2-D ONRT midship section case study.

The CWG method is a systematic methodology that attempts to reduce the total computational cost of extreme event event evaluations with respect to a Monte Carlo approach. However, the introduction of the natural initial conditions make the events produced by the CWG method physically realizable and the utilization of high-fidelity and costly CFD increases the cost per observed event. The total CPU and exposure

time of the CWG-CFD and CCS methods are shown in Figure 7.16 and compared with the required simulation time for Monte Carlo analysis estimated with Equation 7.1 from *Ochi* (1998). In Equation 7.1, $\overline{y_n}$ is the most probable maximum response, T is the exposure time in hours, m_0 and m_1 are the zeroth and second spectral moments of the response, respectively.

$$\overline{y_n} = \sqrt{m_0}\left[2\ln\left(\frac{60^2 T}{2\pi}\sqrt{\frac{m_2}{m_0}}\right)\right]^{\frac{1}{2}} \tag{7.1}$$

The CPU time corresponds to the total computational cost of the methodologies and is specific to the considered mesh, software, and computing system. Meanwhile, the exposure time is the actual response time simulated, which is consistent across systems and would be applicable to model testing and a 3-D ship as well. The CPU and exposure time required of the CWG implementations also includes the random wave simulations considered in the identification of the irregular preludes and the associated probability distribution of the encounter conditions. The CWG-CFD methodology, as shown in Figure 7.16, reduces the computational cost over Monte-Carlo simulation for the same case study by roughly five orders of magnitude at a roll angle of 57.5 deg. The CCS model utilizing 400 training runs results in two orders of magnitude reduction in the total computational cost of the CWG-CFD approach. Thus, the CCS methodology results in a total estimated reduction of seven orders of magnitude in computational cost to produce a probability of exceedance of up to a threshold of 57.5 deg. The cost of the CCS methods is close to that of the Monte Carlo for producing probability of exceedance predictions up to a roll angle of 30 deg.

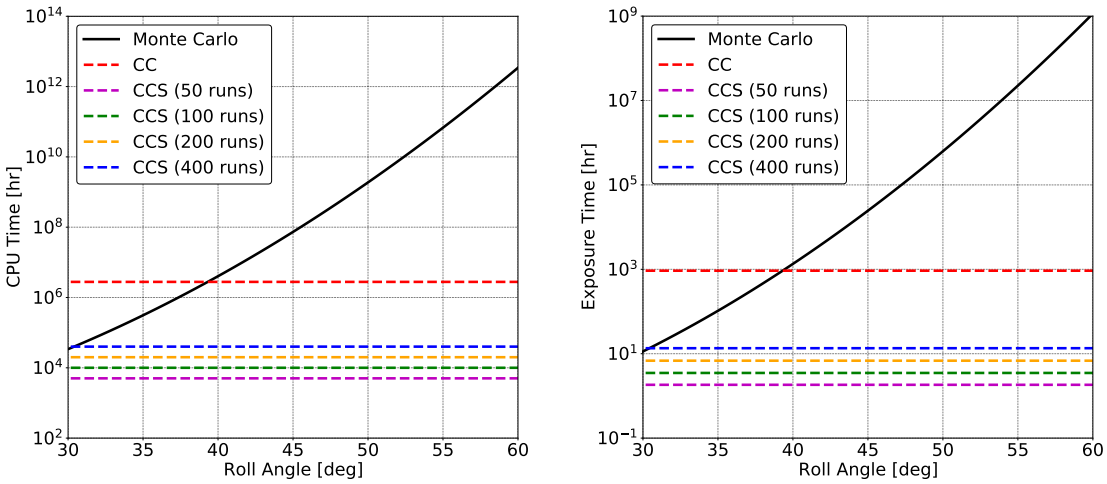

(a) CPU Time

(b) Exposure Time

Figure 7.16: Required CPU and exposure time for the Monte Carlo, CC, and CCS methods for the 2-D ONRT midship section case study.

This case study constitutes significant progress, not only in the development of a computationally efficient framework for extreme ship response quantification, but also demonstrates a means of training neural networks to produce real-time observations of extremes. Previous research training neural networks to represent the dynamical response of vessels has focused on random waves and has not explored the application to extremes. Neural networks, in general, are better at interpolation than extrapolation and are thought to perform poorly in predicting extreme events when trained with random data. However, the present neural nets are trained with composite wave trains that contain large and rare deterministic wave groups that lead to extremes. Therefore, the 400 composite wave trains can be used, in principle, to train robust neural network surrogate models capable of performing Monte Carlo analysis that recover the entire PDF of each DoF and not simply the probability of exceedance that is calculated within the CWG method. Figure 7.17 compares CFD and LSTM predictions of heave and roll PDF in logarithmic scale utilizing only the general modeling approach for 100 hours of exposure time in random irregular waves. The roll and negative portion of the heave are well represented, but the positive heave is under-predicted. Similar

to the probability of exceedance comparisons, the PDF converges around 200 training runs. Although the LSTM models perform well and recovers the underlying PDF, the presented CFD results only consider a 100 hour exposure window, which is not enough to induce significant extremes. The exposure time projections in Equation 7.1 and shown in Figure 7.16 predict a most probable maximum of 35 deg with a 100 hour exposure window, which qualitatively agrees with the absolute maximum roll angles observed in Figure 7.17 even though the models were trained with the composite wave trains rather than random irregular waves. To achieve the larger roll angles in Figure 7.15, significantly more exposure time is required. Therefore, although the prediction of the PDF with the LSTM neural networks is encouraging, further research is needed to evaluate whether CCS training methodology is suitable for recovering the entire extreme PDF through a Monte Carlo prediction with am LSTM neural network.

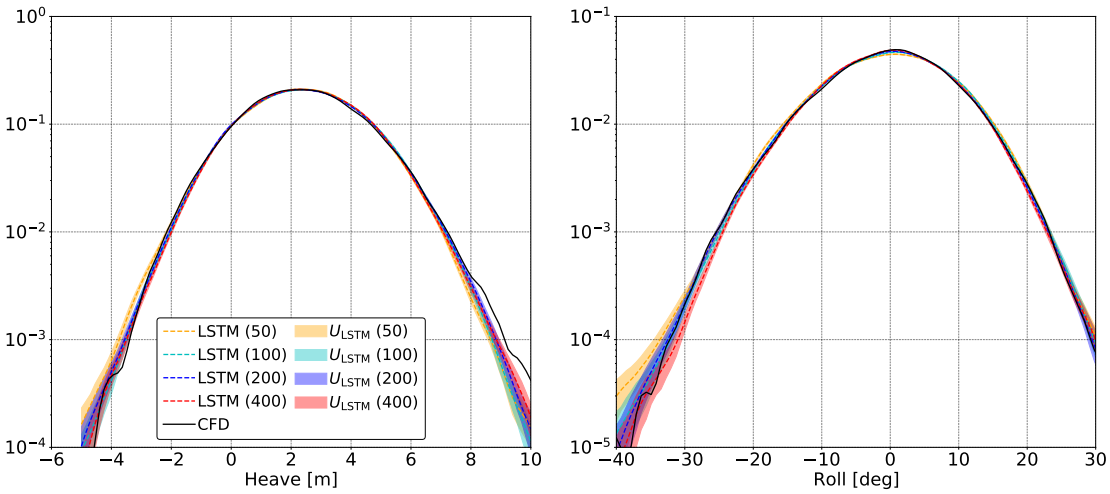

Figure 7.17: Comparison of the PDF in a logarithmic scale for each DoF with models trained with the general approach for the 2-D ONRT midship section case study.

CHAPTER VIII

Case Study: 3-D 6-DoF ONR Tumblehome

This chapter presents a case study demonstrating the CCS framework with a 3-D free-running model-scale ONRT hull in stern-quartering Sea State 7 seas. The vessel is self-propelled and maintains heading by utilizing the propeller and rudder model described in Section 3.3 with a PID-controlled rudder model. The rudder model employed in this case study follows the research of *Araki et al.* (2012), using a wake fraction w of 0 and a straightening coefficient γ of 0.7. The propeller model was developed with a propeller revolution rate $n = 8.97$ rps, and the propeller diameter $D = 0.1066$ m. Table 8.1 shows the particulars and loading condition for the ONRT, as well as the fluid properties utilized in the CFD simulations. The length between perpendiculars L_{pp}, longitudinal center of gravity LCG, vertical center of gravity VCG, and the transverse metacentric height GMT, all reflect model-scale parameters from *Larsson et al.* (2015). However, the gyradii are adjusted to match ongoing work with North Atlantic Treaty Organization Applied Vehicle Technology (NATO AVT-348) activity *Assessment of Experiments and Prediction Methods for Naval Ships Maneuvering in Waves*.

Three different meshes developed utilizing the `snappyHexMesh` meshing tool (G1, G2, and G3) are considered in the present case study and are summarized in Table 8.2. The different meshes employ the same domain extents and are refined by a factor

of $\sqrt{2}$ in each direction to result in mesh sizes of 1.57, 4.07, and 10.95 million cells with the ship for the G1, G2, and G3 meshes, respectively. The G1 mesh is primarily utilized in the extreme event portion of the case study, while the G2 and G3 meshes were used in a small grid sensitivity study to asses the accuracy of the G1 mesh.

Table 8.1: Loading condition and fluid properties of 3-D ONRT midship section.

Properties	Units	Value
Length Between Perpendiculars, L_{pp}	m	3.147
Beam, B	m	0.384
Draft, T	m	0.112
Displacement, ∇	kg	72.6
Longitudinal Center of Gravity, LCG (+Fwd of AP)	m	1.625
Vertical Center of Gravity, KG (Above Baseline)	m	0.156
Transverse Metacentric Height, GMT	m	0.0422
Roll Gyradius, k_{xx}	m	0.1448
Pitch Gyradius, k_{yy}	m	0.7742
Yaw Gyradius, k_{zz}	m	0.7742
Density of Water, ρ_w	kg/m^3	998.72
Density of Air, ρ_a	kg/m^3	1
Kinematic Visc. of Water, ν_w	m^2/s	1.0703e-6
Kinematic Visc. of Air, ν_a	m^2/s	1.48e-5
Accel. due to Gravity, g	m/s^2	9.80665

Figures 8.1 and 8.2 show the G1 mesh for the hull surface and computational domain. Since the CFD simulations utilize a propeller and rudder model, the developed surface mesh neglects both the propeller and rudder geometries. Instead, a body force is added to the fluid solution uniformly for the group of cells encompassing their respective locations in the mesh. The computational domain contains a structured background mesh with dimensions $(3.5 \times 3.5 \times 2.5)L_{pp}$. The length and width are set as equal to aid with the quartering wave generation. The meshes contain a uniform inner region around the hull, while the rest of the domain is graded from the uniform region to the boundaries of the domain. Spacing details of the mesh cells are provided in Table 8.2 for a regular wave with height, $H = 0.1430$ m and period, T=1.6868 s,

where λ corresponds to the wavelength of the wave, Δx, Δy, and Δz correspond to the cell size in the uniform region closest to the hull, while $\overline{\Delta x}$, $\overline{\Delta y}$, and $\overline{\Delta z}$ correspond to the average spacing for the entire mesh.

Table 8.2: Summary of mesh statistics for the 3-D ONRT case study where H = 0.143 m and T=1.6868 s.

Properties	G1	G2	G3
Length [m]	11.0145	11.0145	11.0145
Width [m]	11.0145	11.0145	11.0145
Height [m]	7.8675	7.8675	7.8675
# of Cells (w/o Ship)	1.31 mil	3.71 mil	10.42 mil
# of Cells (w/ Ship)	1.57 mil	4.07 mil	10.95 mil
$\lambda/\Delta x$ (Uniform)	248	351	496
$\lambda/\Delta y$ (Uniform)	248	351	496
$H/\Delta z$ (Uniform)	4.94	6.99	9.88
$\lambda/\overline{\Delta x}$	115	162	229
$\lambda/\overline{\Delta y}$	65	93	130
$H/\overline{\Delta z}$	1.35	1.91	2.69

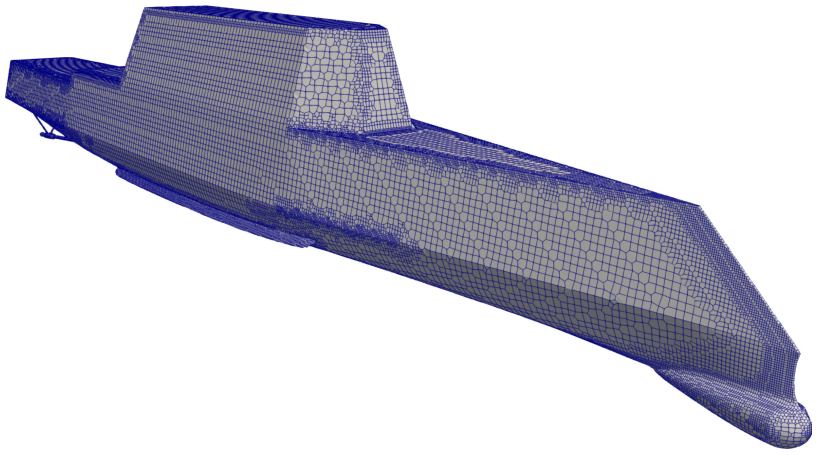

Figure 8.1: Surface mesh of the 3-D ONRT hull for the G1 mesh.

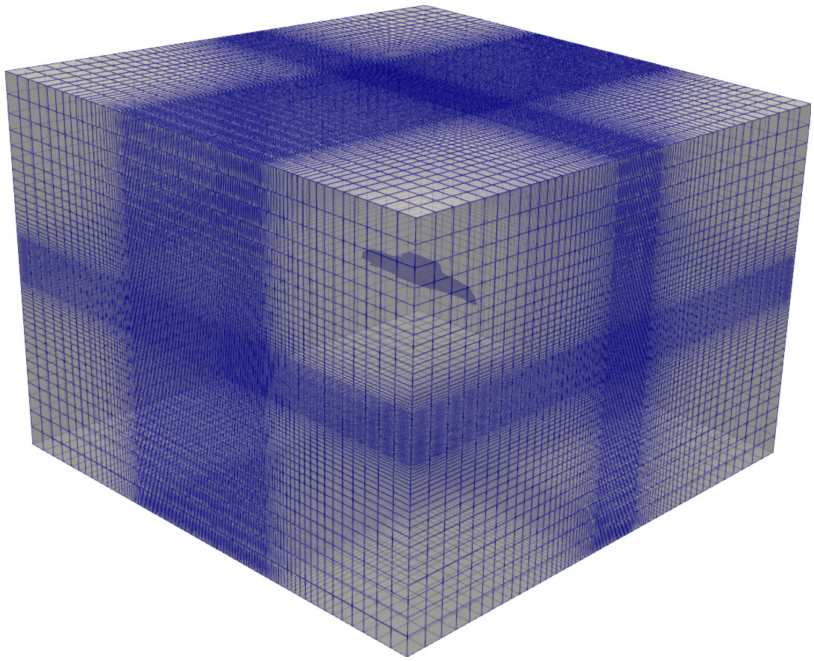

Figure 8.2: G1 Computational domain utilized for the 3-D ONRT CFD simulations.

8.1 Mesh Sensitivity

To confirm the meshes are adequate for the present case study, a grid sensitivity study is performed for both a regular wave propagation and a 6-DoF ship motion in irregular waves case. The regular wave case utilizes a mesh without the ship, and focuses on evaluating whether the grid refinement is sufficient to simulate a stern-quartering regular wave with height $H = 0.143$ m and period $T = 2.1443$ s. Figure 8.3 shows a comparison between the analytical wave solution and the predicted wave elevation at three wave probes distributed diagonally across the domain in the direction of the waves. The longitudinal and lateral location pairs of the probes in meters are (-3,-3), (0,0), and (3,3), ranging from the most upstream probe (Probe 1), to the most downstream probe (Probe 3). The comparison between the analytical solution and the CFD predictions in Figure 8.3 are demonstrated with a non-dimensional time t/T and wave amplitude η/A, where A is the nominal wave amplitude. After the initial growth of the waves over the first several periods, the predicted waves are nearly identical to

the analytical solution for all the observed probes. The close agreement between CFD and the analytical wave observed in Figure 8.3 indicates that all the developed grids have sufficient resolution to propagate waves throughout the domain.

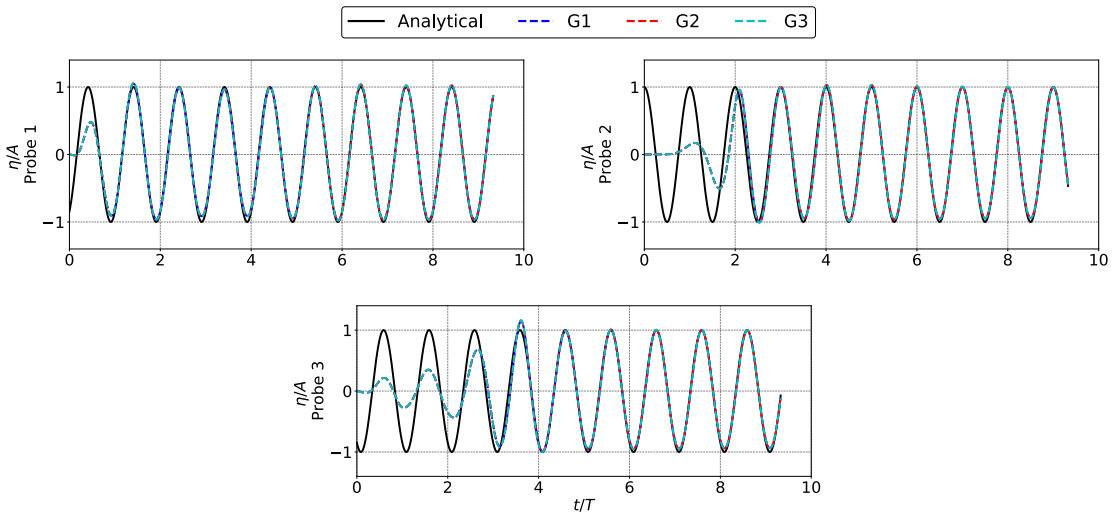

Figure 8.3: Comparison of different 3-D ONRT grid refinements for a regular wave with $H = 0.143$ m and $T = 2.1443$ s.

The other considered case was simulating the 6-DoF response of a free-running ONRT for a composite wave train with an embedded wave group $H_c = 0.3218$, $T_c = 2.4302$ s, and $j = 3$. The free-running ONRT is self-propelled with a propeller model, and its heading is controlled with a PID-controller and a rudder model. Comparisons of the surge velocity, sway velocity, heave, roll, pitch, and yaw are shown in Figure 8.4 for the G1, G2, and G3 meshes. Overall, the different meshes demonstrate little difference between the mesh refinements with the exception of surge velocity and yaw, where the G1 grid deviates from the G2 and G3 grid for a short period of time. The discretization error is the cause for this deviation. Although the yaw responses revealed differences between the mesh refinements, the variation in other DoF is negligible and the G1, G2, and G3 predictions of the wave-body interaction are comparable.

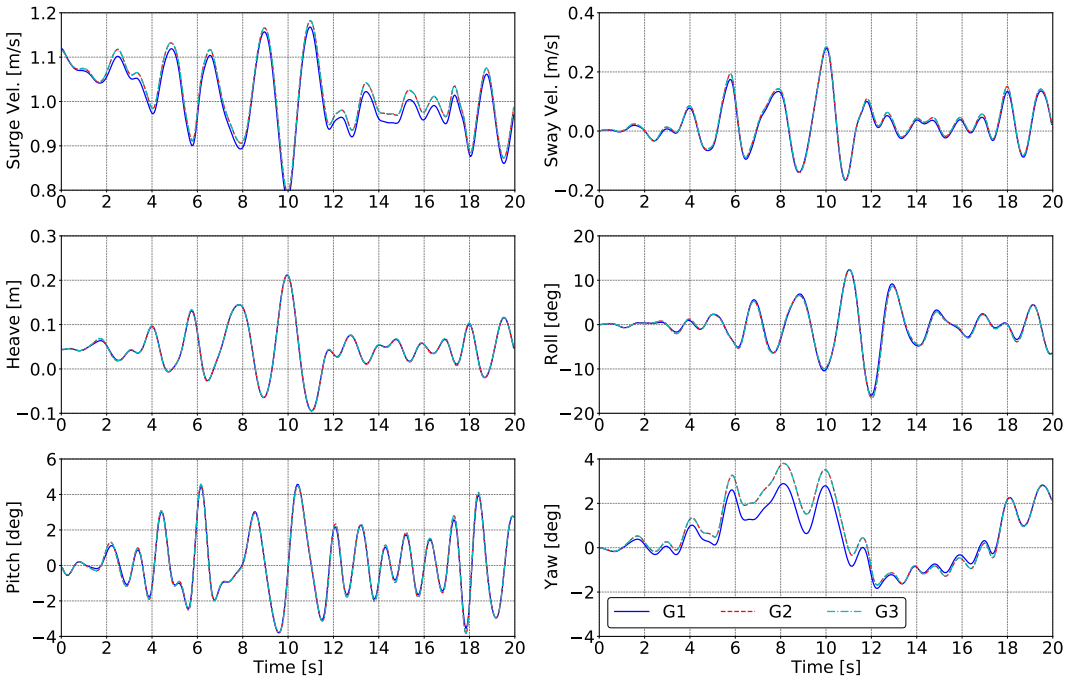

Figure 8.4: Comparison of the different 3-D ONRT grid refinements for ship response due to a sample composite wave train with an embedded wave group of $H_c = 0.3218$, $T_c = 2.4302$ s, and $j = 3$.

Table 8.3 summarizes the overall RMSE for both the wave propagation and 6-DoF motion case. For the wave propagation case, the time-histories of wave elevation for each mesh are compared to the analytical wave elevation at each probe for $t/T \geq 5$. Since there is not an analytical solution for 6-DoF motion case, the RMSE for the G1 and G2 meshes is calculated with respect to the G3 mesh. Overall, both cases observe a decrease in RMSE as the mesh size increased. The selected wave propagation and 6-DoF motion cases demonstrate that the mesh and CFD simulation setup can propagate waves throughout the domain, and also resolve the hydrodynamic forces acting on the body. The evaluated cases provide confidence that the CFD setup is sufficient for showcasing the different aspects of the 6-DoF implementation of the CCS framework. Additionally, the results with the G1 mesh are comparable to predictions with the G2 and G3 meshes. Therefore, all simulations for the CCS 6-DoF framework are performed utilizing only the G1 mesh to reduce the overall computational cost.

Table 8.3: Comparison of the RMSE for the different 3-D ONRT meshes.

Case	G1	G2	G3
Wave Probe #1 [-]	2.310e-2	2.303e-2	2.296e-2
Wave Probe #2 [-]	2.909e-2	2.752e-2	2.671e-2
Wave Probe #3 [-]	3.252e-2	3.139e-2	3.022e-2
Surge Vel. [m/s]	1.374e-2	6.640e-4	-
Sway Vel. [m/s]	6.924e-3	7.193e-4	-
Heave [m]	1.480e-3	5.533e-4	-
Roll [deg]	3.677e-1	5.810e-3	-
Pitch [deg]	1.041e-1	5.672e-3	-
Yaw [deg]	4.437e-1	5.533e-3	-

8.2 Extreme Roll Response

The CCS method is implemented for a free-running model-scale ONRT hull in Sea State 7 with the operating and seaway conditions defined in Table 8.4, where the response of interest is the roll angle. This case study considers a Froude number of 0.2, which corresponds to a speed of 1.111 m/s at model-scale. The ship is free in all DoF and is propelled with a propeller model. The heading is controlled with a rudder model as well as a PID-controller that employs the gains detailed in Table 8.4.

The selected seaway utilizes the stern-quartering seas defined by the JONSWAP spectrum outlined in *Hasselmann et al.* (1973) with a significant wave height H_s of 0.1839 m, a peak modal period T_p of 1.6868 s, and a peak enhancement factor γ of 3.3. 14,286 hours ($\tilde{1}$00,000 hours at full-scale) of random irregular wave data are produced by sampling the spectrum to yield the successive wave relationships required to construct deterministic wave groups with the Markov chain methodology. All of the wave groups constructed in the presented case study are for a T_c of 1.4009, 1.5439, 1.6868, 1.8298, and 1.9727 s and $j \leq 2$.

Thirteen random irregular wave CFD simulations of 20 s in length (260 s total at model-scale and 30 min total at full-scale) are performed for the free-running ONRT hull to develop the PDF shown in Figure 8.5 for roll and roll velocity utilizing KDE.

Table 8.4: Operating and seaway conditions for the 3-D ONRT case study.

Properties	Units	Value
Froude number, F_n	-	0.2
Speed	m/s	1.111
Wave Heading	deg	60 (Stern Quartering)
Sea State	-	7
Spectrum	-	JONSWAP
Significant Wave Height, H_s	m	0.1839
Peak Modal Period, T_p	s	2.1433
Peak Enhancement Factor	-	3.3
Proportional Gain, G_p	deg/deg	4
Integral Gain, G_i	1/s	0
Differential Gain, G_d	deg/(deg/s)	1
Max Rudder Angle, $\delta_{\max}$	deg	35
Max Rudder Rate, $\dot{\delta}_{\max}$	deg/s	35

The roll and roll velocity in random irregular waves demonstrates that the largest roll angles observed within the random irregular wave runs were approximately 40 deg in magnitude. The encounter conditions selected for the CWG method are denoted by black circles in Figure 8.5 and span the non-zero portion of the joint PDF. Each of the 13 random wave simulations are scanned between 8 and 14 s for response values that best match the encounter condition to develop the irregular preludes required for the natural initial condition. The time interval between 8 and 14 s is chosen to ensure that the waves and motions have sufficiently developed from rest, and the simulations with the embedded wave groups would not be longer than 20 s. Once the irregular preludes are identified, a series of composite wave trains are constructed for each wave group and encounter condition.

Table 8.5 shows a summary of the training and validation data, the neural network architecture, and the training parameters. For the present study, 500 of the constructed composite wave trains are randomly selected for the neural network construction and evaluation. 400 of the 500 chosen composite wave trains are used for training a variety of models with different quantities of training data to observe convergence. The other

100 composite wave trains are selected as validation runs for each model. Both the training and validation runs are spread across the 10 T_c and j pairs corresponding to 40 training and 10 validation composite wave trains for each pair. In accordance with the case study in Section 5.3, 27 wave probes around the hull are utilized in the construction of the neural network.

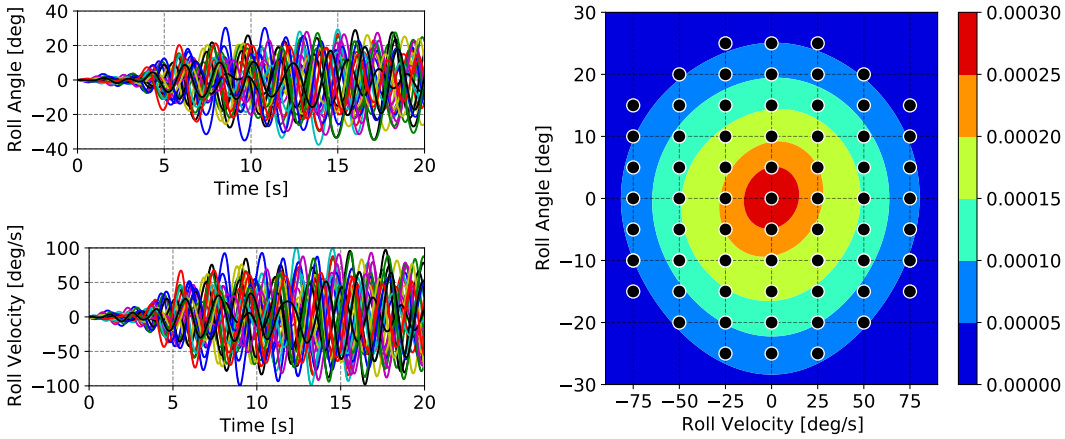

(a) Random Wave Observations

(b) Probability

Figure 8.5: Observation and probability distribution of encounter conditions for the 3-D ONRT case study.

Table 8.5: Training matrix, neural network architecture, and hyper-parameters for the 3-D ONRT case study.

Properties	Value
Total Training Runs	50, 100, 200, 400
Total Validation Runs	100
Time Steps per Run	400
Units per Layer	250
Layers	3
Dropout	0.1
Learning Rate	0.0001
Epochs	2,000
Optimizer	Adam (*Kingma and Ba*, 2014)

Four different neural network models are built with training data quantities of 50, 100, 200, and 400 simulations of composite wave trains. Each model employs the same

architecture and training methodology and is compared against the 100 validation runs for both the L_2 (formulated as the root mean squared error) and L_∞ error described in Equations 5.14 and 5.15, respectively. Only the general approach is considered in this case study. Therefore, only one model is built for all T_c and j at a particular training data quantity. Figures 8.6 and 8.7 show the L_2 and L_∞ error, respectively, for each DoF and different training data quantities. Each square represents the median error across all validation runs, while the error bars correspond to the 25% and 75% quantiles.

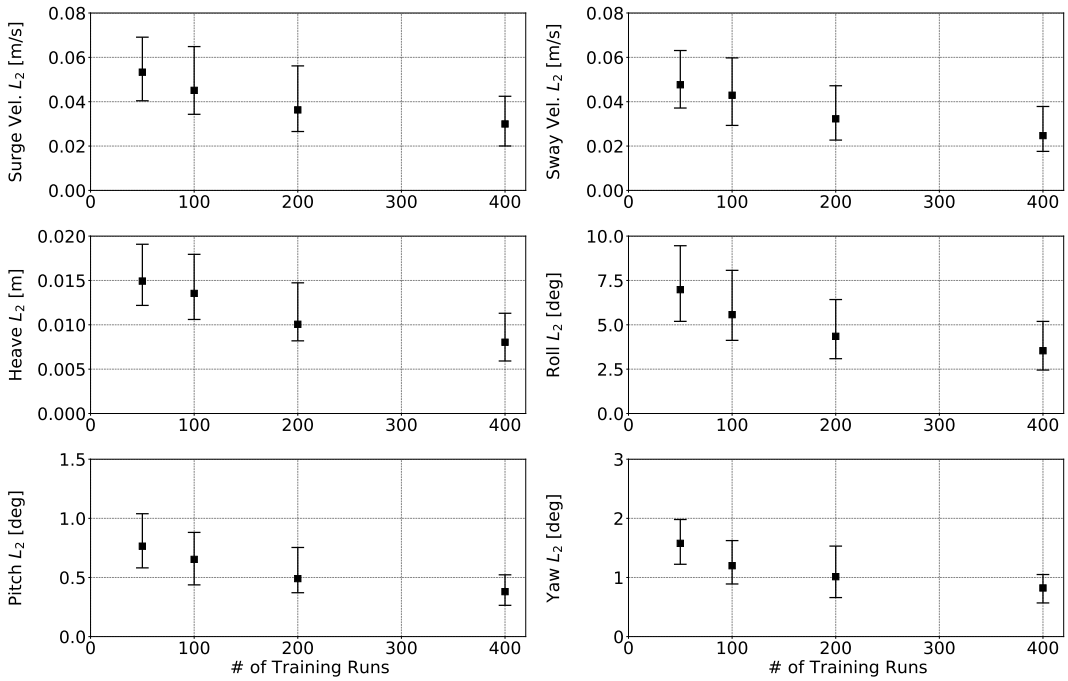

Figure 8.6: Convergence of neural network models with respect to training data for L_2 error for the 3-D ONRT case study.

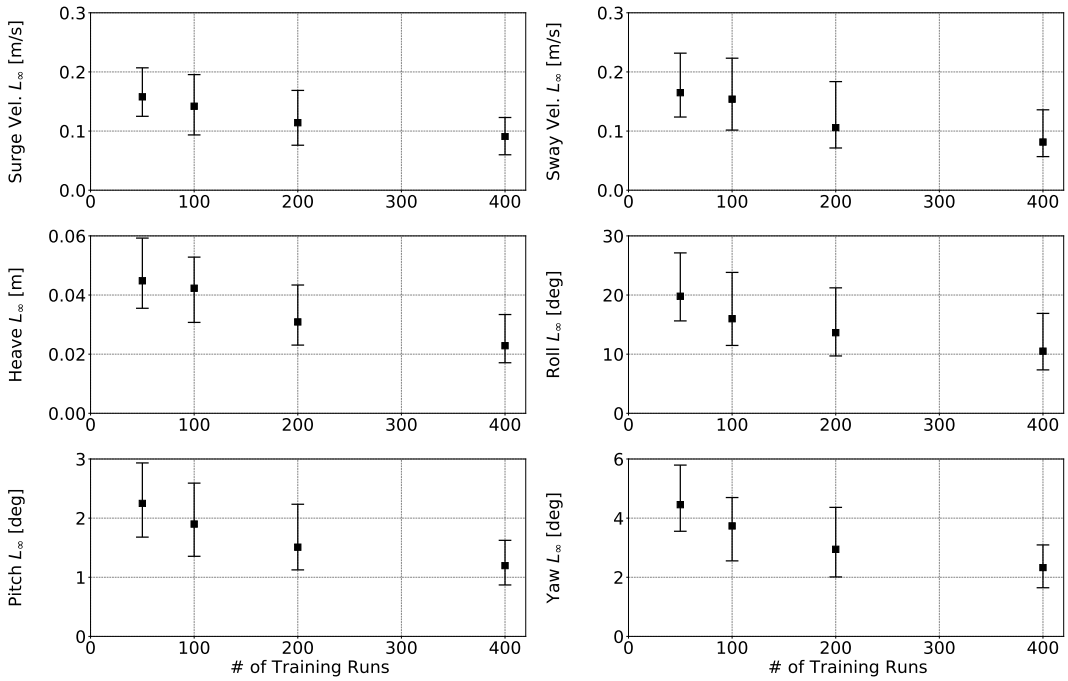

Figure 8.7: Convergence of neural network models with respect to training data for L_∞ error for the 3-D ONRT case study.

In general, as the training data quantity increases, the overall L_2 and L_∞ error decreases, and they all trend towards zero error with 400 training runs. Each DoF demonstrates convergence and less spread in error as training data is increased, indicating that the produced models build an accurate surrogate of the entire dynamical response. L_2 error provides a measure of the entire predicted response time-history. Since the CWG method is interested in the maximum response due to every pair of encounter conditions and wave groups, a low L_∞ error is an indication that the largest values in time-histories are captured. Thus, a low L_2 and L_∞ error, as shown in the model trained with 400 runs, is an indication that not only are response time-histories well-represented in the neural network, but these models could also serve as surrogates for CFD within the CWG method.

A significant advantage of the LSTM neural network surrogate modeling of extreme responses is that it retains the entire prediction time-history of each event, and in

the case of the present methodology, the full 6-DoF representation of the dynamical response can be produced for each composite wave train. This approach differs from the sequential sampling methodologies of *Mohamad and Sapsis* (2018) and *Gong et al.* (2020), which only retain the maximum response due to each wave group with a GPR surrogate. Figures 8.8 through 8.10 and Figures 8.11 through 8.13 show the three time-history predictions for the validation runs with the smallest L_2 and L_∞ error, respectively, for each DoF, with the model trained with 400 runs. The CFD simulations are compared with predictions from neural network model trained with 400 runs and the uncertainty U_{LSTM}, corresponding to 2σ using the Monte Carlo Dropout methodology. Each sub-figure within Figures 8.8 and 8.13 is the time-history with the three smallest evaluations of the L_2 and L_∞ error for that particular DoF and is labeled with the respective validation run index, for reference.

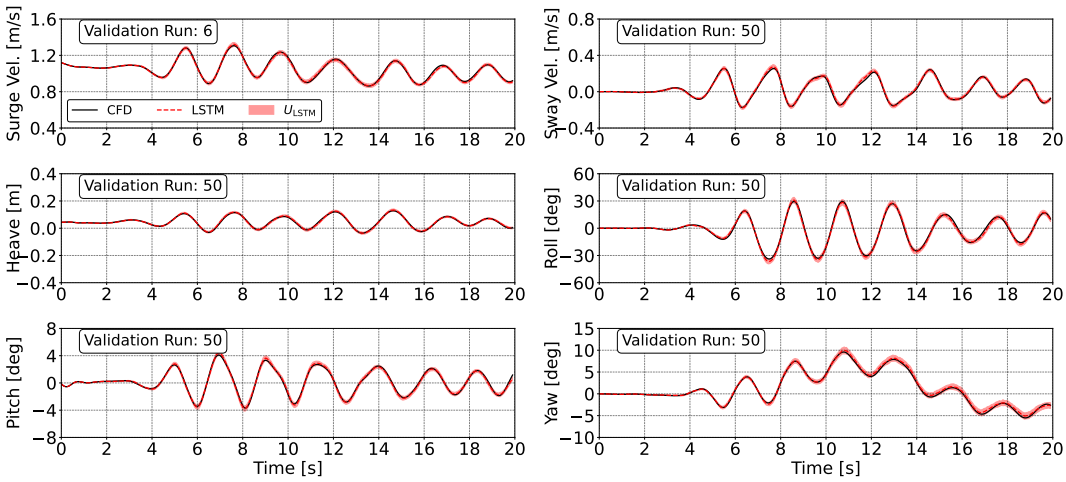

Figure 8.8: Observations with the smallest L_2 error for each DoF with a model trained using 400 simulations for the 3-D ONRT case study.

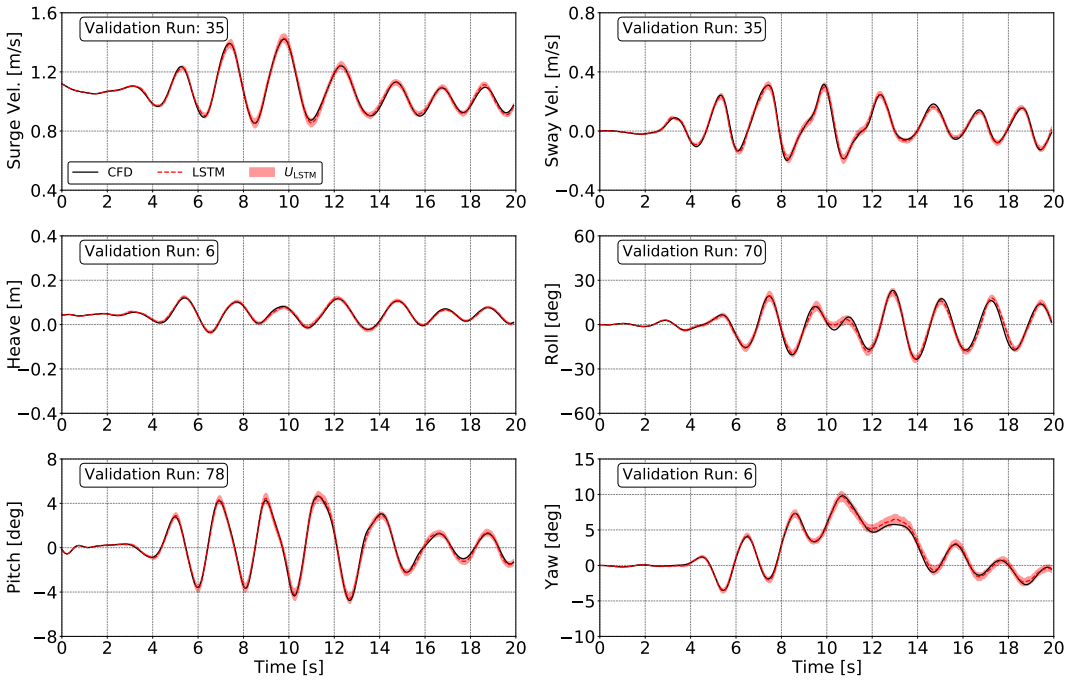

Figure 8.9: Observations with the second smallest L_2 error for each DoF with a model trained using 400 simulations for the 3-D ONRT case study.

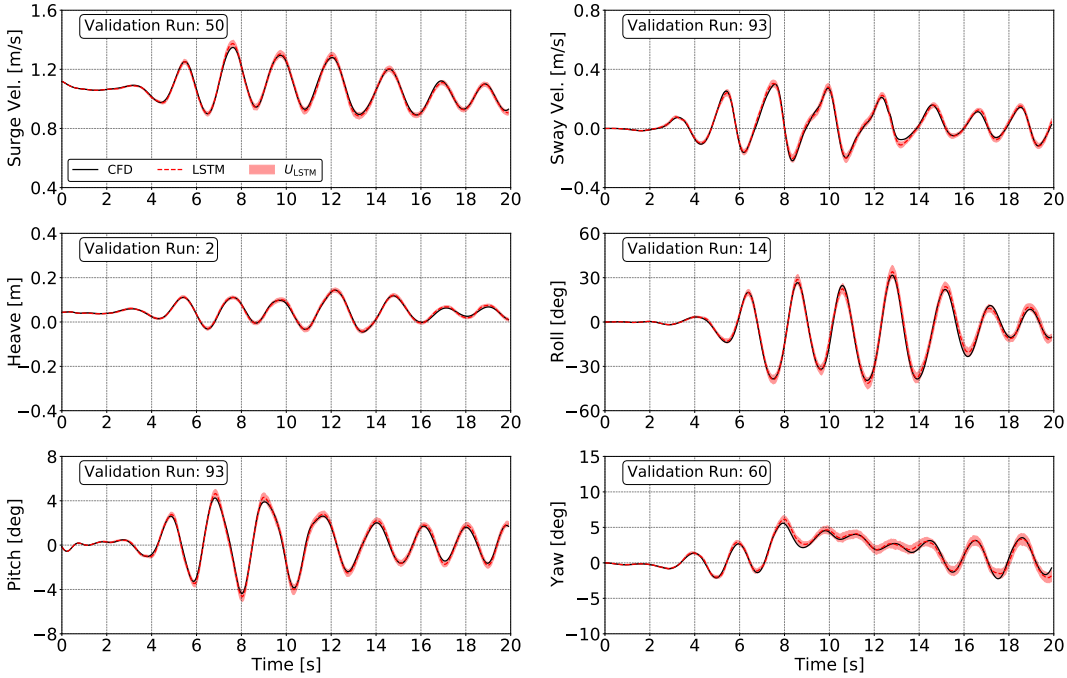

Figure 8.10: Observations with the third smallest L_2 error for each DoF with a model trained using 400 simulations for the 3-D ONRT case study.

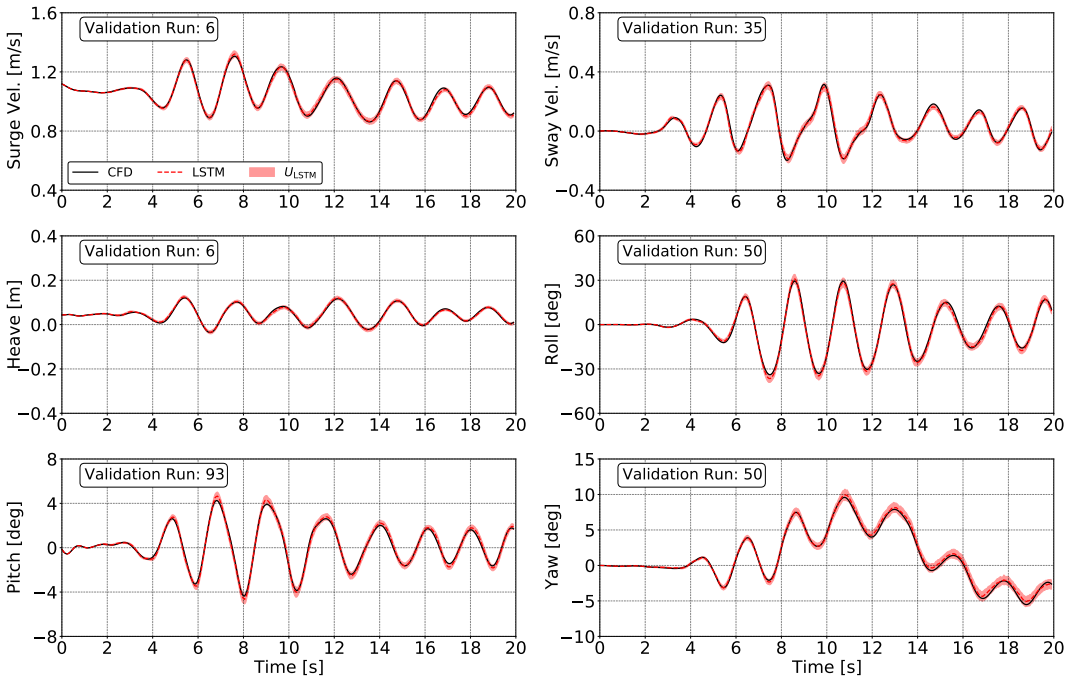

Figure 8.11: Observations with the smallest L_∞ error for each DoF with a model trained using 400 simulations for the 3-D ONRT case study.

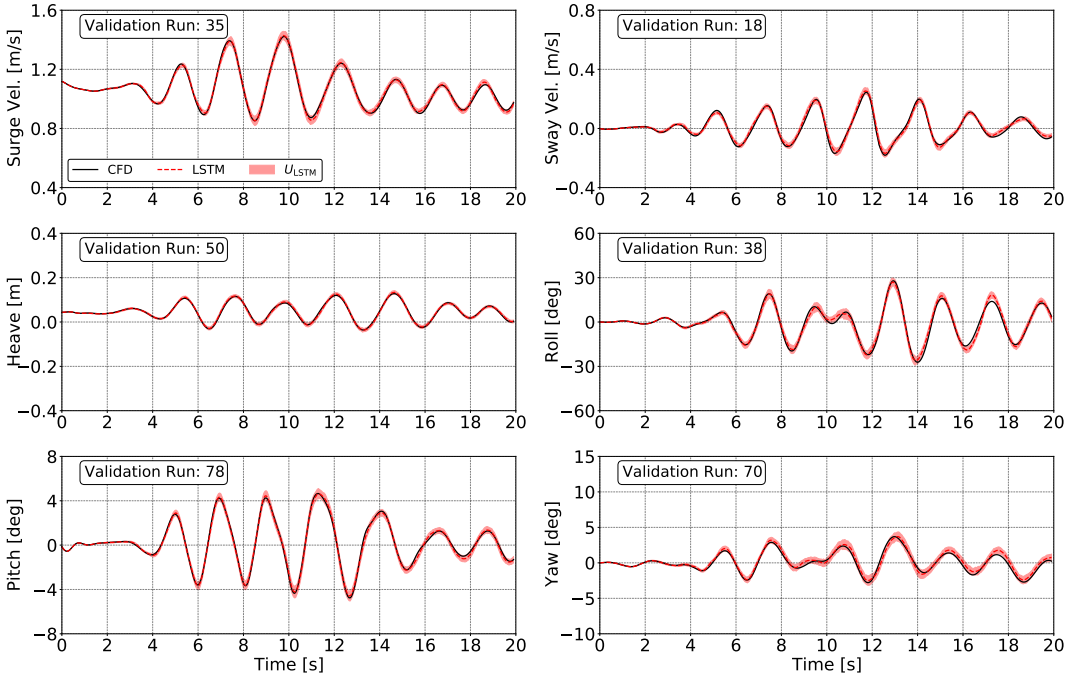

Figure 8.12: Observations with the second smallest L_∞ error for each DoF with a model trained using 400 simulations for the 3-D ONRT case study.

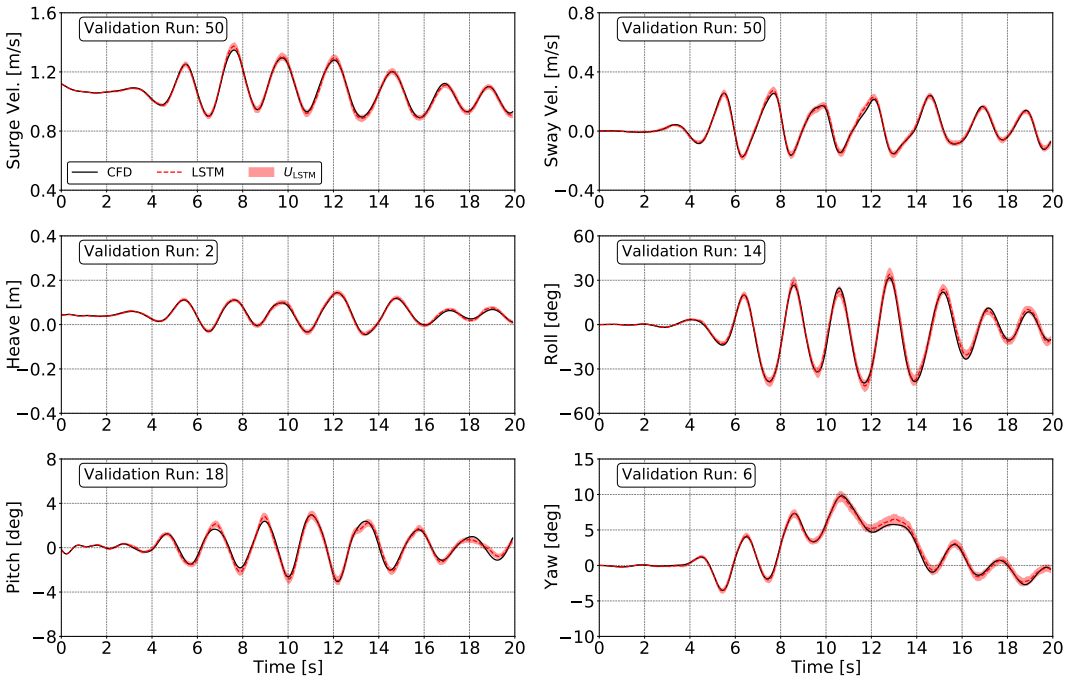

Figure 8.13: Observations with the third smallest L_∞ error for each DoF with a model trained using 400 simulations for the 3-D ONRT case study.

For the validation run with the smallest L_2 and L_∞ error in Figures 8.8 through 8.13, the LSTM predictions agree well with the CFD simulations. Figures 8.14 through 8.16 and Figures 8.17 through 8.19 show the three time-history predictions for the validation runs with the largest L_2 and L_∞ error, respectively, for each DoF, for the model trained with 400 runs. The runs with the largest L_2 and L_∞ error demonstrate much more deviation between the LSTM predictions and the CFD simulations. With the exception of validation run 65 in Figure 8.18, the roll LSTM predictions capture the amplitude of the responses well but with a slight phase shift, which was identified in Section 5.3 as being caused by the difference between the actual and estimated trajectories. The ultimate goal of the CCS framework with the considered encounter conditions in the current case study is to predict the extreme roll for this operating and seaway condition. The observed set of validation runs indicate that the developed LSTM models are able to represent the extreme predictions produced by the CFD

simulations. The LSTM predictions with the largest errors still produced temporal responses that were representative of the desired CFD response.

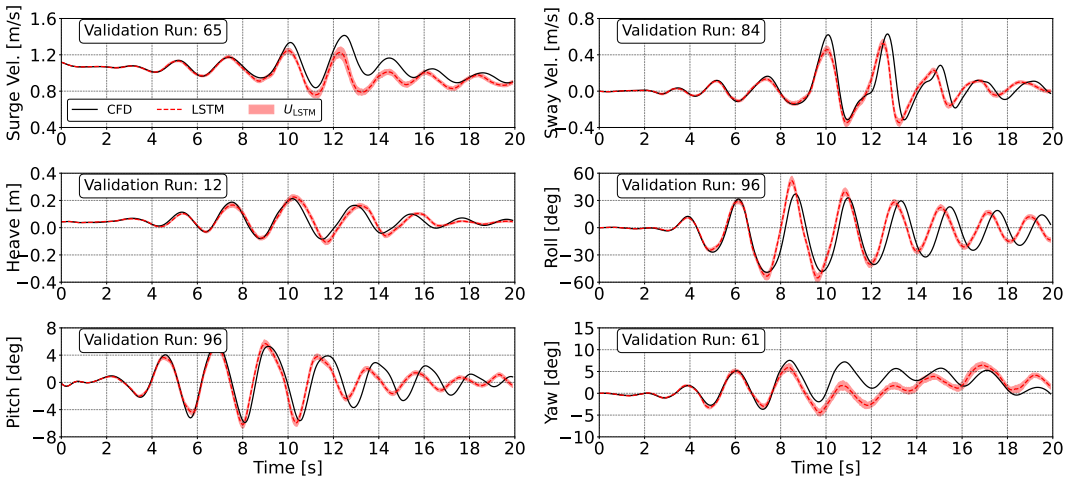

Figure 8.14: Observations with the largest L_2 error for each DoF with a model trained using 400 simulations for the 3-D ONRT case study.

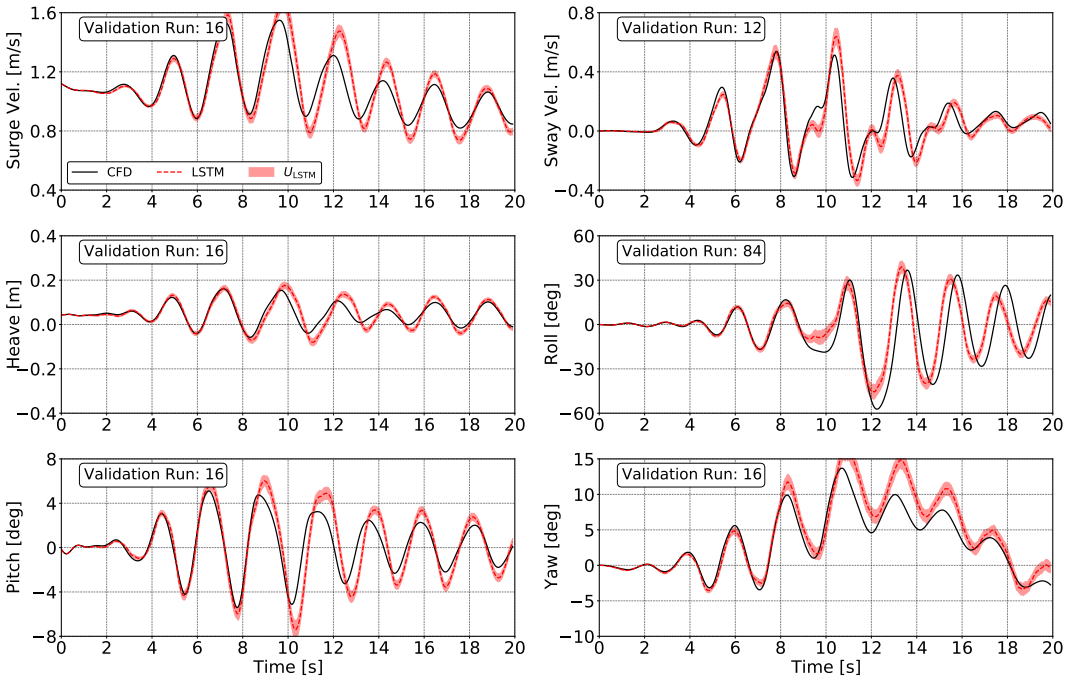

Figure 8.15: Observations with the second largest L_2 error for each DoF with a model trained using 400 simulations for the 3-D ONRT case study.

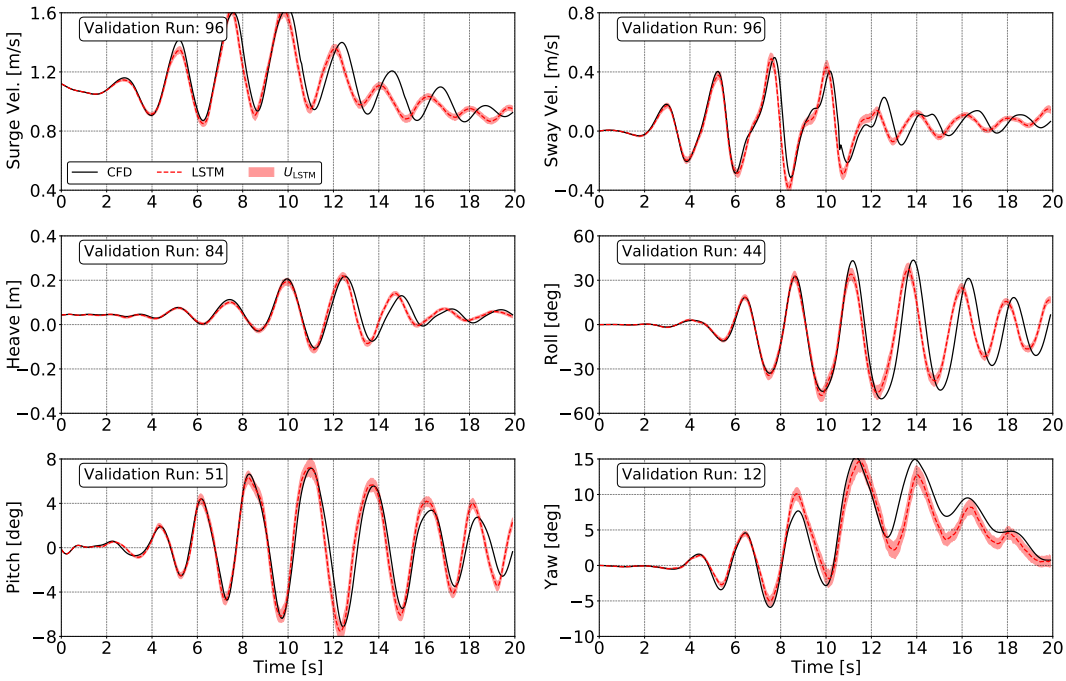

Figure 8.16: Observations with the third largest L_2 error for each DoF with a model trained using 400 simulations for the 3-D ONRT case study.

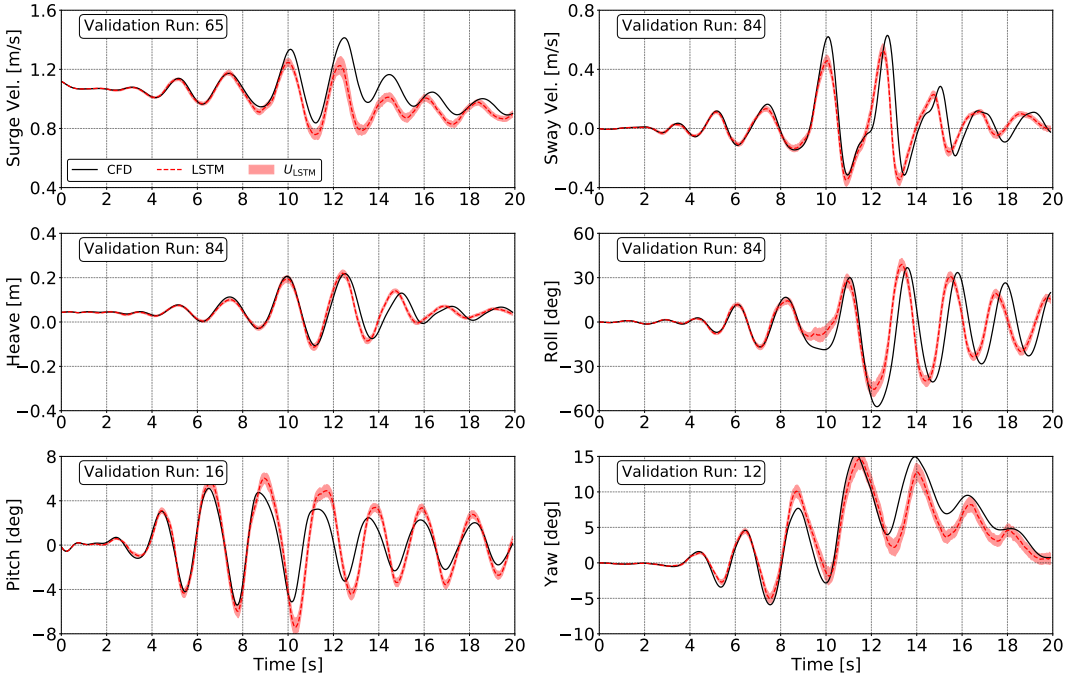

Figure 8.17: Observations with the largest L_∞ error for each DoF with a model trained using 400 simulations for the 3-D ONRT case study.

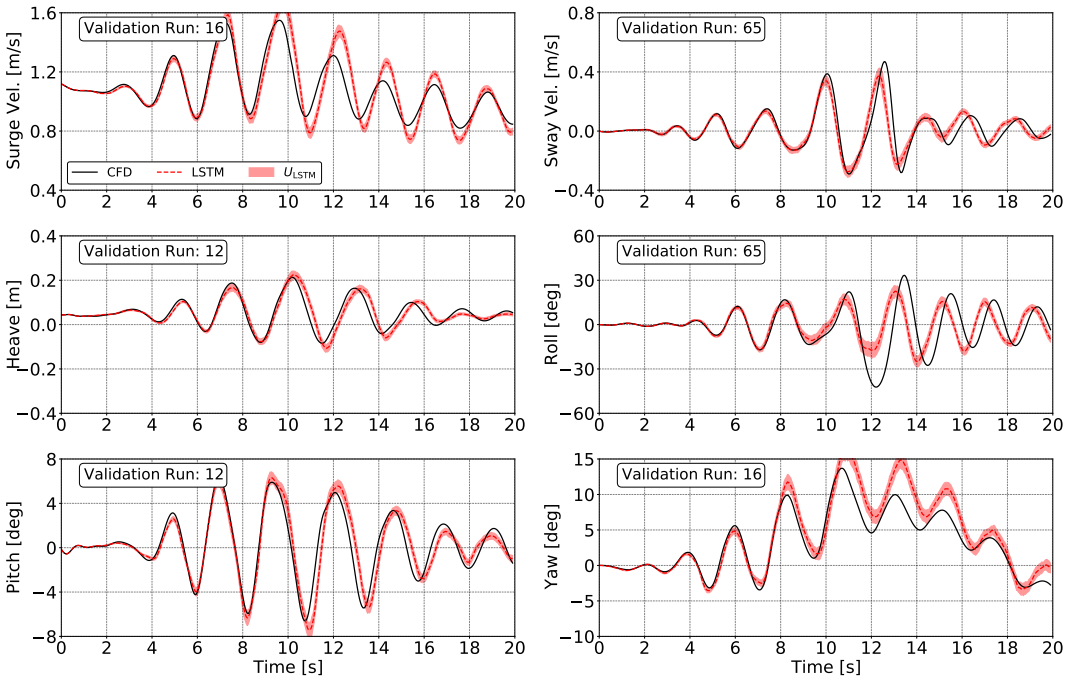

Figure 8.18: Observations with the second largest L_∞ error for each DoF with a model trained using 400 simulations for the 3-D ONRT case study.

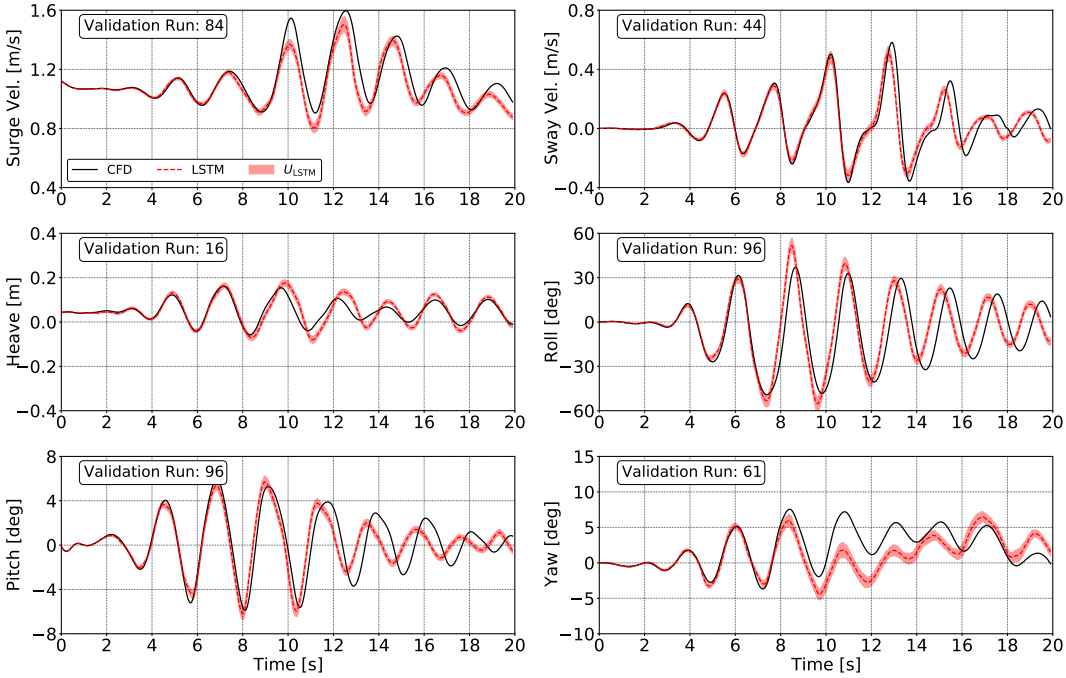

Figure 8.19: Observations with the third largest L_∞ error for each DoF with a model trained using 400 simulations for the 3-D ONRT case study.

Identifying of critical wave groups in the CWG method is fundamental to developing a relationship between the absolute maximum of the response and the encounter conditions and wave groups. Figure 8.20 compares the absolute maximum of heave and roll after the wave group is encountered for the validation dataset. Each marker in Figure 8.20 for a heave and roll corresponds to a single composite wave train and the resulting CFD and LSTM predictions. The solid black line illustrates identical values between the simulation and surrogate model predictions. Each of the trained models follow the solid black line, but there is much more spread between CFD and LSTM predictions for roll. As the training data quantity is increased, the models shift toward the solid black line, indicating higher accuracy as demonstrated in Figures 8.6 and 8.7. Although producing a validation dataset for the entire CC calculation is computationally prohibitive for this case study, the trends in Figure 8.20 are similar to what was demonstrated in the case study in Chapter VII, providing confidence that the LSTM neural network models are capable of reproducing the extreme responses for all the required composite wave trains.

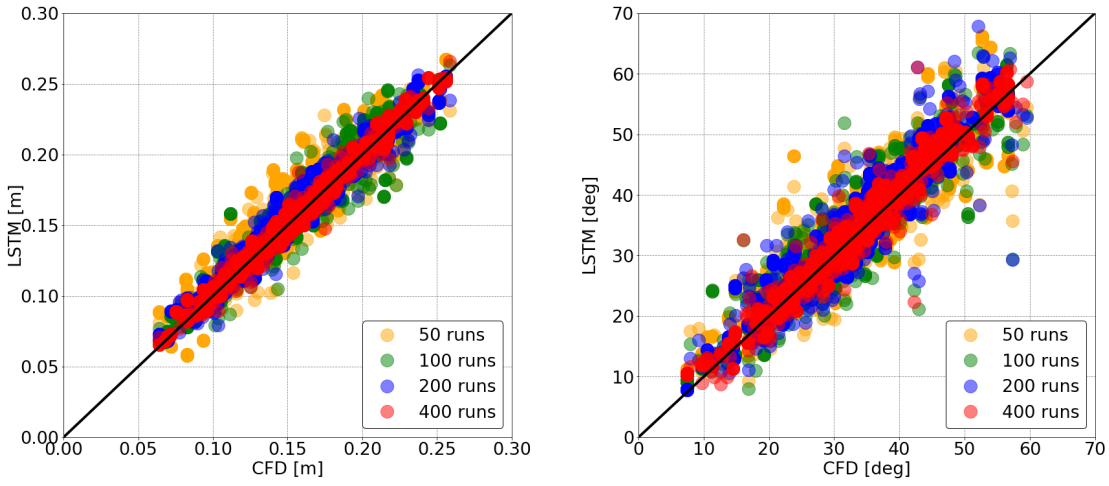

(a) Heave

(b) Roll

Figure 8.20: Comparison of the absolute maximum heave and roll for each composite wave run with CFD and LSTM models with varying amounts of training data for the 3-D ONRT case study.

Figure 8.21 compares the probability of exceedance predictions for all the constructed models in the case study. As the quantity of training data increases, the difference between the probability of exceedance predictions decreases, as does the magnitude of uncertainty from the LSTM models. The clustering of predictions as the quantity of training data increases is an indication of convergence in the LSTM models.

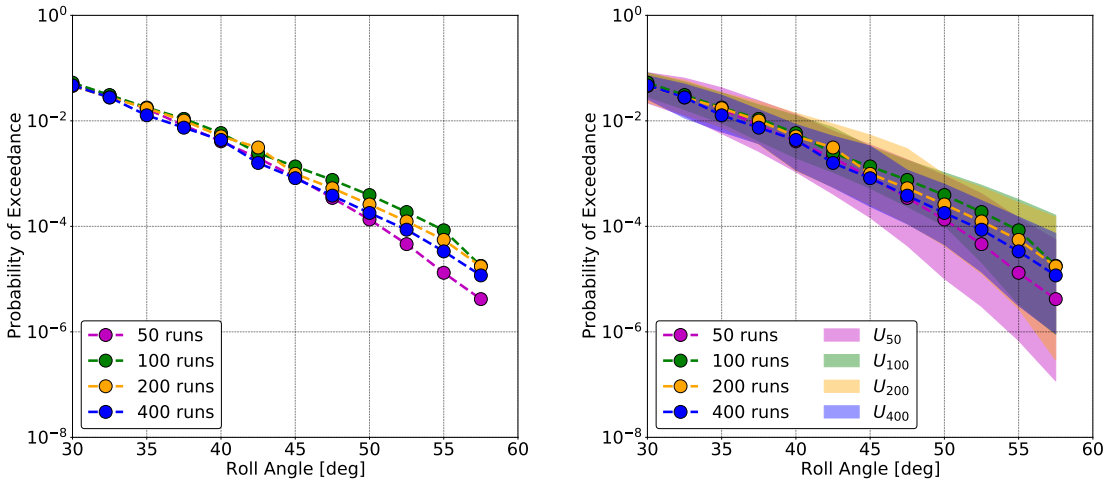

(a) Without Uncertainty (b) With Uncertainty

Figure 8.21: Probability of exceedance of roll in Sea State 7 for the 3-D ONRT case study.

The 3-D case study resulted in a probability of exceedance for 57.5 deg of roll that was roughly an order of magnitude more probable than the 2-D case study in Chapter VII. The increased likelihood of extremes results in less computational cost to observe with Monte Carlo, as reflected in Figure 8.22. The difference between Monte Carlo, estimated by Equation 7.1, and CC for CPU and exposure time is only one order of magnitude at 57.5 deg, as opposed to five orders of magnitude in the 2-D. With this current implementation and due to the systematic nature of combining CWG and CFD, the computational cost is roughly the same across case studies. Therefore, cases with less likely extremes will benefit more from the CCS framework than those with frequent extremes.

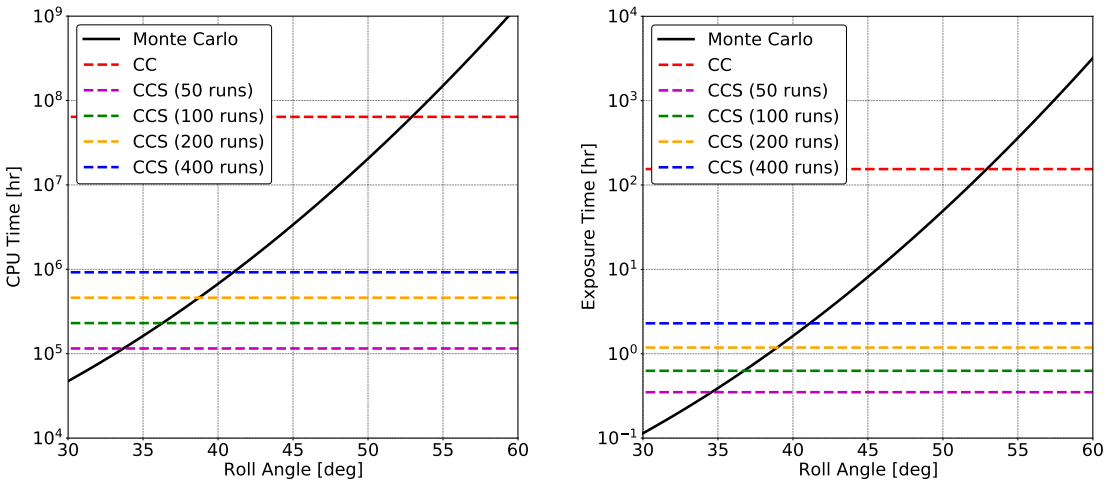

(a) CPU Time

(b) Exposure Time

Figure 8.22: Required CPU and exposure time for the Monte Carlo, CC, and CCS methods for the 3-D ONRT case study.

The probability of exceedance of roll predictions in Figure 8.21 demonstrate the LSTM predictions converge as the quantity of training data increases. The prediction-focused surrogate model retains the temporal predictions for a given wave train and can be applied to random irregular waves as well. Predicting the ship response for 1,000 hours of random irregular waves yields the PDF in Figure 8.23. The sway velocity, heave, roll, and pitch are converging, but there is large spread in the surge velocity and yaw. This difference is likely due to considering a fixed estimated encounter frame for all wave trains. As identified in Section 5.3, a more accurate estimate of the encounter frame results in better overall LSTM models.

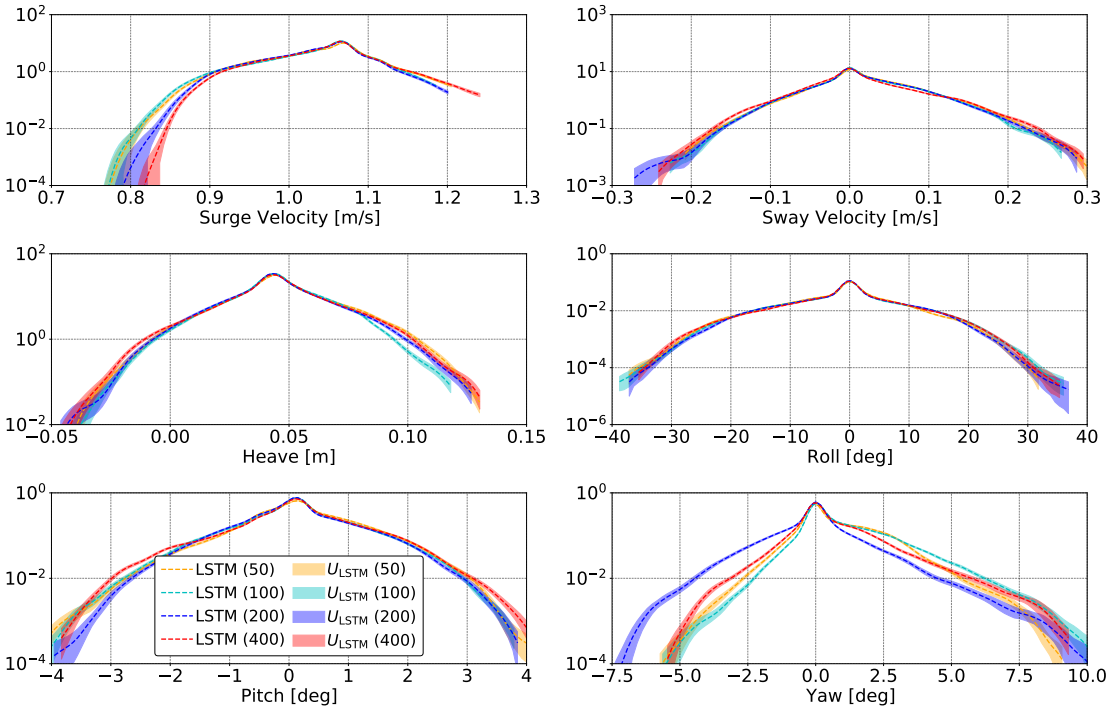

Figure 8.23: Comparison of the PDF in a logarithmic scale for each DoF for the 3-D ONRT case study.

The presented 3-D case study constitutes the first time that a probabilistic method and CFD are combined to not only observe extreme events for a free-running vessel, but also quantify the probability of their occurrence with the observations. Although developing a complete validation dataset for Monte Carlo or CC is computationally expensive, the limited validation dataset and the case study in Chapter VII provides confidence that the CCS framework produces observations of extremes that yield quantitative probabilities of their occurrence.

CHAPTER IX

Conclusion

Ensuring the safety of a vessel in extreme ocean conditions is a crucial consideration for designers and operators. Vessels must withstand a variety of responses through their lifetime, and proper probabilistic characterization of the extremes is critical, as is understanding what causes the extreme events, in order to identify an issue in a design or limit the operational profile of existing platforms. This dissertation develops the CCS framework in order to address the three main challenges in the observation and probabilistic quantification of extreme ship responses:

1. Stochasticity of the ocean environment and rareness of extremes
2. Complex nonlinear hydrodynamic behavior of a vessel in large amplitude waves
3. Evaluation costs associated with nonlinear hydrodynamic behavior

The *stochasticity of the ocean environment and rareness of extremes* is addressed by implementing the CWG method, which provides a systematic methodology of constructing deterministic wave groups, evaluating the ship response due to the different wave groups and encounter conditions to identify critical wave groups that cause near-exceedances of thresholds of interest, and combines the probability of these critical wave groups to calculate a probability of exceedance.

The *complex nonlinear hydrodynamic behavior of a vessel in large amplitude waves* is managed by introducing high-fidelity numerical hydrodynamic predictions with CFD, specifically URANS. High-fidelity numerical hydrodynamic methods can provide quantitative evaluations of the extreme ship responses in waves. However, the accuracy of URANS methods comes at a considerable computational cost.

The *evaluation costs associated with nonlinear hydrodynamic behavior* from the URANS simulations is addressed by the introduction of LSTM neural networks to construct a surrogate model of a limited set of URANS predictions. The trained LSTM neural network can then be utilized to perform all the response evaluations required for the CWG method. The LSTM neural network model yields temporal predictions of the ship response. Therefore, the ability to produce observations with the CCS framework is maintained.

The concept of *natural initial conditions* was developed in this dissertation by embedding deterministic wave groups into random wave trains from previous simulations of ship responses in waves in a manner with which a specified encounter condition is achieved at the moment the wave group is encountered. The natural initial condition allows for the enforcement of encounter conditions and the generation of wave groups to be both physically realizable and reproducible, without any intrusive constraints.

This dissertation also established a methodology of representing the 6-DoF response of a free-running vessel with LSTM neural networks. One main issue with creating a SI model for free-running vessels is that the instantaneous trajectory is unknown *a priori*. Therefore, the encountered wave field around the ship is also unknown. However, if the trajectories are estimated from the training data, the wave field in an approximate encounter frame provides a first-order estimate of the waves that the ship encounters, which makes the LSTM possible for 6-DoF motions.

Three different case studies are described in this dissertation. Section 5.3 contains a case study with the DTMB 5415 hull form and simulations from the medium-fidelity

numerical hydrodynamic simulation tool LAMP, in random irregular waves. This case study focuses on evaluating the ability of the developed LSTM neural network modeling methodology to represent the 6-DoF response of a free-running vessel for both course-keeping as well as turning circles in random irregular waves. The developed modeling methodology with the estimated encounter frames is able to reproduce the temporal predictions from LAMP.

Chapter VII outlines a case study for a 2-D midship section of the ONRT employing the CCS framework. Probability of exceedance calculations are performed for the CCS framework with models trained with varying amounts of training data and an alternative methodology, where CFD is only considered to develop the probability calculations (CWG-CFD). With 200 training runs, the LSTM neural network model reproduces the CC results at a computational cost savings of two orders of magnitude, with respect to the CC method and seven orders of magnitude, with respect to a Monte Carlo approach.

Chapter VIII extends the 2-D case study in VII to a 3-D free-running 6-DoF ONRT. Similarly to the 2-D case study, LSTM neural network models are constructed with varying levels of training data. However, due to the large increase in computational cost for 3-D CFD simulations, only 100 validations runs were available to evaluate the models. In accordance with the 2-D case study, the resulting probability of exceedance calculations converge at around 200 training runs and produce LSTM predictions that are representative of the CFD validation simulations. The similarities between the results of the 3-D and 2-D case studies builds confidence that the CCS framework produces quantitative probabilistic evaluations and observations of extreme ship response events.

9.1 Contributions

This dissertation contributes extensively to the areas of probabilistic methods for extremes, numerical hydrodynamics, and prediction-focused surrogate modeling for marine dynamics. The major contribution from this dissertation is the overall development of the CCS framework outlined in Chapter VI. Each resulting contribution, is a consequence of the different methodologies required within the framework. The CCS framework develops a methodology for quantifying the probability of extreme events and producing quantitative observations of these extremes to provide insight into the mechanisms that cause them. Previous extreme event methodologies have typically focused on only the statistics or the observations. If both were included, it was typically for cases with simplified hydrodynamic models that did not produce physically realizable events.

Another large contribution is the development of the natural initial condition in Section 4.1. As described in Chapter IV, prior to the research in this dissertation, initial conditions were typically ignored, enforced intrusively, or implemented in simplified ODE models for extreme event evaluations. None of the previous research addressed the need for both enforcing initial conditions and producing physically realizable wave groups simultaneously. The natural initial condition methodology provides a solution to this issue and not only produces physically realizable initial conditions and wave groups, but also provides control over what the encounter condition is at the precise moment of wave group encounter so that the variation of the encounter state is prescribed and not random. Additionally, the natural initial condition is valid for both simulations and experiments. Previous research with initial conditions and wave group methods discussed experimental implementations that required intrusive dynamic mechanisms that would lead to unrealistic events. The natural initial condition enables, for the first time, the observation of curated extreme events with initial conditions in an experimental setting.

A significant contribution that arose as a result of the expensive CFD simulations, is the development of the LSTM modeling methodology for free-running vessels in Chapter V. In the context of this dissertation, it is a technique of yielding observations of extreme events that are not only statistically representative of the CFD-produced extreme statistics, but also are able to provide temporal predictions with uncertainty estimates that are aligned with high-fidelity predictions. This dissertation constitutes the first time that a neural network model was employed to represent the 6-DoF response of free-running vessels for course-keeping, turning circles, and extreme roll with rigorous and extensive validation. Although the LSTM models in Chapters VII and VIII are constructed with wave groups from the CWG method, they are not constrained to only wave groups generated within those methods, and the models could be applied to random irregular waves as well to construct PDFs of each DoF, as is demonstrated throughout the cases studies. The CWG method, or another wave group method, could serve as a means of developing extreme ship response events that serve as training data for the surrogate models. The resulting models can then be employed as a proxy for simulation in a wide variety of areas. Outside of the extreme event evaluations that this dissertation focused on, the LSTM methodology developed for the CCS framework could and should be adapted for real-time forecasting and other SI applications.

The final contribution of this dissertation is the utilization of CFD for ship responses in extreme waves. Previous research and application of CFD for ship hydrodynamics has typically emphasized resistance, maneuvering and other similar cases, but routinely is not considered for seakeeping due to its computational cost and the large amount of exposure time required to gain meaningful statistics. Outside of research, an aversion persists to applying CFD to seakeeping problems across the international ship hydrodynamics community, which tends to focus on potential flow BEM approaches.

This dissertation demonstrates that 6-DoF CFD simulations can be applied to ship

motion in wave problems with careful consideration and targeting of prescribed events of interest, like the CWG method provides. Not only can CFD be employed when short-time window events of interest are available, but it also absolutely should be considered for problems that are inherently poorly predicted in the medium-fidelity methods, such as significant green water events. The simulation setup in this dissertation, and the previous research that inspired it should provide a sufficient starting point.

9.2 Future Work

This dissertation developed several methodologies that enabled the observation and probabilistic quantification of extreme ship response events. Advancement of the state-of-the-art in multiple areas has also revealed future research avenues. For instance, the case studies presented denote a subset of the possible extremes that a vessel can experience throughout their lifetime. In the future, the CCS framework should be applied to cases of extreme pitch, surf-riding, broaching, and seaway loads. Application to different response quantities will require some investigation of the proper encounter conditions, and the natural initial condition methodology can be employed to understand the sensitivity of different quantity combinations. Additionally, steps toward including the uncertainty of the encounter conditions in the probability of exceedance were taken in Section 6.1, but further research is required for understanding its propagation from the response to the statistics.

Furthermore, the case studies in Chapters VII and VIII considered extreme roll, but the datasets did not include any observations of capsizing. The CWG method and CFD have been applied to instances of capsizing, but future research should look into the application of the LSTM methodology to capsizing and other instabilities.

Progress was also made in the extension of the LSTM neural network to include multiple speeds, headings, and seas states in random irregular waves for course-keeping in Section 5.4. Both of the extreme roll case studies and the formulation of LSTM

neural networks within the CCS framework focused on training with data from a single condition. The CCS framework should be extended to multiple conditions in order to benefit from the computational cost savings that are a result of creating more generalized models, instead of creating several condition-specific models. Additionally, the main deficiency in the LSTM surrogate modeling technique is that the current methodology considers a single encounter frame for a particular condition, and it is not specific to individual wave trains. Future research should consider developing a methodology for providing an improved estimate of the instantaneous encounter frame for each specific wave train. As demonstrated in the case studies in Section 5.3, the better the encounter frame is estimated, the more accurate the LSTM models are.

Everything in this dissertation was completed for uni-directional linear wave fields. Future research should extend the CCS framework to multi-directional seas and and nonlinear waves (*Gong et al.*, 2021). Extension to other wave fields may require some modifications to the Markov chain wave group construction.

Validation of the methodology and neural networks are provided throughout the dissertation in every case study. However, the computational cost of CFD prevented the development of an extensive Monte Carlo dataset for complete validation of the probability of exceedance calculation for free-running vessels for the cases study in Chapter VIII. There is high confidence that the LSTM neural network can represent predictions resulting from CWG method and CFD, but more research is needed to fully validate the framework for free-running vessels. Future research should produce an extensive Monte Carlo dataset for validation with a medium-fidelity numerical hydrodynamic tool like LAMP, which is much more computationally efficient than CFD, but is capable of reproducing much of the dominating phenomena in extreme ship responses in waves. The CCS framework could then be implemented with LAMP to provide further validation.

BIBLIOGRAPHY

BIBLIOGRAPHY

Abadi, M., et al. (2015), TensorFlow: Large-scale machine learning on heterogeneous systems, software available from tensorflow.org.

Alford, L. (2008), Estimating extreme responses using a non-uniform phase distribution, Ph.D. thesis, The University of Michigan, Ann Arbor, MI.

Alford, L. K., D.-H. Kim, and A. W. Troesch (2011), Estimation of extreme slamming pressures using the non-uniform Fourier phase distributions of a design loads generator, *Ocean Engineering*, *38*(5), 748 – 762, doi:https://doi.org/10.1016/j.oceaneng.2010.12.008.

Anastopoulos, P. A., and K. J. Spyrou (2016), Ship dynamic stability assessment based on realistic wave group excitations, *Ocean Engineering*, *120*, 256 – 263, doi:https://doi.org/10.1016/j.oceaneng.2016.04.018.

Anastopoulos, P. A., and K. J. Spyrou (2017), Evaluation of the critical wave groups method for calculating the probability of extreme ship responses in beam seas, in *Proceedings of the 16th International Ship Stability Workshop*, pp. 131–138, Belgrade, Serbia.

Anastopoulos, P. A., and K. J. Spyrou (2019), Evaluation of the critical wave groups method in calculating the probability of ship capsize in beam seas, *Ocean Engineering*, *187*, 106,213, doi:https://doi.org/10.1016/j.oceaneng.2019.106213.

Anastopoulos, P. A., K. J. Spyrou, C. C. Bassler, and V. Belenky (2016), Towards an improved critical wave groups method for the probabilistic assessment of large ship motions in irregular seas, *Probabilistic Engineering Mechanics*, *44*, 18 – 27, doi:https://doi.org/10.1016/j.probengmech.2015.12.009.

Araki, M., H. Sadat-Hosseini, Y. Sanada, K. Tanimoto, N. Umeda, and F. Stern (2012), Estimating maneuvering coefficients using system identification methods with experimental, system-based, and CFD free-running trial data, *Ocean Engineering*, *51*, 63–84.

Bales, S. L. (1983), Designing Ships to the Natural Environment, *Naval Engineers Journal*, *95*(2), 31–40, doi:doi:10.1111/j.1559-3584.1983.tb00574.x.

Bandyk, P. J. (2009), A body-exact strip theory approach to ship motion computations, Ph.D. thesis, The University of Michigan, Ann Arbor, MI.

Bassler, C. C., M. J. Dipper, and M. Melendez (2019), *Experimental Ship Dynamic Stability Assessment Using Wave Groups*, pp. 507–520, Springer International Publishing, doi:10.1007/978-3-030-00516-0_30.

Belenky, V. (1993), A capsizing probability computation method, *Journal of Ship Research*, *37*, 200–207.

Belenky, V., and B. Campbell (2011), Evaluation of the exceedance rate of a stationary stochastic process by statistical extrapolation using the envelope peaks over threshold (EPOT) method, *Tech. Rep. NSWCCD-50-TR-2011/032*, Naval Surface Warfare Center Carderock Division, Hydromechanics Dept, West Bethesda, MD.

Belenky, V., K. M. Weems, W. Lin, and K. J. Spyrou (2010), Numerical evaluation of capsizing probability in quartering seas with split-time method, in *Proceedings of the 28th Symposium on Naval Hydrodynamics*.

Belenky, V., A. M. Reed, and K. M. Weems (2011), *Probability of Capsizing in Beam Seas with Piecewise Linear Stochastic GZ Curve*, 531-554 pp., Springer Netherlands, Dordrecht, doi:10.1007/978-94-007-1482-3_30.

Belenky, V., K. M. Weems, C. C. Bassler, M. J. Dipper, B. L. Campbell, and K. J. Spyrou (2012), Approaches to rare events in stochastic dynamics of ships, *Probabilistic Engineering Mechanics*, *28*, 30 – 38, doi:https://doi.org/10.1016/j.probengmech.2011.08.020.

Belknap, W. F., and A. M. Reed (2019), *TEMPEST—A New Computationally Efficient Dynamic Stability Prediction Tool*, 3-21 pp., Springer International Publishing.

Bishop, R. C., W. Belknap, C. Turner, B. Simon, and J. H. Kim (2005), Parametric Investigation on the Influence of GM, Roll Damping, and Above-Water Form on the Roll Response of Model 5613, *Tech. Rep. NSWCCD-50-TR-2005/027*, Naval Surface Warfare Center Carderock Division, Hydromechanics Dept, West Bethesda, MD.

Bretschneider, C. (1959), Wave variability and wave spectra for wind-generated gravity waves, *Tech. Rep. Technical Memorandum, No. 118*, Beach Erosion Board, US Army Corps of Engineers.

Campbell, B., and V. Belenky (2010a), Statistical extrapolation for evaluation of probability of large roll, in *Proceedings of the 11th International Symposium on Practical Design of Ships and Other Floating Structures*.

Campbell, B., and V. Belenky (2010b), Assessment of short-term risk with Monte-Carlo method, in *Proceedings of the 11th International Ship Stability Workshop*.

Chollet, F., et al. (2015), Keras, `https://keras.io`.

Cousins, W. T., and T. P. Sapsis (2016), Reduced-order precursors of rare events in unidirectional nonlinear water waves, *Journal of Fluid Mechanics*, *790*, 368–388.

D'Agostino, D., A. Serani, F. Stern, and M. Diez (2022), Time-series forecasting for ships maneuvering in waves via recurrent-type neural networks, *Journal of Ocean Engineering and Marine Energy*, *8*, 479–487, doi:10.1007/s40722-022-00255-w.

del Águila Ferrandis, J., M. S. Triantafyllou, C. Chryssostomidis, and G. E. Karniadakis (2021), Learning functionals via LSTM neural networks for predicting vessel dynamics in extreme sea states, *Proceedings of the Royal Society A: Mathematical, Physical and Engineering Sciences*, *477*(2245), 20190,897, doi:10.1098/rspa.2019.0897.

Filip, G., D.-H. Kim, S. Sahu, J. de Kat, and K. Maki (2014), Bulbous Bow Retrofit of a Containership Using an Open Source Computational Fluid Dynamics (CFD) Toolbox, in *Proceedings of the 2014 SNAME Maritime Convention*.

Filip, G. P., W. Xu, and K. J. Maki (2017), URANS predictions of resistance and motions of the KCS in head waves, *Tech. Rep. 355*, University of Michigan, Ann Arbor, MI.

Filip, G. P., W. Xu, and K. J. Maki (2020), A method for the prediction of extreme wave loads on a fixed platform, *Applied Ocean Research*, *97*, 101,993, doi:https://doi.org/10.1016/j.apor.2019.101993.

Gaidai, O., G. Storhaug, and A. Naess (2016), Extreme Value Statistics of Large Container Ship Roll, *Journal of Ship Research*, *60*(02), 92–100, doi:10.5957/jsr.2016.60.2.92.

Gal, Y., and Z. Ghahramani (2016a), Dropout as a Bayesian Approximation: Representing Model Uncertainty in Deep Learning, in *Proceedings of the 33rd International Conference on Machine Learning (ICML-16)*.

Gal, Y., and Z. Ghahramani (2016b), A Theoretically Grounded Application of Dropout in Recurrent Neural Networks, in *Advances in Neural Information Processing Systems*, vol. 29, pp. 1019–1027.

Gong, X., and Y. Pan (2022a), Sequential bayesian experimental design for estimation of extreme-event probability in stochastic input-to-response systems, *Computer Methods in Applied Mechanics and Engineering*, *395*, 114,979, doi:https://doi.org/10.1016/j.cma.2022.114979.

Gong, X., and Y. Pan (2022b), Effects of varying initial conditions of ship encountering wave groups in computing extreme motion statistics, in *Proceedings of the 34rd Symposium on Naval Hydrodynamics*.

Gong, X., Z. Zhang, K. Maki, and Y. Pan (2020), Full Resolution of Extreme Ship Response Statistics, in *Proceedings of the 33rd Symposium on Naval Hydrodynamics*.

Gong, X., K. M. Silva, K. J. Maki, and Y. Pan (2021), Effect of wave nonlinearity on the statistics of wave groups and extreme ship motions, in *Proceedings of the 36th International Workshop on Water Waves and Floating Bodies*.

Hasselmann, K., et al. (1973), *Measurements of wind-wave growth and swell decay during the Joint North Sea Wave Project (JONSWAP)*, Deutshes Hydrographisches Institut, Hamburg, Germany.

Hochreiter, S., and J. Schmidhuber (1997), Long short-term memory, *Neural computation*, *9*(8), 1735–1780.

Hosseini, S. H. S. (2009), CFD prediction of ship capsize: parametric rolling, broaching, surf-riding, and periodic motions, Ph.D. thesis, University of Iowa, doi:10.17077/etd.c2qgkc5s.

ITTC (2011), Fresh Water and Seawater Properties, *ITTC Procedure 7.5-02-01-03, Revision 02*, 26th International Towing Tank Conference.

Jacobsen, N. G., D. R. Fuhrman, and J. Fredsøe (2012), A wave generation toolbox for the open-source CFD library: OpenFOAM®, *International Journal for Numerical Methods in Fluids*, *70*(9), 1073–1088, doi:10.1002/fld.2726.

Jensen, J. (2007), Efficient estimation of extreme non-linear roll motions using the first-order reliability method (FORM), *Journal of Marine Science and Technology*, *12*, 191–202, doi:https://doi.org/10.1007/s00773-007-0243-z.

Kim, D.-H. (2012), Design loads generator: Estimation of extreme environmental loadings for ship and offshore applications, Ph.D. thesis, The University of Michigan, Ann Arbor, MI.

Kimura, A. (1980), Statistical properties of random wave groups, in *Proceedings of the 17th International Coastal Engineering Conference*, pp. 2955–2973, ASCE, Sydney, Australia.

Kingma, D. P., and J. Ba (2014), Adam: A method for stochastic optimization, doi:10.48550/ARXIV.1412.6980.

Knight, B. (2021), Data-Driven Propeller Modeling for Ship Maneuvering, Ph.D. thesis, University of Michigan.

Knight, B., W. Xu, and K. Maki (2020), Numerical Prediction of Self-Propulsion in Extreme Head Seas, in *Proceedings of the 33rd Symposium on Naval Hydrodynamics*.

Knight, B., K. Silva, and K. Maki (2022), Data-Driven Propeller and Rudder Modeling for Maneuvering Analysis of the ONR Tumblehome, in *Proceedings of the 41st International Conference on Ocean, Offshore & Arctic Engineering OMAE 2022*.

Kogiso, N., and Y. Murotsu (2018), Application of first order reliability method to ship stability–final report of SCAP committee (part 5), in *Proceedings of the 6th Osaka Colloquium on Seakeeping and Stability of Ships*.

Larsson, L., F. Stern, M. Visonneau, T. Hino, N. Hirata, and J. Kim (2015), *Proceedings of the Tokyo 2015 Workshop on CFD in Ship Hydrodynamics*.

Lee, T., K. Ahn, H. Lee, and D. Yum (2003), On an Empirical Prediction of Hydrodynamic Coefficients for Modern Ship Hulls, in *Proceedings of the International Conference on Marine Simulation and Ship Maneuverability (MARSIM 03)*.

Lee, Y.-W., L. McCue, M. Obar, and A. Troesch (2006), Experimental and Numerical Investigation Into the Effects of Initial Conditions on a Three Degree of Freedom Capsize Model, *Journal of Ship Research*, *50*(01), 63–84, doi:10.5957/jsr.2006.50.1.63.

Lin, W., and D. Yue (1993), Time-Domain Analysis for Floating Bodies in Mild-Slope Waves of Large Amplitude, in *Proceedings of the 8th International Workshop on Water Waves and Floating Bodies*.

Lin, W., M. Meinhold, N. Salvesen, and D. Yue (1994), Large-Amplitude Motions and Waves Loads for Ship Design, in *Proceedings of the 20th Symposium on Naval Hydrodynamics*.

Lin, W. M., and D. Yue (1990), Numerical Solutions for Large-Amplitude Ship Motions in the Time-Domain, in *Proceedings of the 18th Symposium on Naval Hydrodynamics*.

Menter, F., M. Kuntz, and R. Langtry (2003), Ten years of industrial experience with the SST turbulence model, in *Proceedings of the fourth international symposium on turbulence, heat and mass transfer*.

Mohamad, M. A., and T. P. Sapsis (2018), Sequential sampling strategy for extreme event statistics in nonlinear dynamical systems, *Proceedings of the National Academy of Sciences*, *115*(44), 11,138–11,143, doi:10.1073/pnas.1813263115.

Mousaviraad, S. M. (2010), Cfd prediction of ship response to extreme winds and/or waves, Ph.D. thesis, University of Iowa, doi:10.17077/etd.9qppvv9h.

Nathan, A. (1975), Trigonometric interpolation of function and derivative data, *Information and Control*, *28*(3), 192–203, doi:https://doi.org/10.1016/S0019-9958(75)90279-X.

NATO (1983), *Standardized Wave and Wind Environments and Shipboard Reporting of Sea Conditions*, Standardization Agreement STANAG 4194, North Atlantic Treaty Organization.

Nielsen, U. D. (2017), Transformation of a wave energy spectrum from encounter to absolute domain when observing from an advancing ship, *Applied Ocean Research*, *69*, 160–172, doi:https://doi.org/10.1016/j.apor.2017.10.011.

Ochi, M. K. (1998), *Ocean Waves: The Stochastic Approach*, Cambridge Ocean Technology Series, Cambridge University Press, doi:10.1017/CBO9780511529559.

Paroka, D., and N. Umeda (2006), Capsizing probability prediction for a large passenger ship in irregular beam wind and waves: comparison of analytical and numerical methods, *Journal of Ship Research*, *50*(4), 371–377.

Piro, D. J., and K. J. Maki (2013), Hydroelastic analysis of bodies that enter and exit water, *Journal of Fluids and Structures*, *37*, 134 – 150, doi:https://doi.org/10.1016/j.jfluidstructs.2012.09.006.

Reed, A. M., and R. F. Beck (2016), Advances in the Predictive Capability for Ship Dynamics in Extreme Waves, in *Proceedings of the 2016 SNAME Maritime Convention*.

Sadat-Hosseini, H., D. Kim, S. Toxopeus, M. Diez, and F. Stern (2015), Cfd and potential flow simulations of fully appended free running 5415m in irregular waves, in *World Maritime Technology Conference*.

Sapsis, T. P. (2021), Statistics of Extreme Events in Fluid Flows and Waves, *Annual Review of Fluid Mechanics*, *53*(1), 85–111, doi:10.1146/annurev-fluid-030420-032810.

Schirmann, M. L., M. D. Collette, and J. W. Gose (2020), Improved vessel motion predictions using full-scale measurements and data-driven models, in *Proceedings of the 33rd Symposium on Naval Hydrodynamics*.

Serani, A., M. Diez, F. van Walree, and F. Stern (2021), URANS analysis of a free-running destroyer sailing in irregular stern-quartering waves at sea state 7, *Ocean Engineering*, *237*, 109,600, doi:https://doi.org/10.1016/j.oceaneng.2021.109600.

Shen, Z., D. Wan, and P. M. Carrica (2015), Dynamic overset grids in OpenFOAM with application to KCS self-propulsion and maneuvering, *Ocean Engineering*, *108*, 287 – 306.

Shin, Y. S., V. L. Belenky, W. M. Lin, K. M. Weems, and A. H. Engle (2003), Nonlinear time domain simulation technology for seakeeping and wave-load analysis for modern ship design, *Transactions, Society of Naval Architects and Marine Engineers*, *111*, 557–578.

Silva, K., B. Knight, and K. Maki (2022), Numerical Prediction of Extreme Roll of a Free-Running Ship with Computational Fluid Dynamics and Neural Networks, in *Proceedings of the 34rd Symposium on Naval Hydrodynamics*.

Silva, K. M., and K. J. Maki (2021a), Data-Driven Identification of Critical Wave Groups, in *Proceedings of the 9th Conference on Computational Methods in Marine Engineering (MARINE 2021)*.

Silva, K. M., and K. J. Maki (2021b), Towards a Computational Fluid Dynamics implementation of the critical wave groups method, *Ocean Engineering*, *235*, 109,451, doi:https://doi.org/10.1016/j.oceaneng.2021.109451.

Silva, K. M., and K. J. Maki (2022a), Data-Driven System Identification of 6-DoF Ship Motion in Waves with Neural Networks, *Applied Ocean Research*, *125*, 103,222, doi:https://doi.org/10.1016/j.apor.2022.103222.

Silva, K. M., and K. J. Maki (2022b), Towards a Generalized Neural Network Approach for Identifying Critical Wave Groups, in *Proceedings of the 18th International Ship Stability Workshop*.

Silva, K. M., and K. J. Maki (2023), Implementation of the critical wave groups method with computational fluid dynamics and neural networks, doi:10.48550/ARXIV.2301.09834.

Silva, K. M., W. Xu, and K. J. Maki (2021), Critical Wave Group Implementation with Computational Fluid Dynamics and Neural Networks, in *1st International Conference on the Stability and Safety of Ships and Ocean Vehicles (STAB&S 2021)*.

Themelis, N., and K. J. Spyrou (2007), Probabilistic assessment of ship stability, *SNAME Transactions*, *115*, 181–206.

Weems, K., and D. Wundrow (2013), Hybrid Models for Fast Time-Domain Simulation of Stability Failures in Irregular Waves With Volume-Based Calculations for Froude-Krylov and Hydrostatic Forces, in *Proceedings of the 13th International Ship Stability Workshop*.

Weems, K., V. Belenky, K. Spyrou, S. Aram, and K. Silva (2020), Towards Numerical Estimation of Probability of Capsizing Caused by Broaching-to, in *Proceedings of the 33rd Symposium on Naval Hydrodynamics*.

Whicker, L., and L. Fehlner (1958), Empirical formulas for low-aspect ratio, all-moveable foils, *DTMB Report 933*.

White, P. (2020), A Hybrid Computational Framework for the Simulation of Ships Maneuvering In Waves, Ph.D. thesis, University of Michigan.

Xu, W. (2020), A Machine Learning Framework to Model Extreme Events for Nonlinear Marine Dynamics, Ph.D. thesis, University of Michigan.

Xu, W., G. P. Filip, and K. J. Maki (2020), A Method for the Prediction of Extreme Ship Responses Using Design-Event Theory and Computational Fluid Dynamics, *Journal of Ship Research*, *64*, 48–60.

Xu, W., K. J. Maki, and K. M. Silva (2021), A data-driven model for nonlinear marine dynamics, *Ocean Engineering*, *236*, 109,469, doi:https://doi.org/10.1016/j.oceaneng.2021.109469.